Charged Pion Contribution to the Anomalous Magnetic Moment of the Muon

Thesis by

Kevin Engel

In Partial Fulfillment of the Requirements

for the Degree of

Doctor of Philosophy

California Institute of Technology

Pasadena, California

2013

(Defended May 16, 2013)

Acknowledgements

In my time at Caltech, there have been many people to whom I owe a debt of gratitude. First, I'd like to thank my advisor, Mark Wise, for his support, guidance, and the occasional donut and t-shirt from his quantum mechanics class. His passion for physics is inspiring, and I appreciate both the freedom he gave to pursue the physics I found interesting as well as the helpful suggestions and ideas, including one which led to this thesis. I would also like to thank Michael Ramsey-Musolf who collaborated with me on all of the work presented here. I enjoyed the semester I spent in Wisconsin with his research group. After a meeting with Michael, I always left enthusiastic, confident and ready to tackle the next obstacle.

I am also grateful to my family for their love and support. I would not be who I am without my parents, George and Karen, and they deserve most of the credit for this thesis. As for my sisters, Sarah and Laura, I promise I'll only insist that you call me Dr. Engel once. Finally, I'd like to thank the colleagues and friends who have made these six years of grad school so enjoyable. Long after the details of the magnetic moment calculation presented here fade from my mind, the memories which remain will be the ones we made together.

Abstract

The model dependence inherent in hadronic calculations is one of the dominant sources of uncertainty in the theoretical prediction of the anomalous magnetic moment of the muon. In this thesis, we focus on the charged pion contribution and turn a critical eye on the models employed in the few previous calculations of $a_\mu^{\pi^+\pi^-}$. Chiral perturbation theory (χPT) provides a check on these models at low energies, and we therefore calculate the charged pion contribution to light-by-light (LBL) scattering to $\mathcal{O}(p^6)$. We show that the dominant corrections to the leading order (LO) result come from two low energy constants which show up in the form factors for the $\gamma\pi\pi$ and $\gamma\gamma\pi\pi$ vertices. Comparison with the existing models reveal a potentially significant omission - none include the pion polarizability corrections associated with the $\gamma\gamma\pi\pi$ vertex. We next consider alternative models where the pion polarizability is produced through exchange of the a_1 axial vector meson. These have poor UV behavior, however, making them unsuited for the $a_\mu^{\pi^+\pi^-}$ calculation. We turn to a simpler form factor modeling approach, generating two distinct models which reproduce the pion polarizability corrections at low energies, have the correct QCD scaling at high energies, and generate finite contributions to $a_\mu^{\pi^+\pi^-}$. With these two models, we calculate the charged pion contribution to the anomalous magnetic moment of the muon, finding values larger than those previously reported: $a_\mu^{\mathrm{I}} = -1.779(4) \times 10^{-10}$, $a_\mu^{\mathrm{II}} = -4.892(3) \times 10^{-10}$.

Contents

Chapter 1

Introduction

The anomalous magnetic moment of the muon provides an important test of the Standard Model. As its current measured value approaches an accuracy of one part in 10^8, this precision measurement challenges both experimentalists and theorists. On the theory side, diverse multi-loop contributions from QED, electro-weak, and hadronic physics must all be considered. The current state of the art calculation gives $a_\mu^{\mathrm{SM}} \equiv \frac{g_\mu - 2}{2} = 11659177(5) \times 10^{-10}$[1] (see Ref [2] for a recent review). This theoretical prediction represents a $\sim 4\sigma$ departure from the experimental value $a_\mu^{\mathrm{exp}} = 11659209(6) \times 10^{-10}$[3] obtained by the E821 Collaboration[4, 5, 6]. To some, this discrepancy suggests new beyond the Standard Model (BSM) physics. Ideas such as supersymmetry, extra dimensions, or additional gauge bosons can naturally generate corrections of this size to a_μ^{SM}[7, 8, 9]. To determine whether these corrections are truly necessary, smaller experimental and theoretical errors are required. A next generation experiment has been proposed at Fermilab which will reduce the experimental uncertainty by a factor of four[10]. A similar reduction in the theoretical error would provide a strong probe of BSM physics.

The dominant theoretical uncertainty comes from diagrams with hadronic contributions. These first appear at $\mathcal{O}(\alpha^2)$ as hadronic vacuum polarization (HVP) diagrams which contain hadronic loops modifying a virtual photon propagator. In this case, however, a complete understanding of the hadronic physics is not required, as a dispersion relationship can be used to relate the amplitude to experimental data on $\sigma(e^+ e^- \to \text{hadrons})$. The uncertainty in this contribution can then be related to uncertainties in the $e^+ e^-$ annhilation data and the most recent analysis gives an error $\delta a_\mu^{\mathrm{HVP}} \sim 4 \times 10^{-10}$[1]. Although less straightforward, similar calculations have been done using hadronic τ decays; isospin symmetry relates this process to the $e^+ e^-$ one. Some tension exists between these two methods - τ data currently predicts a larger a_μ^{SM} that is only $\sim 1\sigma$ away from a_μ^{exp}[11]. Others argue that proper inclusion of isospin breaking corrections bring the τ data in line with the $e^+ e^-$ data[12, 13]. These differences will need to be resolved before the HVP error can be reduced.

A more intractable uncertainty occurs at $\mathcal{O}(\alpha^3)$ in light-by-light diagrams. This class of graphs
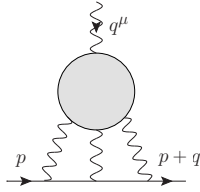
Figure 1.1: LBL contribution to g-2

is shown in Fig 1.1, where the gray blob represents any intermediate states which couple to four photons. In particular, virtual hadrons contribute to these diagrams, and for this process, a theoretical description of these particles is required. Uncertainties in the modeling of the hadrons generate the bulk of the LBL error. Estimates of this error have some range, but generally $\delta a_\mu^{\text{HLBL}} \sim 3 \times 10^{-10}$[14, 15, 16, 17, 18, 19, 20, 21, 22, 23, 24].

The lightest hadronic states are the pions, and therefore one expects these to have the largest impact on a_μ^{HLBL}. An early calculation [25] found the values:

$$a_\mu^{\pi^0} = 6.5 \times 10^{-10}\,, \tag{1.1}$$

$$a_\mu^{\pi^+ \pi^-} = -1.6 \times 10^{-10}\,. \tag{1.2}$$

The π^0 contribution, also known as pseudoscalar exchange, is clearly dominant, and therefore considerable theoretical effort has been focused on reducing the uncertainty from these graphs. As a result, the pseudoscalar exchange error is now comparable with errors from subdominant processes such as charged pion loops which have received much less study from the theoretical community. Any attempts to further reduce the theoretical error must now take these graphs into account.

In this thesis, we re-examine the charged pion loop contribution to a_μ^{HLBL}, focusing, in particular, on the models employed in previous calculations. At low energies, the pions are well described by χPT, an effective field theory of hadronic degrees of freedom relevant to low energy QCD. As such, it is model independent, relying instead on experimentally determined low energy constants, which, in principle, may one day be directly calculated from QCD. In many cases, however, χPT cannot be used to make a direct theoretical prediction. For example, a χPT analysis of the pseudoscalar exchange contribution to a_μ reveals a divergence which must be cancelled by a magnetic moment counterterm, the finite part of which can only be determined by an experimental measurement of a_μ. Consequently, hadronic modeling appears unavoidable in predictions of a_μ^{HLBL}. Nonetheless, χPT can still be used to constrain these models, as they should agree in the low energy regime. We begin with a quick review of this theory.

1.1 Chiral Perturbation Theory

χPT is an effective field theory of the low energy QCD bound states with mass scale $\Lambda_\chi = 4\pi f \sim 1$ GeV. The organizing principle of χPT is chiral symmetry, an approximate global symmetry of QCD which is spontaneously broken from $SU(N_f)_L \times SU(N_f)_R \to SU(N_f)_V$ at low energies. The lightest hadrons are the pions, the pseudo-Nambu-Goldstone bosons of this transition. In 2 flavor χPT, pion interactions are described by the Lagrangian:

$$\mathcal{L}_2 = \frac{f^2}{4}\langle D_\mu U D^\mu U^\dagger \rangle + \frac{f^2}{4}\langle \chi U^\dagger + U\chi^\dagger \rangle. \tag{1.3}$$

We follow the conventions in Ref. [26] where $U(x) = \exp(i\tau^a \pi^a(x)/f)$ is a matrix valued field which transforms as $U(x) \to L(x)U(x)R^\dagger(x)$ under the left and right handed chiral transformations. Ignoring the heavy EW gauge bosons, the covariant derivative is $D_\mu U = \partial_\mu U + ieA_\mu [Q, U]$, where Q = diag(2/3,-1/3). The mass matrix χ is given by $\chi = 2B_0 \text{diag}(m_u, m_d)$. Electroweak and quark mass terms break chiral symmetry in QCD, therefore these terms are needed to enforce the same pattern of symmetry breaking in χPT. Expanded in terms of the three pion fields, this Lagrangian contains standard kinetic terms, mass terms with $m_0^2 = (m_u + m_d)B_0$, and an infinite tower of pion interactions suppressed by powers of f. Note that all interactions in $\mathcal{L}_2$ are proportional to either the pion mass m_0^2 or momentum p^2 (ignoring photons), hence this is known as the $\mathcal{O}(p^2)$ Lagrangian. $\mathcal{L}_2$ consists of all the mass dimension two operators that respect chiral symmetry and parity.

As an effective field theory χPT allows for higher mass dimension operators suppressed by powers of Λ_χ. The $\mathcal{O}(p^4)$ Lagrangian, first written down by Gasser and Leutwyler [27], is parameterized by ten low energy constants (LECs):

$$\begin{aligned}
\mathcal{L}_4 &= \alpha_1 \langle D_\mu U D^\mu U^\dagger \rangle^2 + \alpha_2 \langle D_\mu U D_\nu U^\dagger \rangle \langle D^\mu U D^\nu U^\dagger \rangle + \alpha_3 \langle D_\mu U D^\mu U^\dagger D_\nu U D^\nu U^\dagger \rangle \\
&\quad + \alpha_4 \langle D_\mu U D^\mu U^\dagger \rangle \langle \chi U^\dagger + U\chi^\dagger \rangle + \alpha_5 \langle D_\mu U D^\mu U^\dagger (\chi U^\dagger + U\chi^\dagger) \rangle + \alpha_6 \langle \chi U^\dagger + U\chi^\dagger \rangle^2 \\
&\quad + \alpha_7 \langle \chi^\dagger U - U\chi^\dagger \rangle^2 + \alpha_8 \langle \chi U^\dagger \chi U^\dagger + U\chi^\dagger U\chi^\dagger \rangle + ieF_{\mu\nu}\alpha_9 \langle QD^\mu U D^\nu U^\dagger + QD^\mu U^\dagger D^\nu U \rangle \\
&\quad + e^2 F^{\mu\nu}F_{\mu\nu}\alpha_{10}\langle QUQU^\dagger \rangle. \tag{1.4}
\end{aligned}$$

The LECs are responsible for renormalizing the theory and their finite values must be obtained experimentally. They are typically defined using a modified $\overline{MS}$ scheme:

$$\alpha_i^r = \alpha_i - \frac{\gamma_i}{32\pi^2}\left[\frac{2}{d-4} - \log(4\pi) + \gamma - 1\right]. \tag{1.5}$$

For the LECs which will later be of interest: $\gamma_4 = 1/8$, $\gamma_5 = 1/4$, $\gamma_6 = 3/32$, $\gamma_8 = 0$, $\gamma_9 = 1/6$, $\gamma_{10} = -1/6$.

1.2   Previous $a_\mu^{\pi^+\pi^-}$ calculations

χPT serves as the framework for hadronic light-by-light calculations, the first of which was published in 1985 by Kinoshita et al[25]. They considered only the lightest hadrons, the pions, which affect the muon magnetic moment through pseudoscalar π^0 exchange as well as a $\pi^+\pi^-$ charged pion loop. Unlike the π^0 exchange, the charged pion loop contribution is finite at lowest order in χPT. The $\mathcal{O}(p^2)$ Lagrangian of Eq (1.3) gives rise to the graphs of Fig 4.3, which Kinoshita et al. evaluated numerically to find:

$$a_\mu^{\mathrm{LO}} = -4.8(3) \times 10^{-10} \,. \tag{1.6}$$

This leading order χPT calculation is rather naive in that it treats the pions as structureless and elementary. However, a more complete χPT calculation which includes higher order corrections will no longer be predictive, since, as demonstrated by the divergent π^0 contribution to a_μ, a magnetic moment counterterm first appears in χPT with mass dependence m_μ/f^2. Alternatively, one can introduce models which match onto χPT at low energies, but possess better UV behavior, thereby eliminating the need for counterterms. Kinoshita attempted this by using vector meson dominance (VMD) form factors which modify the couplings of photons to pions. For each photon line in Fig 4.3, Kinoshita et al. inserted the form factor:

$$V(k) = \left(1 - \frac{k^2}{k^2 - M_V^2} \right) \,, \tag{1.7}$$

where k is the photon momenta and $M_V = m_\rho \sim 770$ MeV is the mass of the ρ meson. These result in a supression of the magnetic moment contribution:

$$a_\mu^{\mathrm{VMD}} = -1.6(2) \times 10^{-10} \,. \tag{1.8}$$

From this, the authors concluded that the charged pion contribution was subdominant to the pion exchange contribution, which, having been made finite by the VMD prescription, they had also calculated:

$$a_\mu^{\pi^0} = 6.5(6) \times 10^{-10} \,. \tag{1.9}$$

Consequently, subsequent calculations of a_μ^{HLBL} have mainly focused on the pseudoscalar exchange.

The charged pion contribution appears only in a few papers since that time. In 1996, Kinoshita et al. reexamined their calculation[16], presenting the same results with greater accuracy:

$$a_\mu^{\mathrm{LO}} = -4.46(2) \times 10^{-10} \,, \tag{1.10}$$

$$a_\mu^{\mathrm{VMD}} = -1.67(2) \times 10^{-10} \,. \tag{1.11}$$

They also introduced a refinement of the simple VMD model by using the hidden local symmetry (HLS) Lagrangian [28], which explicitly includes the ρ meson as a dynamical degree of freedom. In this model, ρ exchange gives the same VMD $\gamma\pi\pi$ form factor as in Eq (1.7), but the $\gamma\gamma\pi\pi$ form factor is altered; instead of $(1 - \frac{k_1^2}{k_1^2 - M_V^2})(1 - \frac{k_2^2}{k_2^2 - M_V^2})$, the HLS $\gamma\gamma\pi\pi$ form factor is $(1 - \frac{k_1^2}{k_1^2 - M_V^2} - \frac{k_2^2}{k_2^2 - M_V^2})$. This change led to an even smaller result:

$$a_\mu^{\text{HLS}} = -.44(2) \times 10^{-10} \,. \tag{1.12}$$

Around the same time, a different analysis was published by Bijnens et al. using the extended Nambu-Jona-Lasinio (ENJL) model[15]. Form factors are once again introduced to improve the leading order charged pion loop contribution; these modify the LBL amplitude as follows:

$$\Pi_{\mu\nu\sigma\rho} = V_{\mu\alpha}(k_1)V_{\nu\beta}(k_2)V_{\sigma\gamma}(k_3)V_{\rho\delta}(k_4)\Pi_{\text{LO}}^{\alpha\beta\gamma\delta} \,, \tag{1.13}$$

where

$$V_{\mu\nu}(k) = \frac{g_{\mu\nu}M_V^2(k^2) - k_\mu k_\nu}{M_V^2(k^2) - k^2} \,. \tag{1.14}$$

Due to the gauge invariance of Π_{LO}, the $k_\mu k_\nu$ terms can be dropped from $V_{\mu\nu}(k)$, giving:

$$\Pi_{\mu\nu\sigma\rho} = \frac{M_V(k_1^2)}{M_V^2(k_1^2) - k_1^2} \frac{M_V(k_2^2)}{M_V^2(k_2^2) - k_2^2} \frac{M_V(k_3^2)}{M_V^2(k_3^2) - k_3^2} \frac{M_V(k_4^2)}{M_V^2(k_4^2) - k_4^2} \Pi_{\mu\nu\sigma\rho}^{\text{LO}} \,. \tag{1.15}$$

For fixed M_V which is not a function of momentum, this is equivalent to the full VMD prescription described in Eq (1.7), and Bijnens et al. calculate an a_μ which agrees with Eq (1.11). Incorporating the momentum dependence of M_V, the authors report a slightly different value:

$$a_\mu^{\text{ENJL}} = -1.9(1.3) \times 10^{-10} \,. \tag{1.16}$$

The error quoted here includes an attempt to estimate model uncertainties.

The results discussed above highlight the importance of higher energy corrections in the $a_\mu^{\pi^+\pi^-}$ calculation. For each model, the use of VMD-style form factors strongly supresses the LO result. This is somewhat unexpected, as an evaluation of Eq (1.7) at an energy scale near the muon mass suggests corrections of only a few percent. Given this surprising sensitivity of the $a_\mu^{\pi^+\pi^-}$ calculation to higher energy scales, the reliability of the models which govern the high energy behavior becomes crucial. In this work, we point out the flaws in the current models and seek to improve them; the necessary steps are outlined in the next section.

1.3   Outline

A primary concern in model-based calculations is how well the models capture the relevant physics. We investigate this question in Chapter 2, where we have calculated the charged pion contribution to the LBL scattering amplitude to next-to-leading (NLO) in χPT. Unlike the LBL magnetic moment contribution, this process is finite at this order, and the NLO corrections can be directly compared with model based predictions. The effects of the NLO contributions are easiest to analyze in the ultra-low energy limit $k^2 \ll m_\pi^2$. At this energy scale, we find that the current models reproduce an NLO correction associated with the pion charge radius, but miss a correction of similar magnitude associated with the pion polarizability. Given the large impact of the VMD form factors on a_μ^{LO}, we conclude that proper modeling of the polarizability physics may have a significant impact on $a_\mu^{\pi^+\pi^-}$.

In Chapter 3, we review a resonance model that includes both ρ and a_1 mesons. Exchange of these mesons gives rise to the desired pion charge radius and polarizability corrections at low energies. However, we show that a_1 exchange in this and similar models has poor UV behavior, leading to a divergent $a_\mu^{\pi^+\pi^-}$. Instead, we consider a simpler set of models in which the a_1 has been integrated out, appearing only through form factors. We discuss the modeling constraints and give two distinct realizations. This simple form factor approach satisfies all known constraints from both χPT and QCD and gives a finite contribution to $a_\mu^{\pi^+\pi^-}$.

Armed with our improved models, we proceed to the magnetic moment calculation. The details of this complicated calculation are discussed in Chapters 4 and 5, and our results are given in Chapter 6. We find that for both of our models, the contributions from a_1 exchange tend to cancel the ρ contributions, resulting in a larger (more negative) $a_\mu^{\pi^+\pi^-}$. As before, the calculation is quite sensitive to higher order corrections currently unconstrained by χPT. Different combinations of ρ and a_1 models (which all agree at low energies) lead to estimates of $a_\mu^{\pi^+\pi^-}$ which vary by as much as 5×10^{-10}. This variation is large compared to the currently reported error $\delta a_\mu^{\text{HLBL}}$. This leads to our main conclusion presented in Chapter 7: the charged pion contribution to a_μ may be larger than previously thought, and consequently the uncertainty $\delta a_\mu^{\text{HLBL}}$ should be increased.

Chapter 2

LBL scattering in χPT

At low energy scales, hadronic contributions to LBL scattering can be estimated using χPT. In the usual power counting expansion, the leading order diagrams occur at $\mathcal{O}(p^4)$ and consist of a single loop of charged pions. These graphs are shown in Fig 2.1. In this energy regime, the π^0 pseudoscalar exchange graph of Fig 2.2 is subdominant, appearing at $\mathcal{O}(p^6)$. We ignore the pseudoscalar contribution in what follows, focusing, instead, on the other $\mathcal{O}(p^6)$ contributions which correct the leading order charged pion result. These diagrams are more varied, including both 2-loop graphs and 1-loop graphs with an insertion of an $\mathcal{O}(p^4)$ counterterm. Nonetheless, we have found that these higher order contributions can (mostly) be organized into propagator and vertex corrections, which, when inserted into the original 1-loop graphs, give the NLO contribution to the LBL amplitude. We present our results for the propagator and vertex corrections below, using dimensional regularization for the loop integrals. Because these results are to be placed into 1-loop graphs, we maintain an explicit d throughout.
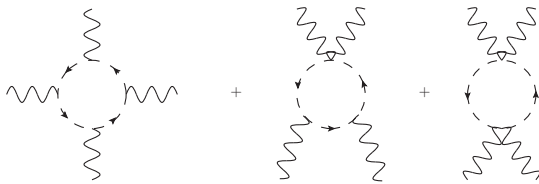

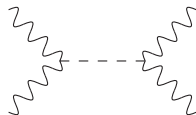Figure 2.1: LO charged pion contribution to LBL.

Figure 2.2: Pseudoscalar exchange contribution to LBL.

2.1 Counterterm and 1-loop corrections

2.1.1 Propagator

The charged pion propagator receives corrections at $\mathcal{O}(p^4)$ from both counterterms and pion loops as shown below.

Figure 2.3: $\mathcal{O}(p^4)$ corrections to the charged pion propagator.

The self energy is found to be:

$$\Pi(k^2) = ik^2 \left[\left(\frac{m_0^2}{f^2} \right) (16\alpha_4 + 8\alpha_5) - \frac{2}{3f^2}\Gamma(1) \left(\frac{1}{m_0^2} \right)^{1-d/2} \right]$$
$$- im_0^2 \left[\left(\frac{m_0^2}{f^2} \right) (32\alpha_6 + 16\alpha_8) - \frac{1}{6f^2}\Gamma(1) \left(\frac{1}{m_0^2} \right)^{1-d/2} \right], \tag{2.1}$$

where we have defined

$$\Gamma(n) \equiv \frac{1}{(4\pi)^{d/2}} \mu^{4-d} \Gamma(n - d/2). \tag{2.2}$$

From this, the physical pion mass can be derived:

$$m_\pi^2 = m_0^2 \left(1 + \left(\frac{m_0^2}{f^2} \right) \left[32\alpha_6^r + 16\alpha_8^r - 16\alpha_4^r - 8\alpha_5^r - \log(\mu^2/m_0^2)/(32\pi^2) \right] \right). \tag{2.3}$$

For the purposes of this calculation, we choose to absorb part of the mass counterterm into m_0, setting the tree level mass equal to the physical pion mass. This way, the LO 1-loop graphs will depend on m_π, not m_0, and therefore do not contribute to NLO. This choice alters the propagator correction, which we write as:

$$\Pi(k^2) = ic_1(k^2 - m_\pi^2) - ic_2 m_\pi^2. \tag{2.4}$$

$$c_1 = \left(\frac{m_\pi^2}{f^2} \right) (16\alpha_4 + 8\alpha_5) - \frac{2}{3f^2}\Gamma(1) \left(\frac{1}{m_\pi^2} \right)^{1-d/2}, \tag{2.5}$$

$$c_2 = \left(\frac{m_\pi^2}{f^2} \right) (32\alpha_6 + 16\alpha_8 - 16\alpha_4 - 8\alpha_5) + \frac{1}{2f^2}\Gamma(1) \left(\frac{1}{m_\pi^2} \right)^{1-d/2}$$
$$- \left(\frac{m_\pi^2}{f^2} \right) \left[32\alpha_6^r + 16\alpha_8^r - 16\alpha_4^r - 8\alpha_5^r - \log(\mu^2/m_\pi^2)/(32\pi^2) \right]. \tag{2.6}$$

The coefficient c_2 is proportional to $d - 4$ and will not appear in the final result.

2.1.2 $\gamma\pi\pi$ vertex

The $\gamma\pi^+\pi^-$ coupling which appears in the $\mathcal{O}(p^2)$ Lagrangian receives corrections from $\mathcal{O}(p^4)$ counterterms as well as pion loops. These graphs are shown in Fig 2.4; we have chosen to represent this result as:

$$= ie(p_1^\nu + p_2^\nu)V_{\mu\nu}(k). \qquad (2.7)$$

In this notation, the full 1PI vertex is given by adding the $\mathcal{O}(p^2)$ vertex, $g^{\mu\nu}$, to $V^{\mu\nu}$. At $\mathcal{O}(p^4)$, $V^{\mu\nu}$ is found to be:

$$V^{\mu\nu}(k) = -\frac{1}{2f^2}J^{\mu\nu}(k) - \frac{2\alpha_9}{f^2}k^\mu k^\nu$$
$$+ g^{\mu\nu}\left[\left(\frac{m_\pi^2}{f^2}\right)(16\alpha_4 + 8\alpha_5) - \frac{5}{3f^2}\Gamma(1)\left(\frac{1}{m_0^2}\right)^{1-d/2} + \frac{2\alpha_9}{f^2}k^2\right], \qquad (2.8)$$

where $J^{\mu\nu}(k)$ is the first of four Feynman integrals needed for this paper. It can be found in the appendix.
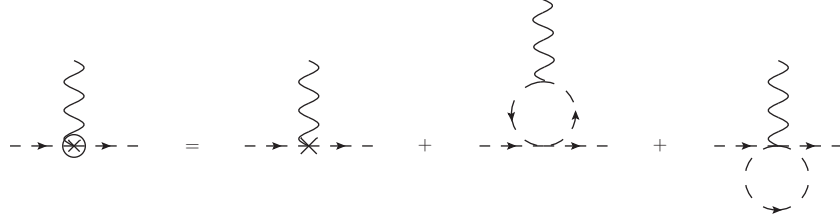
Figure 2.4: $\mathcal{O}(p^4)$ corrections to the $\gamma\pi\pi$ vertex

For on shell pions, the $k^\mu k^\nu$ terms can be ignored. We have checked that the remaining terms reproduce the standard result for the pion form factor[26]:

$$G_\pi(k^2) \equiv 1 + r_\pi^2 k^2/6 + \mathcal{O}(k^4), \qquad (2.9)$$

$$r_\pi^2 = \frac{12\alpha_9^r}{f^2} + \frac{1}{16\pi^2 f^2}\left[\log(\mu^2/m_\pi^2) - 1\right], \qquad (2.10)$$

where r_π is the charge radius of the pion. The α_4 and α_5 dependence of $V^{\mu\nu}$ disappears due to the wavefunction renormalization required for on shell pions. We see that the photon coupling to the charged pion is controlled by α_9. Experimental values of this form factor, measured at different values of k^2, allow for a determination of r_π, and therefore α_9^r. The most recent determination of the charge radius was done by Bijnens et al, who found $\alpha_9^r(m_\rho) = 7.0 \pm .2 \times 10^{-3}$ for two flavor χPT at $\mathcal{O}(p^4)$[29].

2.1.3 $\gamma\gamma\pi\pi$ vertex

This vertex appears at tree level with value $2ie^2 g^{\mu\nu}$, but also receives corrections from the diagrams in Fig 2.5. We have chosen to parameterize the result as:

$$= ie^2 \left[V_1^{\mu\nu}(k_1, k_2) + (p_1^2 + p_2^2 - 2m_\pi^2) V_2^{\mu\nu}(k_1, k_2) \right] \tag{2.11}$$

where

$$
\begin{aligned}
V_1^{\mu\nu}(k_1, k_2) =& \frac{(k_1 + k_2)^2}{f^2} \left(I^{\mu\nu}(k_1, k_2) + g^{\mu\nu} K(k_1, k_2) \right) - \frac{1}{f^2} \left(J^{\mu\nu}(k_1) + J^{\mu\nu}(k_2) \right) \\
& - \frac{16}{3f^2} g^{\mu\nu} \Gamma(1) \left(\frac{1}{m_0^2} \right)^{1-d/2} + 2g^{\mu\nu} \left(\frac{m_\pi^2}{f^2} \right) (16\alpha_4 + 8\alpha_5) \\
& + \frac{8(\alpha_9 + \alpha_{10})}{f^2} (k_1 k_2 g^{\mu\nu} - k_1^\nu k_2^\mu) + \frac{4\alpha_9}{f^2} (g^{\mu\nu}(k_1^2 + k_2^2) - k_1^\mu k_1^\nu - k_2^\mu k_2^\nu),
\end{aligned} \tag{2.12}
$$

$$
V_2^{\mu\nu}(k_1, k_2) = -\frac{1}{3f^2} \left(I^{\mu\nu}(k_1, k_2) + g^{\mu\nu} K(k_1, k_2) \right). \tag{2.13}
$$

Two new Feynman integrals appear in this result - $I^{\mu\nu}$ and K; they can be found in the appendix.
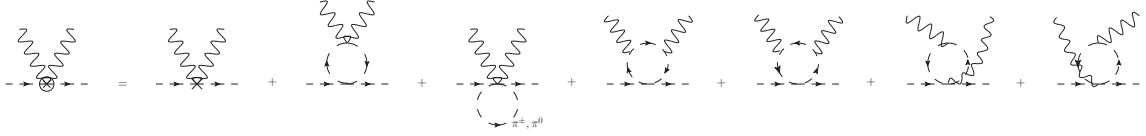
Figure 2.5: $\mathcal{O}(p^4)$ corrections to the $\gamma\gamma\pi\pi$ vertex

Although the fully virtual result is required for our calculation, some insight can be gained by taking the $d \to 4$ limit with on-shell pions and expanding about small photon momenta:

$$
\begin{aligned}
\langle \pi^+(p_2) | A^\mu(k_1) A^\nu(k_2) | \pi^+(p_1) \rangle_{1PI} =& 2ie^2 \Big[g^{\mu\nu} + \frac{r_\pi^2}{6} (g^{\mu\nu}(k_1^2 + k_2^2) - k_1^\mu k_1^\nu - k_2^\mu k_2^\nu) \\
& + \frac{4(\alpha_9^r + \alpha_{10}^r)}{f^2} (k_1 k_2 g^{\mu\nu} - k_1^\nu k_2^\mu) + \mathcal{O}(k^4) \Big].
\end{aligned} \tag{2.14}
$$

We see that the higher momentum corrections are governed by r_π^2 from the one photon vertex, and a new combination of LECs - $\alpha_9^r + \alpha_{10}^r$, associated with the pion polarizability. Pion polarizability measurements are difficult, however, and the best experimental constraint on this quantity comes from radiative pion decay[30]:

$$
\alpha_9^r + \alpha_{10}^r = 1.32 \pm .14 \times 10^{-3}. \tag{2.15}
$$

α_{10}^r can also be determined separately using data from semileptonic τ decays[31]. Converting from three to two flavor χPT, we find $\alpha_{10}^r(m_\rho) = -(5.19 \pm .06 \times 10^{-3})$. When combined with the value for α_9^r suggested by the charge radius, we find reasonable convergence with the result from radiative pion

decay. Some discrepancy still exists when comparing these values to the experimentally measured pion polarizability. The latest results disagree by a factor of 2[32].

2.1.4 Ward identity

We have presented the $\mathcal{O}(p^4)$ corrections to the pion propagator, $\gamma\pi\pi$, and $\gamma\gamma\pi\pi$ vertices. A useful cross-check on this calculation is provided by the full Ward identity, keeping all particles off-shell. Using a path integral technique[33], we derive the usual relationship:

$$\partial_\mu \langle 0|\mathrm{T}j^\mu(x_1)A^\nu(x_2)\pi^-(x_3)\pi^+(x_4)|0\rangle = \tag{2.16}$$
$$e\left[\delta(x_1 - x_4) - \delta(x_1 - x_3)\right]\langle 0|\mathrm{T}A^\nu(x_2)\pi^-(x_3)\pi^+(x_4)|0\rangle .$$

In connected diagrams, an external photon $A^\mu(x_1)$ results in the factor $i\int d^4z\Delta^{\mu\alpha}(x_1 - z)j_\alpha(z)$. By inverting this relationship, Eq (2.16) can be used to relate the $\gamma\gamma\pi\pi$ vertex to the $\gamma\pi\pi$ one. We convert to momentum space (using the labeling of Eq (2.11)), resulting in the Ward identity:

$$k_1^\mu \mathcal{M}_{\mu\nu}(k_1, k_2, p_1, p_2) = e\left[\mathcal{M}_\nu(k_2, p_1 + k_1, p_2) - \mathcal{M}_\nu(k_2, p_1, p_2 - k_1)\right] . \tag{2.17}$$

Note that the amplitudes here are the full ones, not just the 1PI part. External photon legs are amputated in the conversion between j^μ and A^μ, but pion ones are not. These amplitudes are given in the appendix, written in terms of the functions discussed in this section. We have verified, after a lengthy calculation, that Eq (2.17) is indeed satisfied.

2.2 LBL amplitude

At leading order, we need only consider the three diagrams in Fig 2.1. The full LBL amplitude is given by permuting the photon momenta and indices, taking into consideration the symmetries of each graph:

$$\Pi_{\mathrm{LO}}^{\mu\nu\sigma\rho}(k_1, k_2, k_3, k_4) = ie^4\left[\tfrac{1}{4}H^{\mu\nu\sigma\rho}(k_1, k_2, k_3, k_4) + g^{\mu\nu}I^{\sigma\rho}(k_3, k_4) + \tfrac{1}{2}g^{\mu\nu}g^{\sigma\rho}K(k_3, k_4)\right] + \mathrm{perms} .$$
$$\tag{2.18}$$

In the $d \to 4$ limit, $H^{\mu\nu\sigma\rho}$, $I^{\sigma\rho}$, and K are all divergent, but when the 24 permuations are taken into account, the divergences cancel, leaving $\Pi_{\mathrm{LO}}^{\mu\nu\sigma\rho}$ finite. A 4-photon counterterm does not appear in χPT until $\mathcal{O}(p^8)$, therefore, both LO and NLO results must be finite.

The NLO diagrams are shown in Fig 2.6, utilizing the vertex and propagator corrections discussed in Section 2.1. As mentioned earlier, this method of organizing the various corrections is not quite perfect, and some overcounting takes place when the full permutations are considered. The three

2-loop graphs i-k of Fig 2.6 are double counted in graphs g-h and their value must be subtracted to arrive at the final answer.

(a)   (b)   (c)   (d)

(e)   (f)   (g)   (h)

(i)   (j)   (k)
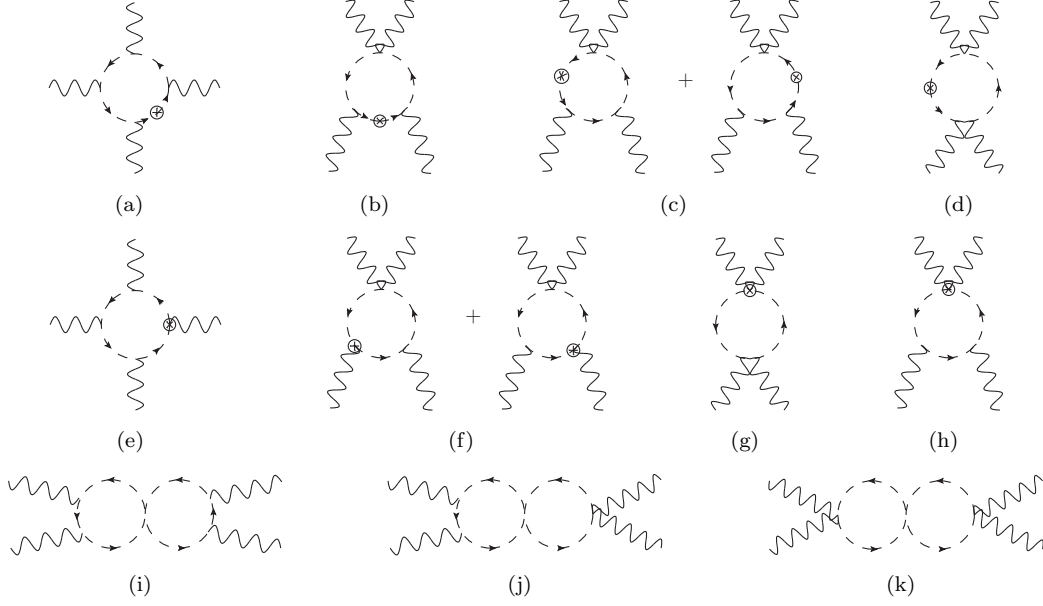
Figure 2.6: NLO charged pion contribution to LBL. Use of the form factors leads to a double counting of the 2-loop graphs i-k. These graphs must be subtracted from graphs a-h to find the NLO LBL amplitude.

The amplitude for the first eight diagrams is given below:

$$a) - ie^4 c_1 H^{\mu\nu\sigma\rho}(k_1, k_2, k_3, k_4)\,,$$

$$b) - ie^4 c_1 g^{\mu\nu} I^{\sigma\rho}(k_3, k_4)\,,$$

$$c) - 2ie^4 c_1 g^{\mu\nu} I^{\sigma\rho}(k_3, k_4)\,,$$

$$d) - ie^4 c_1 g^{\mu\nu} g^{\sigma\rho} K(k_3, k_4)\,,$$

$$e) \, ie^4 V^{\sigma\alpha}(k_3) H^{\mu\nu}{}_\alpha{}^\rho(k_1, k_2, k_3, k_4)\,,$$

$$f) \, 2ie^4 g^{\mu\nu} V^{\sigma\alpha}(k_3) I_\alpha{}^\rho(k_3, k_4)\,,$$

$$g) \tfrac{1}{2} ie^4 g^{\sigma\rho} \left[V_1^{\mu\nu}(k_1, k_2) K(k_3, k_4) - 2V_2^{\mu\nu}(k_1, k_2) \Gamma(1) \left(\tfrac{1}{m_\pi^2} \right)^{1-d/2} \right]\,,$$

$$h) \tfrac{1}{2} ie^4 \left[V_1^{\mu\nu}(k_1, k_2) I^{\sigma\rho}(k_3, k_4) - V_2^{\mu\nu}(k_1, k_2) \left(J^{\sigma\rho}(k_3) + J^{\sigma\rho}(k_4) \right) \right]\,.$$

We have neglected contributions to graphs a-d proportional to c_2 which go to zero in the limit $d \to 4$. Some simplification can be achieved by absorbing a factor of $c_1 g^{\mu\nu}$ into the vertex form factors:

$$\tilde{V}^{\mu\nu}(k) = V^{\mu\nu} - c_1 g^{\mu\nu}\,, \tag{2.19}$$

$$\tilde{V_1}^{\mu\nu}(k_1, k_2) = V_1^{\mu\nu}(k_1, k_2) - 2c_1 g^{\mu\nu}\,. \tag{2.20}$$

By using these modified form factors in graphs e-h, we also reproduce graphs a-d. Note that the modified form factors no longer depend on α_4 and α_5. They are the form factors appropriate for renormalized pions.

Amplitudes for graphs i-k are given below. Graphs i and j contain structures which disappear under permutation; we present the simplified expressions that result from a judicious combination of photon permutations:

$$i)\ \frac{ie^4}{12f^2}[3(k_1+k_2)^2 I^{\mu\nu}(k_1,k_2)I^{\sigma\rho}(k_3,k_4) + I^{\mu\nu}(k_1,k_2)\left(J^{\sigma\rho}(k_3)+J^{\sigma\rho}(k_4)\right)$$
$$+\left(J^{\mu\nu}(k_1)+J^{\mu\nu}(k_2)\right)I^{\sigma\rho}(k_3,k_4)],$$

$$j)\ \frac{ie^4}{6f^2}\left[3(k_1+k_2)^2 K(k_1,k_2)I^{\sigma\rho}(k_3,k_4) + K(k_1,k_2)\left(J^{\sigma\rho}(k_3)+J^{\sigma\rho}(k_4)\right) + 2I^{\sigma\rho}(k_3,k_4)\Gamma(1)\left(\frac{1}{m_\pi^2}\right)^{1-d/2}\right],$$

$$k)\ \frac{ie^4}{6f^2}g^{\mu\nu}g^{\sigma\rho}\left[2(k_1+k_2)^2 K(k_1,k_2)K(k_3,k_4) + (K(k_1,k_2)+K(k_3,k_4))\Gamma(1)\left(\frac{1}{m_\pi^2}\right)^{1-d/2}\right].$$

Putting all these contributions together, the NLO LBL amplitude is:

$$\Pi^{\mu\nu\sigma\rho}_{\text{NLO}}(k_1,k_2,k_3,k_4) = ie^4\Big\{\tilde{V}^{\sigma\alpha}(k_3)\left[H^{\mu\nu}{}_\alpha{}^\rho(k_1,k_2,k_3,k_4) + 2g^{\mu\nu}I_\alpha{}^\rho(k_3,k_4)\right]$$
$$+\left[\frac{1}{2}\tilde{V}_1{}^{\mu\nu}(k_1,k_2) - \frac{(k_1+k_2)^2}{4f^2}\left(I^{\mu\nu}(k_1,k_2)+g^{\mu\nu}K(k_1,k_2)\right)\right]\left[I^{\sigma\rho}(k_3,k_4)+g^{\sigma\rho}K(k_3,k_4)\right]\Big\}$$
$$+\text{ perms}. \tag{2.21}$$

2.3 LBL effective Lagrangian

For low energy processes with $k^2 \ll m_\pi^2$, the LBL result in the previous section can be expanded as a power series in the photon momenta. The integrals become simple polynomials in the Feynman parameters and are easily evaluated. We match the result onto an effective Lagrangian as coefficients of 4-photon operators. Note that the momentum expansion here is not the same as the χPT one where $k^2 \sim m_\pi^2 \ll (4\pi f)^2$. At lowest order in the momentum expansion, there are only two mass dimension eight operators:

$$32\mathcal{O}_1^{(8)} = (F^{\mu\nu}F_{\mu\nu})^2,$$
$$8\mathcal{O}_2^{(8)} = F_{\alpha\beta}F^{\beta\gamma}F_{\gamma\delta}F^{\delta\alpha}.$$

The LO and NLO contributions to the coefficients of these two operators appear in Table 2.1, with the common factor $e^4/(4\pi)^2 m_\pi^4$ removed. Only one NLO correction appears at this order, as these are usually associated with additional powers of momenta. The full impact of the NLO corrections can be seen by going to the next order in the momentum expansion. As we show in the appendix, there are naively 24 distinct operators which can be formed by combining two derivatives and four

field strengths. However, 7 of these can be eliminated through integration by parts, and another 10 are related by exchanging external derivatives with field strength derivatives. This leaves a non-unique but complete basis of seven $d = 10$ operators which we have chosen as:

$$16\,\mathcal{O}_1^{(10)} = \partial_\rho F_{\mu\nu}\partial^\rho F^{\mu\nu}F_{\alpha\beta}F^{\alpha\beta}\,,$$

$$8\,\mathcal{O}_2^{(10)} = \partial_\rho F_{\mu\nu}F^{\mu\nu}\partial^\rho F_{\alpha\beta}F^{\alpha\beta}\,,$$

$$2\,\mathcal{O}_3^{(10)} = \partial_\rho F_{\alpha\beta}\partial^\rho F^{\beta\gamma}F_{\gamma\delta}F^{\delta\alpha}\,,$$

$$4\,\mathcal{O}_4^{(10)} = \partial_\rho F_{\alpha\beta}F^{\beta\gamma}\partial^\rho F_{\gamma\delta}F^{\delta\alpha}\,,$$

$$4\,\mathcal{O}_5^{(10)} = \partial^\mu F_{\mu\nu}F^{\alpha\nu}\partial_\alpha F_{\beta\gamma}F^{\beta\gamma}\,,$$

$$4\,\mathcal{O}_6^{(10)} = F_{\mu\nu}F^{\alpha\nu}\partial^\mu F_{\beta\gamma}\partial_\alpha F^{\beta\gamma}\,,$$

$$2\,\mathcal{O}_7^{(10)} = F_{\mu\nu}\partial^\mu F_{\alpha\beta}\partial^\nu F^{\beta\gamma}F_{\gamma\alpha}\,.$$

The coefficients of these operators are given in Table 2.2.

Table 2.1: Coefficients of lowest dimension ($d = 8$) operators contributing to the LBL amplitude, scaled by $(4\pi)^2 m_\pi^4/e^4$. Second and third columns give LO and NLO contributions in χPT, while the final column indicates the LO corrections from current VMD-style models.

Operator	LO	NLO	VMD
$\mathcal{O}_1^{(8)}$	1/9	$\frac{m_\pi^2}{f^2}\frac{16}{3}(\alpha_9^r + \alpha_{10}^r)$	0
$\mathcal{O}_2^{(8)}$	1/45	0	0

Table 2.2: Coefficients of $d = 10$ operators $\mathcal{O}_n^{(10)}$ contributing to the LBL amplitude, scaled by $(4\pi)^2 m_\pi^6/e^4$. First column denotes operator index n. Second and third columns give LO and NLO contributions in χPT, while final column indicates the LO corrections from current VMD-style models . Identifying $r_\pi^2 = 6/M_V^2$ (see text) implies agreement between the two-loop χPT and VMD predictions for the charge radius contribution.

n	LO	NLO	VMD
1	$\frac{1}{45}$	$\frac{1}{3}\left\{\frac{1}{9}(m_\pi r_\pi)^2 + \frac{4}{5}(\frac{m_\pi}{f})^2(\alpha_9^r + \alpha_{10}^r)\right\}$	$\frac{2}{9}\frac{m_\pi^2}{M_V^2}$
2	$\frac{2}{45}$	$\frac{1}{9}\left\{\frac{1}{3}(m_\pi r_\pi)^2 + \frac{1}{2}\frac{m_\pi^2}{\Lambda_\chi^2} + \frac{44}{5}(\frac{m_\pi}{f})^2(\alpha_9^r + \alpha_{10}^r)\right\}$	$\frac{2}{9}\frac{m_\pi^2}{M_V^2}$
3	$\frac{2}{315}$	$\frac{1}{135}(m_\pi r_\pi)^2$	$\frac{2}{45}\frac{m_\pi^2}{M_V^2}$
4	$\frac{1}{189}$	$\frac{1}{135}(m_\pi r_\pi)^2$	$\frac{2}{45}\frac{m_\pi^2}{M_V^2}$
5	$\frac{1}{135}$	$\frac{4}{45}(\frac{m_\pi}{f})^2(\alpha_9^r + \alpha_{10}^r)$	0
6	$\frac{1}{315}$	0	0
7	$\frac{1}{945}$	0	0

Our low energy expansion yields several interesting results. First, we find that the bulk of the LBL corrections can be organized into either pion charge radius corrections $\sim r_\pi^2$ or pion polarizability corrections $\sim \alpha_9^r + \alpha_{10}^r$. These are associated with corrections to the $\gamma\pi\pi$ and $\gamma\gamma\pi\pi$ vertices respectively. To this order, at least, it seems that correct modeling of the photon-pion interactions gives the dominant higher order corrections to the LBL amplitude. Second, we find that the LO LBL amplitude is numerically supressed, making the NLO corrections more significant. Because the 4-photon operators have been defined with appropriate symmetry factors, one naively expects $\mathcal{O}(1)$ coefficients from LO and $m_\pi^2/\Lambda_\chi^2 \cdot \mathcal{O}(1)$ coefficients from the chirally supressed NLO. Taking $\mathcal{O}_1^{(8)}$ as an example, we find an NLO contribution, which, upon plugging in the experimental value for $\alpha_9^r + \alpha_{10}^r$, evaluates to $1.1 \times m_\pi^2/\Lambda_\chi^2$, in agreement with our expectation. The LO contribution, on the other hand, is numerically supressed by a factor of $1/9$. Rather than the $\sim \frac{m_\pi^2}{\Lambda_\chi^2} \sim 1\%$ corrections suggested by χPT power counting, for $\mathcal{O}_1^{(8)}$, the NLO results modify the LO by 15%. The remaining coefficients tell a similar story, with NLO corrections due to the pion charge radius and/or pion polarizability resulting in $\mathcal{O}(10-20\%)$ modifications of the LO coefficients. The two types of corrections occur in Tables 2.1 and 2.2 in roughly comparable size; the charge radius correction is largest for $\mathcal{O}_1^{(10)}(\sim 30\%)$, while the strongest effects of the polarizability appear in $\mathcal{O}_1^{(8)}(\sim 15\%)$. Our low energy results suggest that NLO corrections to LBL can be significant and arise mainly from corrections to the $\gamma\pi\pi$ and $\gamma\gamma\pi\pi$ vertices.

2.4   LBL and $g - 2$

The NLO results in the previous section allow for a low energy comparison between χPT and the models which have been used to calculate $a_\mu^{\pi^+\pi^-}$. In the low energy regime, the ENJL, full VMD, and HLS models all produce $\gamma\pi\pi$ and $\gamma\gamma\pi\pi$ form factors which are identical to $\mathcal{O}(k^2)$. Applying these to the LO LBL graphs give corrections which are shown in the last column of Tables 2.1 and 2.2 and should be compared with the NLO χPT predictions. Identifying M_V^2 with $6/r_\pi^2$, we see that these VMD-style models fail to capture all of the relevant physics, reproducing LBL corrections due to the charge radius, but not the pion polarizability. Given the comparable magnitudes of these two corrections in the previous section, one suspects that a model which includes polarizability corrections may deviate substantially from the VMD predictions. Of course, these low energy results $(k^2 \ll m_\pi^2)$ cover only a small portion of the enrgy range important to the magnetic moment calculation and therefore may not be indicative of their impact on $a_\mu^{\pi^+\pi^-}$. Indeed, the three VMD-style models agree at these low energies, but, as discussed in Section 1.2, give rather different values for $a_\mu^{\pi^+\pi^-}$. While it is unclear what effect the inclusion of polarizability will have on $a_\mu^{\pi^+\pi^-}$, the VMD results certainly demonstrate that NLO contributions to the magnetic moment are far from negligible. A proper estimation of $a_\mu^{\pi^+\pi^-}$ should model all NLO effects, including the pion

polarizability.

Previous $a_\mu^{\pi^+\pi^-}$ calculations have all used VMD-style models where the $\gamma\pi\pi$ and $\gamma\gamma\pi\pi$ form factors are the result of vector meson exchange. These models fit within the more general framework of resonance saturation, where the finite parts of the χPT counterterms are saturated by the exchange of low-lying resonances[34]. In this framework, the charge pion radius is associated with exchange of the ρ vector meson. Existing models include this using a $\gamma\pi\pi$ form factor such as $(1 - \frac{k^2}{k^2 - M_V^2})$. At low energies, this must match the form factor calculated using χPT, giving the relationship $M_V^2 = 6/r_\pi^2$. Measurements of the pion charge radius are in good agreement with the identification of M_V as the ρ mass. Pion polarizability corrections, on the other hand, are induced by exchanges of the a_1 axial-vector meson. In this case, low energy matching gives $M_A^2 = \frac{f^2}{4(\alpha_9 + \alpha_{10})}$. Despite being the same order in chiral power counting, no $a_\mu^{\pi^+\pi^-}$ calculation has included these effects. Although the a_1 is more massive than the ρ, the large $a_\mu^{\pi^+\pi^-}$ corrections induced by including the ρ exchanges lead us to suspect that the a_1 contributions will be non-negligible. A more complete estimation of $a_\mu^{\pi^+\pi^-}$ should incorporate both ρ and a_1 exchanges. The remainder of this thesis is devoted to that task. In the next chapter, we survey existing a_1 models. Finding them inadequate for the magnetic moment calculation, we then create two simple models of a_1 exchange which result in finite contributions to $a_\mu^{\pi^+\pi^-}$.

Chapter 3

a_1 modeling

3.1 AT model

In hadronic physics, the idea of form factors dominated by exchange of resonances is an old one. After the advent of χPT in 1984 by Gasser and Leutwyler[27] it was quickly realized that a limited number of low-lying resonances could explain the $\mathcal{O}(p^4)$ LECs [34]. In particular the LECs α_9 and α_{10} can be associated with the ρ vector meson and the a_1 axial vector meson. These resonances can be incorporated into χPT in a number of ways; two of the most popular models are the generalized hidden local symmetry (GHLS) model [35] and the antisymmetric tensor (AT) model [34]. Despite the very different realizations of the resonances, Ecker et al. showed that their effects on the pion couplings were identical[36]. We focus here on the simpler AT model which, unlike GHLS, requires no χPT counterterms.

3.1.1 Formulation

In this model, the vector resonances are described by antisymmetric tensors which transform non-linearly under the chiral symmetry:

$$R_{\mu\nu} \to h R_{\mu\nu} h^\dagger \,. \tag{3.1}$$

Here h is defined by the transformation of the goldstone fields:

$$u(\pi) \to g_L u(\pi) h^\dagger \equiv h u(\pi) g_R^\dagger \,, \tag{3.2}$$

where $u(\pi)^2 = U(\pi) = \exp(i\pi^i \tau^i / f)$. A covariant derivative can be defined for fields which transform as in Eq (3.1):

$$\nabla_\mu R = \partial_\mu R + [\Gamma_\mu, R] \,, \tag{3.3}$$

with connection Γ_μ defined in terms of $u(\pi)$ and the external gauge fields associated with the chiral symmetries:

$$\Gamma_\mu = \tfrac{1}{2}\left[u^\dagger(\partial_\mu + il_\mu)u + u(\partial_\mu + ir_\mu)u^\dagger\right].\tag{3.4}$$

To describe massive vector particles, the kinetic term must include only three degrees of freedom. For antisymmetric tensors, this gives rise to two possible Lagrangians - the AT model employs the one where the R_{0i} are the propagating degrees of freedom:

$$\mathcal{L}_{\mathrm{kin}}(R_{\mu\nu}) = -\tfrac{1}{2}\langle\nabla^\mu R_{\mu\alpha}\nabla_\nu R^{\nu\alpha}\rangle + \tfrac{1}{4}M_R^2\langle R_{\mu\nu}R^{\mu\nu}\rangle.\tag{3.5}$$

With this choice of kinetic terms, the most general Lagrangian to $\mathcal{O}(p^2)$ in chiral power counting and linear in the vector resonance $V_{\mu\nu}$ and axial vector resonance $A_{\mu\nu}$ is given by:

$$\mathcal{L}_{\mathrm{AT}} = \mathcal{L}_{\mathrm{kin}}(V_{\mu\nu}) + \mathcal{L}_{\mathrm{kin}}(A_{\mu\nu}) + \tfrac{F_V}{2\sqrt{2}}\langle V_{\mu\nu}f_+^{\mu\nu}\rangle - i\tfrac{G_V}{2\sqrt{2}}\langle V_{\mu\nu}[u^\mu,u^\nu]\rangle - \tfrac{F_A}{2\sqrt{2}}\langle A_{\mu\nu}f_-^{\mu\nu}\rangle,\tag{3.6}$$

where:

$$f_\pm^{\mu\nu} = u^\dagger F_L^{\mu\nu}u \pm uF_R^{\mu\nu}u^\dagger,\tag{3.7}$$

$$u_\mu = iu^\dagger D_\mu U u = iu^\dagger(\partial_\mu U + il_\mu U - iU r_\mu)u.\tag{3.8}$$

For the $g-2$ calculation, our interest is in the resonance interactions with pions and photons. For the two flavor case, with:

$$V_{\mu\nu} = \begin{pmatrix} \tfrac{1}{\sqrt{2}}\rho_{\mu\nu}^0 & \rho_{\mu\nu}^+ \\ \rho_{\mu\nu}^- & \tfrac{1}{\sqrt{2}}\rho_{\mu\nu}^0 \end{pmatrix} \quad,\quad A_{\mu\nu} = \begin{pmatrix} \tfrac{1}{\sqrt{2}}a_{\mu\nu}^0 & a_{\mu\nu}^+ \\ a_{\mu\nu}^- & \tfrac{1}{\sqrt{2}}a_{\mu\nu}^0 \end{pmatrix},\tag{3.9}$$

the relevant interactions can be extracted from Eq (3.6):

$$\mathcal{L} = -\tfrac{1}{2}\partial^\mu\rho_{\mu\alpha}^0\partial_\nu\rho^{0\nu\alpha} + \tfrac{1}{4}M_V^2\rho_{\mu\nu}^0\rho^{0\mu\nu} - D^\mu a_{\mu\alpha}^+ D_\nu a^{-\nu\alpha} + \tfrac{1}{2}M_A^2 a_{\mu\nu}^+ a^{-\mu\nu} +$$
$$\tfrac{F_V e}{2}F^{\mu\nu}\rho_{\mu\nu}^0\left(1 - \tfrac{\pi^+\pi^-}{f^2}\right) - \tfrac{iG_V}{f^2}\rho^{0\mu\nu}\left(D_\mu\pi^+ D_\nu\pi^- - D_\nu\pi^+ D_\mu\pi^-\right) - \tfrac{iF_A e}{2f}F^{\mu\nu}\left(a_{\mu\nu}^-\pi^+ - a_{\mu\nu}^+\pi^-\right).$$
$$\tag{3.10}$$

The various parameters in this model are constrained experimentally and theoretically; some of these restrictions are discussed in more detail in Sec 3.2.1. For now, we follow Ref [36] and set $F_V = \sqrt{2}f$, $G_V = f/\sqrt{2}$, $F_A = f$, $M_A = \sqrt{2}M_V$.

3.1.2 AT form factors and $g - 2$

The Lagrangian above contains ρ^0 and $a_1^\pm$ mesons which couple both to the photon and the charged pions. These interactions modify the elementary photon-pion couplings found in the $\mathcal{O}(p^2)$ χPT Lagrangian. The $\gamma\pi\pi$ vertex, given at LO in χPT as $V^\mu = ie(p_1^\mu + p_2^\mu)$ becomes:

$$V_{AT}^\mu = ie(p_{1\nu} + p_{2\nu}) \left[g^{\mu\nu} - \frac{g^{\mu\nu}k^2 - k^\mu k^\nu}{k^2 - M_V^2} \right] . \tag{3.11}$$

The $\gamma\gamma\pi\pi$ vertex, with LO amplitude $V^{\mu\nu} = 2ie^2 g^{\mu\nu}$, receives corrections from both ρ and a_1 exchanges:

$$
\begin{aligned}
V_{AT}^{\mu\nu} = 2ie^2 \Bigg[& g^{\mu\nu} - \left(\frac{g^{\mu\nu}k_1^2 - k_1^\mu k_1^\nu}{k_1^2 - M_V^2} + \frac{g^{\mu\nu}k_2^2 - k_2^\mu k_2^\nu}{k_2^2 - M_V^2} \right) + \\
& \frac{1}{M_A^2}(k_1 k_2 g^{\mu\nu} - k_2^\mu k_1^\nu) - \\
& \frac{1}{2M_A^2(P_1^2 - M_A^2)}(k_1 k_2 P_1^\mu P_1^\nu - P_1 k_2 P_1^\mu k_1^\nu - P_1 k_1 k_2^\mu P_1^\nu + g^{\mu\nu} P_1 k_1 P_1 k_2) - \\
& \frac{1}{2M_A^2(P_2^2 - M_A^2)}(k_1 k_2 P_2^\mu P_2^\nu - P_2 k_2 P_2^\mu k_1^\nu - P_2 k_1 k_2^\mu P_2^\nu + g^{\mu\nu} P_2 k_1 P_2 k_2) \Bigg] ,
\end{aligned}
\tag{3.12}
$$

where $P_1 = p_1 + k_1$ and $P_2 = p_1 + k_2$.

In the AT model, ρ exchanges affect the LO $g - 2$ calculation only through the form factors given above. From an effective field theory viewpoint, these two form factors can be viewed as higher momentum modifications of the $\gamma\pi\pi$ and $\gamma\gamma\pi\pi$ vertices; gauge invariance then allows for a simplified structure. Terms proportional to k^μ arise from $\partial_\mu A^\mu$ terms in the Lagrangian. In the Lorenz gauge, these structures vanish and can safely be ignored. For a more general gauge, as we show in the appendix, proper choice of gauge fixing term can eliminate these structures at the cost of adding additional interactions higher order in α. Therefore, to lowest order in α, independent of the choice of gauge, the k^μ terms in the form factors can be ignored. For the ρ exchanges, this results in simple, multiplicative form factors that modify the LO vertices:

$$V_{AT,\rho}^\mu \rightarrow ie(p_1^\mu + p_2^\mu)\left(1 - \frac{k^2}{k^2 - M_V^2}\right), \tag{3.13}$$

$$V_{AT,\rho}^{\mu\nu} \rightarrow 2ie^2 g^{\mu\nu}\left(1 - \frac{k_1^2}{k_1^2 - M_V^2} - \frac{k_2^2}{k_2^2 - M_V^2}\right). \tag{3.14}$$

These are identical to the form factors used by Kinoshita et al. in their calcuation of a_μ^{HLS}.

The a_1 contributions to the magnetic moment, on the other hand, have not been previously calculated. These are more complicated, for, in addition to the effect on the $\gamma\gamma\pi\pi$ form factor, gauge invariance requires that we also include diagrams like the ones in Fig 3.1(b). Furthermore, from Eq (3.12), we see that a_1 exchange in the AT model has poor UV behavior as compared to ρ

(a) a_1 exchange contribution to the $\gamma\gamma\pi\pi$ form factor and $g-2$.

(b) Non form factor a_1 exchange graphs which must accompany diagrams like (a) in order to preserve gauge invariance.
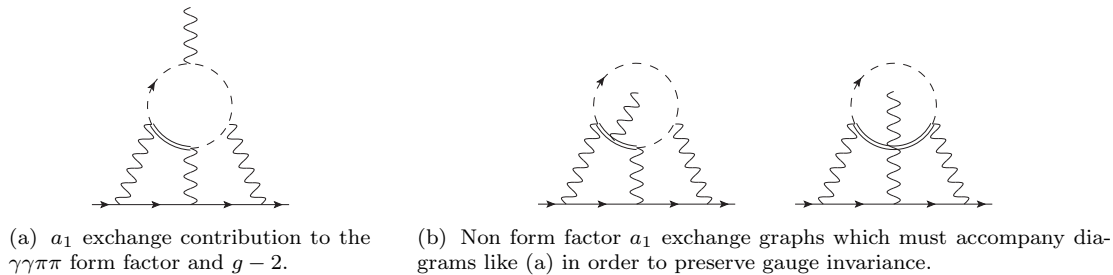
Figure 3.1: Some a_1 (doubled line) contributions to the magnetic moment in the AT theory.

exchange. This is due to the bad UV behavior of the massive meson propagator. The specific form of the $\gamma\rho$ vertex leads to convergent ρ exchanges, but no such cancellations occur for the a_1. In the $g-2$ calculation this invariably leads to divergent contributions from various subgraphs. We see no reason for the divergences to cancel in the sum, and expect a counterterm will be required for a finite a_μ^{AT}. This position is supported by Ref [37] wherein the pion mass splitting was calculated using the AT model. In order to achieve a finite result, the authors were forced to include additional form factors which suppressed the a_1 contribution at high energies.

In other resonance models, such as GHLS, where the mesons are included as the usual 4-vectors, Lorentz invariance limits the form of the a_1 exchange interaction, and the finite parts of the α_9 and α_{10} χPT counterterms must be explicitly added to the theory [36]. These counterterms contribute to the two photon form factor:

$$V_{\text{CT}}^{\mu\nu} = \tfrac{2ie^2}{M_A^2}(g^{\mu\nu}k_1k_2 - k_2^\mu k_1^\nu)\,, \tag{3.15}$$

and, unless a_1 exchange exactly cancels these terms for large k_1,k_2, the resulting a_μ calculation will diverge. Existing models can likely be altered with higher momentum terms to ensure this cancellation; however, we found it simpler to create our own models. In the next few sections we discuss modeling constraints and present two minimal models of a_1 exchange with improved UV behavior. When combined with the appropriate ρ exchanges these models satisfy all known constraints from χPT and QCD.

3.2 a_1 form factors

The resonance models discussed in the previous section include the ρ and a_1 mesons as full propagating degrees of freedom. For the $g-2$ calculation, however, this level of complexity is unnecessary as these particles appear mainly as modifications to the $\gamma\pi\pi$ and $\gamma\gamma\pi\pi$ vertices. In this work, we adopt an effective field theory viewpoint in which the resonances have been integrated out, leaving behind form factors which modify the photon-pion interactions. Despite the considerable modeling

freedom inherent in this approach, our form factors are constrained at both low and high energies; for the two models discussed below, these restrictions give rise to a relatively model independent result.

3.2.1 Constraints

At low energies, the form factors are constrained by the experimentally measured $\mathcal{O}(p^4)$ χPT counterterms. For the $\gamma\pi\pi$ vertex, a 1-loop calculation, in the simplifying limit of photon momenta $k^2 \ll m_\pi^2$, gives:

$$V_{\chi\mathrm{PT}}^\mu \sim ie(p_{1\nu} + p_{2\nu})\left[g^{\mu\nu} + \tfrac{r_\pi^2}{6}(g^{\mu\nu}k^2 - k^\mu k^\nu)\right]. \tag{3.16}$$

Similarly, for the $\gamma\gamma\pi\pi$ vertex with incoming photon momenta k_1^μ and k_2^ν, one finds:

$$V_{\chi\mathrm{PT}}^{\mu\nu} \sim 2ie^2\Big[g^{\mu\nu} + \tfrac{r_\pi^2}{6}(g^{\mu\nu}k_1^2 - k_1^\mu k_1^\nu + g^{\mu\nu}k_2^2 - k_2^\mu k_2^\nu)+$$
$$\tfrac{4(\alpha_9^r+\alpha_{10}^r)}{f^2}(k_1 k_2 g^{\mu\nu} - k_2^\mu k_1^\nu)\Big]. \tag{3.17}$$

In the framework of resonance saturation, the pion charge radius can be written in terms of the ρ mass: $r_\pi^2 = 6/M_V^2$, and the pion polarizability can be written in terms of the a_1 mass: $4(\alpha_9^r + \alpha_{10}^r) = f^2/M_A^2$. With this choice of parameterization, the Weinberg sum rules[38] imply that $M_A = \sqrt{2}M_V$, in reasonable agreement with the experimentally measured values.

At high energies, the amplitudes are constrained by QCD [39, 40]. For large photon momenta $k = k_1 = -k_2 = q \to \infty$, a parton-level analysis suggests that both form factors should fall off as $1/q^2$. As pointed out in Ref [40], the $\gamma\gamma\pi\pi$ vertex in the HLS model does not satisfy this constraint, as it fails to vanish at large q^2. However, the full VMD prescription used in the ENJL model is no better, falling off too quickly as $1/q^4$. In addition to correcting the low energy behavior of these models, adding an a_1 contribution can also fix the asymptotic behavior at high energies.

One other possible check on the form factors is given by the electromagnetic pion mass shift. Because they couple to photons, the self energy of the charged pions differs from that of the π^0, and this difference is clearly affected by any additional physics which modify the photon-pion couplings. Using the AT model along with some additional form factors, the authors of Ref [37] found reasonable agreement with the experimentally measured value. The two form factors play a large role in this calculation, and therefore the mass shift provides a useful independent cross-check of any models used in the $g - 2$ calculation.

Finally, though not strictly necessary, a predictive $g - 2$ calculation requires an a_1 contribution that is well behaved at high energies. Although the AT model satisfies both the χPT and QCD constraints, it fails this one. This is most readily apparent in the LBL diagram shown in Fig 3.2. Two a_1 exchanges lead to a non-convergent loop integral, and, as these are formally distinct from
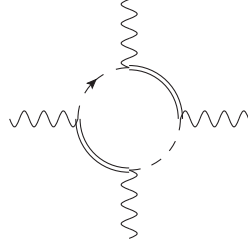
Figure 3.2: Divergent LBL diagram in the AT theory for two a_1 exchanges

the one a_1 exchange graphs, no cancellation is possible. Even the one a_1 insertion graphs are likely divergent, as evidenced by the need for additional form factor supression in the AT mass shift calculation[37]. Using our form factor approach, we find it is relatively simple to create models of a_1 exchange with improved UV behavior, which also satisfy both the low and high energy constraints.

3.2.2 Model I

Any attempt to include the effects of a_1 exchange must match onto the pion polarizability term in Eq (3.15) at low energies. At the Lagrangian level, this is generated by the interaction:

$$\mathcal{L} = -\tfrac{e^2}{2M_A^2} F_{\mu\nu} F^{\mu\nu} \pi^+ \pi^- \; . \tag{3.18}$$

Left unmodified, this term has poor UV behavior and will lead to a divergent $a_\mu^{\pi^+\pi^-}$. When viewed, however, as the first of many high energy corrections induced by integrating out the a_1 meson, a way forward is suggested. Just as the pion charge radius is often identified as the first term in the expansion of a ρ meson propagator, for our first a_1 model, we make the same assumption with the pion polarizability term and complete M_A^2 into a full propagator:

$$\mathcal{L}_{a_1} = -\frac{e^2}{4} F_{\mu\nu} \pi^+ \left(\frac{1}{D^2 + M_A^2} \right) \left(F^{\mu\nu} \pi^- \right) \quad + \text{ h.c.} \tag{3.19}$$

The Feynman rule for the $\gamma\gamma\pi\pi$ vertex is modified from Eq (3.15) to:

$$V_{a_1}^{\mu\nu} = -ie^2 (k_1 k_2 g^{\mu\nu} - k_2^\mu k_1^\nu) \left[\frac{1}{(p_1+k_1)^2 - M_A^2} + \frac{1}{(p_1+k_2)^2 - M_A^2} \right] \; . \tag{3.20}$$

The two agree at low energies, but $V_{a_1}^{\mu\nu}$ has the improved UV behavior necessary for the magnetic moment calculation. Note, however, that gauge invariance requires the use of D^2 rather than ∂^2 in Eq (3.19), and this naturally gives rise to vertices involving additional photons. We derive the Feynman rules for these interactions in the appendix. From the resulting denominator structure, the additional interactions have a direct correspondence with the graphs in Fig 3.1(b). Accordingly, we have found it simplest to express the Feynman rules of this theory in terms of the fictional a_1

exchange diagrams of Fig 3.3.

$$-e^2(k_1 k_2 g^{\mu\nu} - k_2^\mu k_1^\nu)$$

$$\frac{i}{k^2 - M_A^2}$$

$$ie(p_1^\mu + p_2^\mu)$$

$$2ie^2 g^{\mu\nu}$$

Figure 3.3: Feynman rules for a_1 exchange in Model I. The ellipsis in the first figure stands for any insertions of the subsequent diagrams.

In the limit of large photon momenta, the a_1 contribution to the $\gamma\gamma\pi\pi$ form factor approaches a constant; the QCD constraint then suggests it should be combined with the AT (or HLS) ρ prescription from Eq (3.14) which has a similar behavior. Indeed, with these ingredients, the full $\gamma\gamma\pi\pi$ form factor is given by:

$$V^{\mu\nu} = 2ie^2 \left[g^{\mu\nu}\left(1 - \frac{k_1^2}{k_1^2 - M_V^2} - \frac{k_2^2}{k_2^2 - M_V^2}\right) - \frac{1}{2}(k_1 k_2 g^{\mu\nu} - k_2^\mu k_1^\nu)\left(\frac{1}{(p_1+k_1)^2 - M_A^2} + \frac{1}{(p_1+k_2)^2 - M_A^2}\right)\right],$$
(3.21)

which, ignoring unphysical polarizations, does have the correct $1/q^2$ asymptotic behavior.

Turning to the pion mass shift calculation, we find that the improved UV behavior of our a_1 exchange model gives rise to a finite result, with no need for additional form factors. Including both ρ and a_1 exchanges, the Compton amplitude for our model is given by:

$$T^{\mu\nu}(p,q) = \left(-2 + \frac{4q^2}{q^2 - M_V^2} - \frac{q^2}{q^2 + 2pq - M_A^2 + m_\pi^2} - \frac{q^2}{q^2 - 2pq - M_A^2 + m_\pi^2}\right) D_1^{\mu\nu}$$
(3.22)
$$- 4\frac{M_V^2 m_\pi^2}{(q^2 - M_V^2)^2}\left(\frac{1}{q^2 + 2pq} + \frac{1}{q^2 - 2pq}\right) D_2^{\mu\nu},$$

where we follow the conventions of [37], with:

$$D_1^{\mu\nu} = -g^{\mu\nu} + \frac{q^\mu q^\nu}{q^2}, \tag{3.23}$$

$$D_2^{\mu\nu} = \frac{1}{p^2}\left(p^\mu - \frac{pq}{q^2}q^\mu\right)\left(p^\nu - \frac{pq}{q^2}q^\nu\right). \tag{3.24}$$

Note that this result was obtained by reinstating the k^μ terms in the form factors that were removed in Section 3.1.2. Unlike $g-2$, the mass shift calculation is not leading order in e, and these terms can not be removed without consequence. Using Eq (3.22) with $M_A = \sqrt{2}M_V$, we calculate the mass shift:

$$\delta m^2 = \frac{ie^2}{2}\int \frac{d^4q}{(2\pi)^4}\frac{g_{\mu\nu}T^{\mu\nu}(p,q)}{q^2}, \tag{3.25}$$

$$= \frac{e^2 M_V^2}{32\pi^2}\left\{12\log(2) - 2\frac{m_\pi^2}{M_V^2} + \log\left(\frac{M_V^2}{m_\pi^2}\right) - \frac{1-2m_\pi^2/M_V^2-8m_\pi^4/M_V^4}{\sqrt{1-4m_\pi^2/M_V^2}}\log\left(\frac{M_V^2(1+\sqrt{1-4m_\pi^2/M_V^2})-2m_\pi^2}{2m_\pi^2}\right)\right\}. \tag{3.26}$$

For vector meson mass $M_V = m_\rho = 775.49$ MeV, this evaluates to:

$$\Delta m_\pi = m_{\pi^\pm} - m_{\pi^0} = 5.12\text{ MeV}, \tag{3.27}$$

which agrees reasonably well with the experimental value:

$$\Delta m_{\pi,\text{ exp}} = 4.5936 \pm .0005\text{ MeV}. \tag{3.28}$$

3.2.3 Model II

Although the propagator form factor model described above is well motivated and satisfies all the constraints, it is certainly not unique. We introduce a second model here in an attempt to outline the degree of model dependence in our final result. Because the first model employs the partial VMD form factors suggested by the AT and HLS Lagrangians, we are motivated in our second model to instead use the full VMD form factors preferred by Bijnens et al. For this model of ρ exchange, the $\gamma\pi\pi$ vertex of Eq (3.13) remains unchanged, but the $\gamma\gamma\pi\pi$ vertex is altered:

$$V_{\text{VMD}}^{\mu\nu} = 2ie^2\left[g^{\mu\nu} - \frac{g^{\mu\nu}k_1^2-k_1^\mu k_1^\nu}{k_1^2-M_V^2} - \frac{g^{\mu\nu}k_2^2-k_2^\mu k_2^\nu}{k_2^2-M_V^2} + \frac{g^{\mu\nu}k_1^2k_2^2-k_1^\mu k_1^\nu k_2^2-k_2^\mu k_2^\nu k_1^2+k_1k_2k_1^\mu k_2^\nu}{(k_1^2-M_V^2)(k_2^2-M_V^2)}\right]. \tag{3.29}$$

To match onto the asymptotic behavior predicted by QCD, this implies that the a_1 contribution to the form factor must fall off as $1/q^2$. One simple way to achieve this result is to apply the VMD

form factors to the pion polarizability vertex:

$$\mathcal{L} = -\frac{e^2}{2M_A^2}\left(1 - \frac{\partial^2}{\partial^2 + M_V^2}\right)F_{\mu\nu}\left(1 - \frac{\partial^2}{\partial^2 + M_V^2}\right)F^{\mu\nu}\pi^+\pi^- \; . \tag{3.30}$$

Combined with the ρ exchanges, this leads to a $\gamma\gamma\pi\pi$ form factor,

$$V^{\mu\nu} = 2ie^2\left(1 - \frac{k_1^2}{k_1^2 - M_V^2}\right)\left(1 - \frac{k_2^2}{k_2^2 - M_V^2}\right)\left[g^{\mu\nu} + \frac{1}{M_A^2}(k_1 k_2 g^{\mu\nu} - k_2^\mu k_1^\nu)\right] \; , \tag{3.31}$$

which satisfies both the low and high energy constraints.

However, this model is not as well behaved as the previous one. Much like the AT model, two insertions of this a_1 vertex result in a divergent LBL diagram. For the $g-2$ calculation, we ignore these graphs as higher order contributions (in χPT power counting) and instead focus on the one insertion graphs which are finite. As for the pion mass shift, the Compton amplitude for this model is given by:

$$T^{\mu\nu}(p,q) = \frac{2q^2 M_V^4/M_A^2 - 2M_V^4}{(q^2 - M_V^2)^2}D_1^{\mu\nu} - 4\frac{M_V^2 m_\pi^2}{(q^2 - M_V^2)^2}\left(\frac{1}{q^2 + 2pq} + \frac{1}{q^2 - 2pq}\right)D_2^{\mu\nu} \; . \tag{3.32}$$

The first term leads to a logarithmic divergence in the mass shift integral of Eq (3.25). In retrospect, this is not surprising, and indeed should be a generic consequence for models satisfying the asymptotic $1/q^2$ form factor behavior. For the first model, a fortuitous cancellation occurs in the integral between m_π^2/q^4 and $(pq)^2/q^6$ terms to give a convergent result. Despite these shortcomings, our VMD model does satisfy the known constraints, and, at one insertion, provides a finite correction to the $g-2$ calculation. Armed now with two different models of a_1 exchange, we turn, at last, to their effect on the magnetic moment of the muon. This complicated calculation is discussed in the next section.

Chapter 4

$g - 2$ calculation

The charged pion contribution to a_μ is a three loop process and is therefore simplest to evaluate numerically. We begin by reviewing a general method for turning momentum space integrals into bounded integrals appropriate for numeric evaluation. Next, we discuss some aspects of this particular calculation which allow for a reduction in both the number of graphs necessary to consider and the size and complexity of the resultant integrand. We present the LO graphs and give a detailed description of our process for one of them. Finally, we turn to the a_1 corrections, giving the necessary graphs for Models I and II, and discussing the slight alterations to our methods that are required to evaluate these contributions.

4.1 Parametric formulation of Feynman integrals

For numeric evaluations of multi-loop Feynman diagrams, the parametric formulation is a useful tool. In this method, integrals over loop momenta are done simultaneously, leaving behind functions of Feynman parameters which can be integrated numerically. This process is described in detail in Ref [41]; we present a brief summary here.

Consider an arbitrary Feynman diagram with n propagators, m loop momenta l_i^μ, and some number of external momenta k_j^μ. If each propagator is assigned a Feynman parameter, then the full amplitude can be written as:

$$\iiint \frac{d^4 l_1}{(2\pi)^4} \frac{d^4 l_2}{(2\pi)^4} \dots \iiint\limits_{0}^{1} dx_1 dx_2 \dots \delta(1 - \Sigma x_i) \text{Num}(l_i^\mu, k_j^\mu) \Gamma(n) \left(\sum_{i=1}^{n} x_i(p_i^2 - m_i^2) \right)^{-n}. \quad (4.1)$$

Here p_i, the momenta flowing through the ith propagator, is obviously a linear combination of the loop and external momenta. Factors from vertices and the like have been grouped together into the single function $\text{Num}(l_i^\mu, k_j^\mu)$.

To begin with, we consider the special case where the numerator does not depend on the loop momenta l_i^μ. We focus on the denominator, dropping Lorentz indices for convenience and rewriting
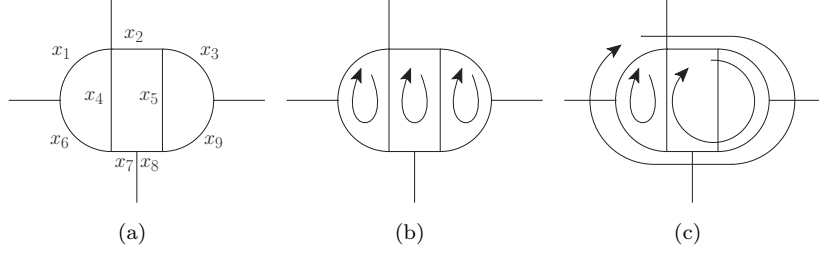
Figure 4.1: 3-loop diagram with different choices of loop momenta

it to illustrate the loop momenta dependence:

$$(l_i U_{ij}(x)l_j + 2l_i A_{ij}(x)k_j - f(k,m,x)) \,. \tag{4.2}$$

Here $U_{ij}(x)$ is a symmetric $m \times m$ matrix which depends on the choice of loops. As an example, Fig 4.1 shows the same diagram with two different routings of the three loop momenta. Using the parameterization from Fig 4.1(a), the two loop momenta coupling matrices are:

$$U^{(b)} = \begin{pmatrix} x_1 + x_4 + x_6 & -x_4 & 0 \\ -x_4 & x_2 + x_4 + x_5 + x_7 + x_8 & -x_5 \\ 0 & -x_5 & x_3 + x_5 + x_9 \end{pmatrix}, \tag{4.3}$$

$$U^{(c)} = \begin{pmatrix} x_1 + x_4 + x_6 & -x_4 & x_1 + x_6 \\ -x_4 & x_2 + x_3 + x_4 + x_7 + x_8 + x_9 & x_2 + x_3 + x_7 + x_8 + x_9 \\ x_1 + x_6 & x_2 + x_3 + x_7 + x_8 + x_9 & x_1 + x_2 + x_3 + x_6 + x_7 + x_8 + x_9 \end{pmatrix}. \tag{4.4}$$

$A_{ij}(x)$ couples the loop momenta to the external momenta and clearly depends on how the external momenta are routed through the diagram. $f(k,m,x)$ is a function composed of invariants of the external momenta and the various particle masses.

In this form, the integral over the loop momenta is relatively straightforward. We first remove the linear term with the redefinition $l = \tilde{l} - U^{-1}Ak$, which results in the denominator:

$$\left(\tilde{l}U(x)\tilde{l} - V(k,m,x)\right), \tag{4.5}$$

where we have defined

$$V(k,m,x) = (A(x)k)_i U_{ij}^{-1}(x)(A(x)k)_j + f(k,m,x). \tag{4.6}$$

As a symmetric matrix, U can be diagonalized by an orthogonal transformation which we implement

through $\hat{l} = T(x)\tilde{l}$. The resultant loop integrals are quite simple:

$$\sim \iiint \frac{d^4\hat{l}_1}{(2\pi)^4} \frac{d^4\hat{l}_2}{(2\pi)^4} \cdots \left(\sum_{i=1}^{m} c_i \hat{l}_i^2 - V\right)^{-n} \Gamma(n),$$

(4.7)

where c_i are the eigenvalues of U. Using dimensional regularization, the loop integrals evaluate to:

$$\frac{i^m(-1)^n}{\left(\prod_i^m c_i\right)^{d/2} (4\pi)^{md/2}} \Gamma(n - md/2) \left(\frac{1}{V}\right)^{n-md/2}.$$

(4.8)

Rewriting $\prod_i^m c_i$ as $\det U$, we find that the full amplitude is given as:

$$\int\limits_0^1 \!\!\!\iint dx_1 dx_2 \ldots \delta(1 - \mathbf{\Sigma} x_i) \mathrm{Num}(k_j^\mu) \frac{i^m(-1)^n}{(4\pi)^{md/2}} \Gamma(n - md/2) \frac{1}{(\det U(x))^{d/2}} \left(\frac{1}{V(k,m,x)}\right)^{n-md/2}.$$

(4.9)

This formalism can be easily extended to include numerators which do depend on the loop momenta. For each l_i, we introduce a source momentum and mass by modifying the existing propagator:

$$\frac{1}{l_1^2 - m^2} \rightarrow \frac{1}{l_1^2 + 2q_1 l_1 - m_1^2}.$$

(4.10)

Now, an l_1^μ in the numerator can be achieved through a derivative with respect to the source momenta:

$$\frac{l_1^\mu}{l_1^2 - m^2} = D_1^\mu \frac{1}{l_1^2 + 2q_1 l_1 - m_1^2}\bigg|_{\substack{q_1=0 \\ m_1=m}},$$

(4.11)

where

$$D_i^\mu \equiv -\frac{1}{2} \int^{m_i^2} \frac{\partial}{\partial q_{i\mu}} dm_i^2.$$

(4.12)

With the substitution $\mathrm{Num}(l_i^\mu, k_j^\mu) \rightarrow \mathrm{Num}(D_i^\mu, k_j^\mu)$, the numerator is made independent of the loop momenta and the previous analysis can be repeated, but now with an expanded $A_{ij}(x)$ which includes couplings to the source momenta. The full amplitude is then given by:

$$\int\limits_0^1 \!\!\!\iint dx_1 dx_2 \ldots \delta(1 - \mathbf{\Sigma} x_i) \frac{i^m(-1)^n}{(4\pi)^{md/2}} \Gamma(n - md/2)$$

$$\frac{1}{(\det U(x))^{d/2}} \mathrm{Num}(D_i^\mu, k_j^\mu) \left(\frac{1}{V(k,m,x,q_i,m_i)}\right)^{n-md/2}\bigg|_{\substack{q_i \to 0 \\ m_i \to m}},$$

(4.13)

where we set $q_i \to 0$ and return m_i to the original mass m after all the derivatives with respect to the source momenta have been taken. The end result is a function of external momenta invariants,

particle masses, and Feynman parameters whose bounded integral can be evaluated numerically.

4.2 Symmetries and simplifications for LBL $g - 2$ calculation

We use the general formalism described in the previous section to calculate three loop charged pion contributions to the muon magnetic moment. For this particular calculation, however, we can employ some additional tricks to help simplify the result.

As shown in Fig 1.1, the relevant diagrams arise by attaching three photon lines from the LBL subdiagrams to a muon line. We find it convenient to isolate the LBL part and write the amplitude as:

$$\mathcal{M}^\mu = \iint \frac{d^4 k_2}{(2\pi)^4} \frac{d^4 k_3}{(2\pi)^4} \mathrm{ML}_{\nu\sigma\rho}(p, q, k_2, k_3) \Pi^{\mu\nu\sigma\rho}(q, k_2, k_3, -q - k_2 - k_3). \tag{4.14}$$

This generates an $\mathcal{O}(\alpha^3)$ correction to the muon vertex function which is paramaterized as:

$$\Gamma^\mu(q) = \gamma^\mu \mathrm{F}_1(q^2) + \frac{i\sigma^{\mu\nu} q_\nu}{2m_\mu} \mathrm{F}_2(q^2). \tag{4.15}$$

For this calculation, we concern ourselves only with contributions to F_2, since the anomalous magnetic moment is given by $a_\mu \equiv (g_\mu - 2)/2 = \mathrm{F}_2(0)$. Therefore, any terms in Eq (4.14) which are not linear in q can be safely ignored.

We have purposefully separated out the LBL subdiagram to take advantage of its q dependence. The Ward-Takahashi identity for LBL is quite simple: $q_\alpha \Pi^{\alpha\nu\sigma\rho} = 0$, as it relates the four photon amplitude to the three photon one, which must vanish according to Furry's Theorem. By differentiating with respect to q^μ, we find:

$$\Pi^{\mu\nu\sigma\rho} = -q_\alpha \frac{\partial \Pi^{\alpha\nu\sigma\rho}}{\partial q^\mu}. \tag{4.16}$$

This enormously simplifies the magnetic moment calculation, since the linear q dependence of the LBL subdiagram allows us to set $q \to 0$ everywhere else:

$$\mathcal{M}^\mu \sim \iint \frac{d^4 k_2}{(2\pi)^4} \frac{d^4 k_3}{(2\pi)^4} \mathrm{ML}_{\nu\sigma\rho}(p, k_2, k_3)(-q_\alpha) \frac{\partial \Pi^{\alpha\nu\sigma\rho}(q, k_2, k_3, -q - k_2 - k_3)}{\partial q^\mu} \bigg|_{q=0}. \tag{4.17}$$

The incoming muon momentum p is now the only external momenta which appears in the denominator, and, if routed along the muon line, it enters the same way, regardless of the individual subdiagrams which make up LBL. As we will demonstrate shortly, this allows us to use the same denominator (and therefore the same parametric functions U and V) for every contributing diagram.

Incidentally, this prescription has the additional advantage of rendering individual LBL diagrams finite. In its initial form, the LBL diagrams are divergent, cancelling only in the aggregate sum. However, if Eq (4.16) is used before integrating over the loop momenta, each diagram is individually
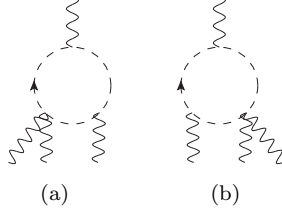
Figure 4.2: Mirror image LBL diagrams

convergent. In this way, we can avoid the extra processing which would have been required to numerically evaluate divergent diagrams[42].

Some simplification can also be achieved in the numerator structure. For an individual diagram, the only structures left at the end will be proportional to $p^\mu \slashed{q}, \gamma^\mu \slashed{q}, \slashed{q}\gamma^\mu$, and q^μ. The first one vanishes when sandwiched between $\overline{u}(p+q)$ and $u(p)$ and can be neglected. The remaining three are not independent and can be related by anti-commuting gamma matrices:

$$\slashed{q}\gamma^\mu = -\gamma^\mu \slashed{q} + 2q^\mu \,. \tag{4.18}$$

This leaves two distinct structures whose coefficients will have to be calculated for each diagram. However, gauge invariance requires the overall sum of the diagrams to be proportional to:

$$\frac{i\sigma^{\mu\nu}}{2m_\mu}q_\nu = -\frac{1}{4m_\mu}\left(\gamma^\mu \slashed{q} + \slashed{q}\gamma^\mu\right) = -\frac{1}{2m_\mu}\left(\gamma^\mu \slashed{q} - q^\mu\right)\,. \tag{4.19}$$

Rather than duplicate effort, we cut the size of the calculation in half by finding only the coefficient of $\gamma^\mu \slashed{q}$. Throughout the calculation, we cull from the numerator all terms proportional to p^μ or q^μ (in addition to occuring in the intial amplitude, these terms can arise as gamma matrices are contracted or when loop momenta are replaced by factors of p).

Two other symmetries are useful for this project, reducing the number of diagrams which need to be considered. Charge conjugation symmetry implies that LBL subdiagrams which differ only in the directionality of the pion loop have the same value. The second symmetry is not as obvious, but as we show below, it relates the magnetic moment contributions from LBL diagrams which are mirror images.

Consider the two LBL diagrams in Fig 4.2 with photon momenta q^μ flowing into the pion loop from above and k_2^ν, $-q^\rho - k_2^\rho - k_3^\rho$, k_3^σ from left to right respectively flowing in from below. If we denote the amplitude of graph (a) as $\Pi_a^{\mu\nu\sigma\rho}(q, k_2, k_3)$, then clearly the amplitude of graph (b) can be found by exchanging k_2^ν and k_3^σ:

$$\Pi_b^{\mu\nu\sigma\rho}(q, k_2, k_3) = \Pi_a^{\mu\sigma\nu\rho}(q, k_3, k_2)\,. \tag{4.20}$$

The total contribution of the two graphs to the muon vertex function is given by:

$$\mathcal{M}^\mu \sim \iint \frac{d^4k_2}{(2\pi)^4}\frac{d^4k_3}{(2\pi)^4}\mathrm{ML}_{\nu\sigma\rho}(p,k_2,k_3)(-q_\alpha)\left(\frac{\partial\Pi_a^{\alpha\nu\sigma\rho}(q,k_2,k_3)}{\partial q^\mu}+\frac{\partial\Pi_a^{\alpha\sigma\nu\rho}(q,k_3,k_2)}{\partial q^\mu}\right)\Bigg|_{q=0},$$
(4.21)

or equivalently:

$$\mathcal{M}^\mu \sim \iint \frac{d^4k_2}{(2\pi)^4}\frac{d^4k_3}{(2\pi)^4}\left(\mathrm{ML}_{\nu\sigma\rho}(p,k_2,k_3)+\mathrm{ML}_{\sigma\nu\rho}(p,k_3,k_2)\right)(-q_\alpha)\frac{\partial\Pi_a^{\alpha\nu\sigma\rho}(q,k_2,k_3)}{\partial q^\mu}\Bigg|_{q=0}.$$
(4.22)

Using the Feynman gauge, the muon line part is given by:

$$\mathrm{ML}_{\nu\sigma\rho}(p,k_2,k_3)=\frac{e^3\gamma^\sigma(\not{p}+\not{k_3}+m_\mu)\gamma^\rho(\not{p}-\not{k_2}+m_\mu)\gamma^\nu}{((p+k_3)^2-m_\mu^2)((p-k_2)^2-m_\mu^2)k_2^2k_3^2(k_2+k_3)^2}$$
(4.23)

$$
\begin{aligned}
=\Big\{&\gamma^\sigma\gamma^\alpha\gamma^\rho\gamma^\beta\gamma^\nu(p_\alpha+k_{3\alpha})(p_\beta-k_{2\beta})+\\
&\gamma^\sigma\gamma^\alpha\gamma^\rho\gamma^\nu m_\mu(p_\alpha+k_{3\alpha})+\\
&\gamma^\sigma\gamma^\rho\gamma^\alpha\gamma^\nu m_\mu(p_\alpha-k_{2\alpha})+\\
&\gamma^\sigma\gamma^\rho\gamma^\nu m_\mu^2\Big\}\frac{e^3}{((p+k_3)^2-m_\mu^2)((p-k_2)^2-m_\mu^2)k_2^2k_3^2(k_2+k_3)^2}.
\end{aligned}
$$

For the sake of comparison, we also write out $\mathrm{ML}_{\sigma\nu\rho}(p,k_3,k_2)$, suggestively relabeling the dummy indices so that the order of the gamma matrices is flipped:

$$
\begin{aligned}
\mathrm{ML}_{\sigma\nu\rho}(p,k_3,k_2)=\Big\{&\gamma^\nu\gamma^\beta\gamma^\rho\gamma^\alpha\gamma^\sigma(p_\alpha-k_{3\alpha})(p_\beta+k_{2\beta})+\\
&\gamma^\nu\gamma^\rho\gamma^\alpha\gamma^\sigma m_\mu(p_\alpha-k_{3\alpha})+\\
&\gamma^\nu\gamma^\alpha\gamma^\rho\gamma^\sigma m_\mu(p_\alpha+k_{2\alpha})+\\
&\gamma^\nu\gamma^\rho\gamma^\sigma m_\mu^2\Big\}\frac{e^3}{((p-k_3)^2-m_\mu^2)((p+k_2)^2-m_\mu^2)k_2^2k_3^2(k_2+k_3)^2}.
\end{aligned}
$$
(4.24)

In our $g-2$ calculation, loop momenta in the numerator can do one of two things: contract with one another to form metrics, or pull out factors of external momentum p from the parametric function V. Note, however, that the pk_2 and pk_3 couplings differ by a minus sign in the denominator of the two muon lines. If, in the first case, one of these loop momenta pulls down a factor of p^α, then in the second one it will pull down a factor of $-p^\alpha$. We will now show that this implies that the two muon lines give the same contribution to a_μ.

In order for the three γ part of $\mathrm{ML}_{\nu\sigma\rho}$ to contribute to the coefficient of $\gamma^\mu\not{q}$, one of the γ must be contracted into p, e.g. $\sim \not{p}\gamma^\mu\not{q}$. Note that the position of $\not{p}$ is not terribly significant for this calculation. Because we can drop p^μ terms and pq is $\mathcal{O}(q^2)$, any $\not{p}$ can be moved to the right, and,
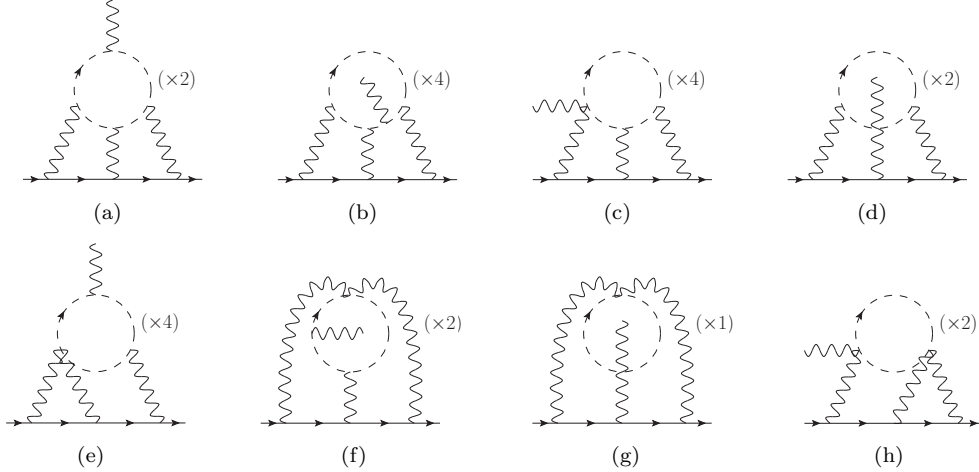
Figure 4.3: LO charged pion contributions to the muon magnetic moment

using $\not{p}u(p) = m_\mu u(p)$, turned into a factor of m_μ. If $\not{p}$ occurs between γ^μ and $\not{q}$, then only one anti-commutation takes place and a minus sign must be appended.

The corresponding part of the second muon line $\text{ML}_{\sigma\nu\rho}$ has the same numerator and will therefore generate the exact same term, but now, the order of the gamma matrices is flipped and a $-p$ is contracted: $\sim \not{q}\gamma^\mu(-\not{p})$. We anticommute $\not{q}$ and γ^μ, (discarding the q^μ term that is generated) thereby picking up an additional minus sign for the $\gamma^\mu\not{q}$ coefficient. It should now be clear that any three γ contribution from the first muon line is reproduced by the second one, as the minus sign on p is cancelled by exchanging γ^μ and $\not{q}$. Similar reasoning can be applied to the four and five γ parts of the muon lines, where now some combination of metrics and p contractions contribute to the $\gamma^\mu\not{q}$ coefficient. The minus sign from the flipped order is always cancelled out, allowing us to conclude that diagrams (a) and (b) contribute equally to the magnetic moment. More generally, any pair of graphs which have the same left-right mirror symmetry with respect to the muon line will give equal contributions to a_μ.

4.3 Leading order calculation

The symmetries discussed in the previous section greatly reduce the number of diagrams which must be considered in the LO a_μ^{LBL} calculation. These graphs (and appropriate symmetry factors) are shown in Fig 4.3. In order to demonstrate our specific implementation of the general formalism discussed earlier, we present, in detail, our calculation of the magnetic moment contribution from graph 4.3(a).

We begin by choosing the loop momenta and routing the external momenta through the diagram; our labeling is shown in Fig 4.4. We make similar choices for all the diagrams in Fig 4.3 - the pion loop is assigned clockwise momenta l, the left-most photon loop is assigned clockwise momenta k_2,
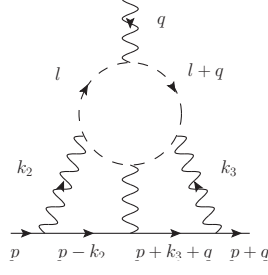
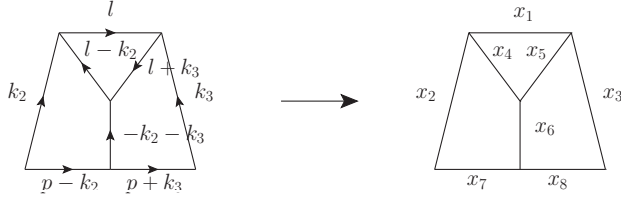Figure 4.4: Momentum labeling for graph 4.3(a)

Figure 4.5: Feynman parameter assignment for the graphs of Fig 4.3

and the right-most one is chosen anti-clockwise with loop momenta k_3.

Next, we write down just the LBL amplitude (including the symmetry factor here):

$$\Pi_a^{\mu\nu\sigma\rho} = \int \frac{d^4l}{(2\pi)^4} \frac{2e^4(2l^\mu + q^\mu)(2l^\nu - k_2^\nu)(2l^\sigma + k_3^\sigma + 2q^\sigma)(2l^\rho - k_2^\rho + k_3^\rho + q^\rho)}{(l^2 - m_\pi^2)((l+q)^2 - m_\pi^2)((l+k_3+q)^2 - m_\pi^2)((l-k_2)^2 - m_\pi^2)}. \tag{4.25}$$

Eq (4.16) is then used to isolate the linear q dependence:

$$\Pi_a^{\mu\nu\sigma\rho} \sim \int \frac{d^4l}{(2\pi)^4} \frac{2e^4 2ql(2l^\nu - k_2^\nu)}{(l^2 - m_\pi^2)^2((l+k_3)^2 - m_\pi^2)((l-k_2)^2 - m_\pi^2)}\bigg\{$$
$$- 2g^{\mu\sigma}(2l^\rho - k_2^\rho + k_3^\rho) - g^{\mu\rho}(2l^\sigma + k_3^\sigma)$$
$$+ (2l^\sigma + k_3^\sigma)(2l^\rho - k_2^\rho + k_3^\rho)\left(\frac{2l^\mu}{l^2 - m_\pi^2} + \frac{2(l^\mu + k_3^\mu)}{(l+k_3)^2 - m_\pi^2}\right)\bigg\}. \tag{4.26}$$

As discussed earlier, we have dropped a term proportional to q^μ from our result. Although the numerator is now more complicated, the denominator is simpler, involving only three distinct propagators which no longer depend on q.

We now assign a Feynman parameter to each propagator; this is shown schematically in Fig 4.5. Combining the propagators into a common denominator and comparing with Eq (4.2) gives (using the basis $l_i = (l, k_2, k_3)$):

$$U(x) = \begin{pmatrix} x_1 + x_4 + x_5 & -x_4 & x_5 \\ -x_4 & x_2 + x_4 + x_6 + x_7 & x_6 \\ x_5 & x_6 & x_3 + x_5 + x_6 + x_8 \end{pmatrix} , \qquad (4.27)$$

$$A^\mu(x) \equiv A_{ij}(x)k_j^\mu = \begin{pmatrix} x_1 q_1^\mu \\ x_2 q_2^\mu - x_7 p^\mu \\ x_3 q_3^\mu + x_8 p^\mu \end{pmatrix} , \qquad (4.28)$$

$$f = m_1^2 x_1 + m_2^2 x_2 + m_3^2 x_3 + m_\pi^2 (x_4 + x_5) , \qquad (4.29)$$

where source momenta and masses have been introduced for the three loop momenta. The parametric function V can now be directly calculated using Eq (4.6). For convenience, we parameterize V as:

$$V = \Big[\tfrac{1}{U} \big(c_1 x_1^2 q_1^2 + c_2 x_2^2 q_2^2 + c_3 x_3^2 q_3^2 + 2c_4 x_1 x_2 q_1 q_2 + 2c_5 x_1 x_3 q_1 q_3 + 2c_6 x_2 x_3 q_2 q_3 \big) \qquad (4.30)$$

$$+ 2c_7 x_1 p q_1 + 2c_8 x_2 p q_2 + 2c_9 x_3 p q_3 + c_{10} m_\mu^2 + f \Big] . \qquad (4.31)$$

In a slight abuse of notation we use U here to refer to $\det U$ of the matrix in Eq (4.27). It should be clear from the context which one is meant. This factor is generated from the inverse matrix in Eq (4.6); we include it explicitly in the first six coefficients so that the overall exponent of U in the final answer is directly correlated with the number of momentum contractions. The ten c's are functions of the Feynman parameters and their values can be found in the Appendix.

Turning back to the numerator, we find it separates into two parts, one where the total number of propagators $n = 9$, and one with $n = 10$:

$$\text{Num}_9^\mu = \text{MLnum}_{\nu\sigma\rho} \big[x_1 e^4 4ql(2l^\nu - k_2^\nu)(-2g^{\mu\sigma}(2l^\rho - k_2^\rho + k_3^\rho) - g^{\mu\rho}(2l^\sigma + k_3^\sigma)) \big] , \qquad (4.32)$$

$$\text{Num}_{10}^\mu = \text{MLnum}_{\nu\sigma\rho} \big[e^4 8ql(2l^\nu - k_2^\nu)(2l^\sigma + k_3^\sigma)(2l^\rho - k_2^\rho + k_3^\rho)(\tfrac{1}{2} x_1^2 l^\mu + x_1 x_5 (l^\mu + k_3^\mu)) \big] . \qquad (4.33)$$

$\text{MLnum}_{\nu\sigma\rho}$ is, of course, the numerator of the muon line, given by:

$$\text{MLnum}_{\nu\sigma\rho} = e^3 \gamma^\sigma (\slashed{p} + \slashed{k}_3 + m_\mu) \gamma^\rho (\slashed{p} - \slashed{k}_2 + m_\mu) \gamma^\nu . \qquad (4.34)$$

The Feynman parameters in the LBL numerator account for the different multiplicities of the propagators in Eq (4.26).

As we have shown previously, we can replace numerator loop momenta with derivatives with

respect to source momenta, finally allowing us to write:

$$\mathcal{M}_a^\mu = \int\!\!\!\int\!\!\!\int_0^1 dx_1 dx_2 \ldots \delta(1 - \mathbf{\Sigma} x_i) \frac{i}{(4\pi)^{3d/2} U^{d/2}} \left\{ \mathrm{Num}_9^\mu(p^\alpha, D_i^\alpha) \left(\frac{1}{V}\right)^{9-3d/2} \Gamma(9 - 3d/2) \right.$$

$$\left. - \mathrm{Num}_{10}^\mu(p^\alpha, D_i^\alpha) \left(\frac{1}{V}\right)^{10-3d/2} \Gamma(10 - 3d/2) \right\} \bigg|_{\substack{q_i \to 0 \\ m_1 \to m_\pi \\ m_2, m_3 \to 0}} . \tag{4.35}$$

The loop momentum integrals have been replaced with integrals over Feynman parameters. The only remaining hurdles are performing the source momentum derivatives, extracting the $\gamma^\mu \slashed{q}$ coefficient, and numerically integrating the result.

With Eq (4.35) as the starting point, the remaining processing can be accomplished by computer programs. We have written one which evaluates the source momentum derivatives, then simplifies the ensuing contractions into gamma matrices. As was mentioned previously, in order to survive the $q_i \to 0$ limit, each loop momentum in the numerator must either pull out a factor of p from V, or contract with another loop momentum. As an example, we consider one of the many terms in Eq (4.32):

$$-16 e^7 x_1 m_\mu \gamma^\sigma \slashed{p} \gamma^\rho \gamma^\nu q l \, l^\nu k_3^\rho g^{\mu\sigma} . \tag{4.36}$$

The loop momenta become source momenta derivatives which act on V:

$$q D_1 D_1^\nu D_3^\rho \left(\frac{1}{V}\right)^{9-3d/2} \Gamma(9 - 3d/2) \bigg|_{\substack{q_i \to 0 \\ m_1 \to m_\pi \\ m_2, m_3 \to 0}} . \tag{4.37}$$

Using the parameterization of V from Eq (4.31), this is easily evaluated:

$$= q p \, p^\nu p^\rho (-c_7^2 c_9) \left(\frac{1}{V}\right)^{9-3d/2} \Gamma(9 - 3d/2) +$$

$$\left[q p \, g^{\nu\rho} \frac{c_5 c_7}{2U} + q^\nu p^\rho \frac{c_1 c_9}{2U} + q^\rho p^\nu \frac{c_5 c_7}{2U} \right] \left(\frac{1}{V}\right)^{8-3d/2} \Gamma(8 - 3d/2) . \tag{4.38}$$

Of course, half the terms here would be immediately discarded since qp is $\mathcal{O}(q^2)$. The remaining terms are contracted into the gamma matrices, $\slashed{p}$ are transformed into m_μ, and the coefficient of $\gamma^\mu \slashed{q}$ is extracted. This process is repeated for each term in the numerator. We arrive at last, at an expression for the magnetic moment contribution due to diagram (a):

$$a_\mu = \frac{2e^6}{(4\pi)^{3d/2}} \int\!\!\!\int\!\!\!\int_0^1 dx_1 dx_2 \ldots \delta(1 - \mathbf{\Sigma} x_i) \left\{ \mathrm{num}_7 \, U^{-3-d/2} \left(\frac{1}{V}\right)^{7-3d/2} \Gamma(7 - 3d/2) + \right.$$

$$\left. \mathrm{num}_8 \, U^{-2-d/2} \left(\frac{1}{V}\right)^{8-3d/2} \Gamma(8 - 3d/2) \right\} , \tag{4.39}$$

where num$_7$ and num$_8$ are complicated functions of c_i, U, and d; they are given explicitly in the appendix. The parametric function V in this expression is now the physical one with $q_i \to 0$, $m_1 \to m_\pi$, and $m_2, m_3 \to 0$. We have also rescaled by m_μ^2 to make it a dimensionless quantity:

$$V \equiv \frac{m_\pi^2}{m_\mu^2}(x_1 + x_4 + x_5) + c_{10}\,. \tag{4.40}$$

As we will demonstrate in Section 5.1, this integral is finite, therefore we can take the $d \to 4$ limit and evaluate numerically.

The remaining diagrams in Fig 4.3 can be evaluated the same way. Note that our convention of routing momentum q through the middle photon line implies that the LBL amplitude of graphs 4.3(d) and 4.3(g) does not depend on q, and accordingly gives no contribution to a_μ. For the remaining graphs, we impose the same denominator structure displayed in Fig 4.5. This ensures that each diagram has the same parametric functions U and V, differing only in the numerator functions. This will prove useful during the numeric integration. Some graphs intially lack all eight propagators; we 'fix' these by multiplying both numerator and denominator by the missing propagator. For example, graph 4.3(h), which consists of only seven propagators, contributes the following numerator to Eq (4.35):

$$\text{Num}_9^\mu = \text{MLnum}_{\nu\sigma\rho} \left[8e^4 q^\nu g^{\sigma\rho}((l + k_3)^2 - m_\pi^2)x_4(-l^\mu + k_2^\mu) \right]\,. \tag{4.41}$$

The final and complete expression for the LO $a_\mu^{\pi^+\pi^-}$ can be written as in Eq (4.39), but with num$_7$ and num$_8$ which contain contributions from all the graphs in Fig 4.3.

4.4   VMD corrected result

In the full VMD model, each photon is supplemented by the form factor $(1 - \frac{k^2}{k^2 - M_V^2})$. Including the k^{-2} from the photon propagator, the photon denominator structure which includes VMD corrections takes the form:

$$\left(\frac{1}{k_2^2} - \frac{1}{k_2^2 - M_V^2} \right) \left(\frac{1}{k_3^2} - \frac{1}{k_3^2 - M_V^2} \right) \left(\frac{1}{(k_2 + k_3)^2} - \frac{1}{(k_2 + k_3)^2 - M_V^2} \right)\,. \tag{4.42}$$

Incorporating VMD corrections is apparently quite simple! The original LO denominator of $\frac{1}{k_2^2 k_3^2 (k_2+k_3)^2}$ is expanded into permutations of massless and massive photon lines, resulting in an alteration of V by $\frac{M_V^2}{m_\mu^2} x_i$ terms. Because only the denominator is affected, the full VMD result is a simple extension

of the LO calculation, found by replacing $\left(\frac{1}{V}\right)^{n-3d/2}$ in Eq (4.39) with:

$$\left\{\left(\frac{1}{V}\right)^{n-3d/2} - \left(\frac{1}{V_2}\right)^{n-3d/2} - \left(\frac{1}{V_3}\right)^{n-3d/2} - \left(\frac{1}{V_6}\right)^{n-3d/2} + \right.$$
$$\left. \left(\frac{1}{V_{23}}\right)^{n-3d/2} + \left(\frac{1}{V_{26}}\right)^{n-3d/2} + \left(\frac{1}{V_{36}}\right)^{n-3d/2} - \left(\frac{1}{V_{236}}\right)^{n-3d/2}\right\}, \tag{4.43}$$

where $V_2 = V + \frac{M_V^2}{m_\mu^2}x_2$, $V_{23} = V + \frac{M_V^2}{m_\mu^2}(x_2 + x_3)$, etc.

For the partial VMD corrections suggested by the HLS and AT models, the two photon vertex is treated differently than the one photon vertex with form factor $\left(1 - \frac{k_1^2}{k_1^2-M_V^2} - \frac{k_2^2}{k_2^2-M_V^2}\right)$. This results in a slightly different prescription for some graphs: (a)-(c) remain unchanged from the full VMD result, but for graph (e), the V_{26} and V_{236} terms are removed, for graph (f), V_{23} and V_{236} are removed, and for graph (h), V_{36} and V_{236} are removed.

4.5 a_1 corrections

Unlike the VMD corrections, contributions from a_1 exchange cannot be written as simple modifications of the LO diagrams and must be calculated separately. The necessary graphs are shown in Figs 4.6 and 4.7 for Model I and II respectively. We have again included symmetry factors from charge conjugation and mirror symmetry.

In Fig 4.7 the cross symbol denotes an insertion of the interaction vertex from Eq (3.30). These Model II graphs differ from the LO ones only in the numerator structure and are therefore evaluated in the same way. For Model I, however, some slight complications arise, falling into two different categories. For diagrams such as 4.6(a), the usual denominator structure can be used, slightly modified to include mass M_A for the a_1 propagator. This results in magnetic moment contributions as in Eq (4.39), but now with V which depends on M_A. For diagram 4.6(a), for example:

$$V \to V_{A4} = \frac{m_\pi^2}{m_\mu^2}(x_1 + x_5) + \frac{M_A^2}{m_\mu^2}x_4 + c_{10}. \tag{4.44}$$

The other class of diagrams appear more challenging as the same propagator can occur with different masses. This arises whenever q flows into an $a_1\gamma\pi$ vertex. Diagram 4.6(i), for example, contains the two propagators $(l^2 - m_\pi^2)^{-1}$ and $(l^2 - M_A^2)^{-1}$. Rather than adding another Feynman parameter to account for this extra propagator, we use the identity:

$$\frac{1}{(l^2 - m_\pi^2)(l^2 - M_A^2)} = \frac{1}{m_\pi^2 - M_A^2}\left[\frac{1}{l^2 - m_\pi^2} - \frac{1}{l^2 - M_A^2}\right]. \tag{4.45}$$

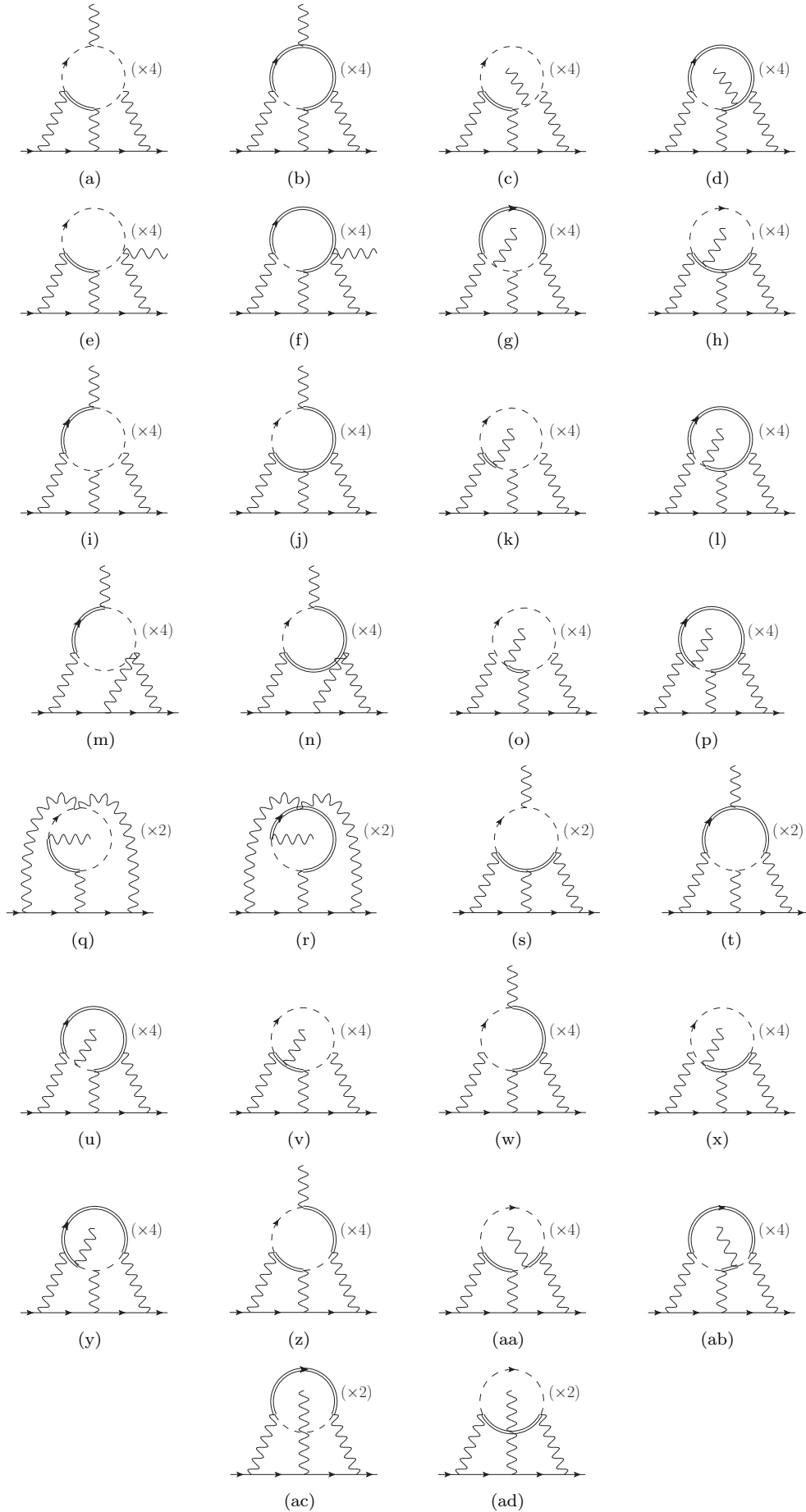The standard U and V functions can once again be used, but now the number of propagators has

Figure 4.6: Model I a1 exchange diagrams which contribute to the muon magnetic moment
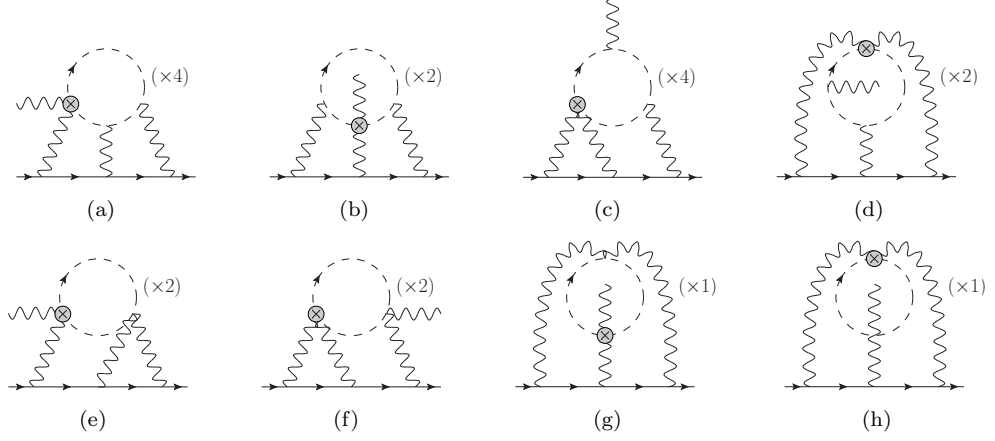
Figure 4.7: Model II a1 exchange diagrams which contribute to the muon magnetic moment

been reduced by one. Contributions from these graphs accordingly occur in the form:

$$a_\mu = \frac{2e^6}{(4\pi)^{3d/2}} \int\!\!\!\int\!\!\!\int_0^1 dx_1 dx_2 \ldots \delta(1 - \mathbf{\Sigma}x_i) \frac{m_\mu^2}{m_\pi^2 - M_A^2} \Bigg\{$$

$$\text{num}_6\, U^{-2-d/2} \left[\left(\frac{1}{V}\right)^{6-3d/2} - \left(\frac{1}{V_A}\right)^{6-3d/2} \right] \Gamma(6 - 3d/2) +$$

$$\text{num}_7\, U^{-1-d/2} \left[\left(\frac{1}{V}\right)^{7-3d/2} - \left(\frac{1}{V_A}\right)^{7-3d/2} \right] \Gamma(7 - 3d/2) \Bigg\}, \quad (4.46)$$

where, of course, V_A is the modified form factor which accounts for the a_1 mass; for graph 4.6(i) $V_A \to V_{A1} = V + \left(\frac{M_A^2}{m_\mu^2} - \frac{m_\pi^2}{m_\mu^2}\right)x_1$. Note that despite the ominous gamma function, the num_6 contribution is still finite - the V functions combine with $\Gamma(6 - 3d/2)$ in the $d \to 4$ limit to give $-\frac{3}{2}\log\left(\frac{V}{V_A}\right)$.

Finally, we point out that the diagrams in Fig 4.6 have intentionally been grouped in pairs. For this particular model of a_1 exchange, graphs (a) and (b), (c) and (d), etc. share the same numerator structure, differing only in the mass assignments which show up in V. Only graphs (w) and (z) remain unpaired as their partner is related by the mirror symmetry which we have encoded in the symmetry factor.

The full $a_\mu^{\pi^+\pi^-}$ is given by adding the contribution from the ρ corrected LO graphs of Fig 4.3 to one of the sets of a_1 graphs in Fig 4.6 or Fig 4.7. As per the discussion in Section 3.2.1, the ρ prescription must be matched to the correct a_1 model in order to satisfy all the constraints on the pion form factors. Furthermore, a consistent calculation should also include ρ corrections for the LO $\gamma\pi\pi$ and $\gamma\gamma\pi\pi$ vertices which appear in the a_1 diagrams. Just as in the LO case, these additional effects can be easily incorporated as a modification of the V functions.

Chapter 5

Numeric integration

We have seen that the various charged pion magnetic moment contributions can be put into the form of either Eq (4.39) or (4.46). We evaluate these integrals numerically, setting $d \to 4$ and using a MISER Monte Carlo algorithm. A number of improvements are discussed, most notably a partitioning of the overall integral into various subregions which, under a set of variable changes, allow for square convergent integrals, resulting in speedy evaluation with small errors.

5.1 Taking $d \to 4$

Using the parametric formulation, the amplitude for any diagram can be written in the form:

$$\iiint\limits_0^1 dx_1 dx_2 \ldots \delta(1 - \mathbf{\Sigma} x_i) \frac{\text{num}}{U^{a+d/2} V^{b-md/2} (4\pi)^{md/2}} \Gamma(b - md/2) . \tag{5.1}$$

Before evaluating numerically, the physical limit $d \to 4$ must be taken. For diagrams which contain UV or IR divergences, this is not a simple task. These divergences manifest as zeroes in the U and V functions respectively - naively setting $d \to 4$ results in divergent integrals.

As a simple example, consider the two dimensional integral $I = \int_0^1 dx \int_0^1 dy \, (x+y)^{-2+\epsilon}$. This can be easily evaluated for positive ϵ as $I = \frac{2^\epsilon - 2}{\epsilon(\epsilon-1)}$, which has an ϵ^{-1} pole as ϵ approaches zero. However, this pole can be overlooked by attempting to take the $\epsilon \to 0$ limit before integrating, resulting in the divergent integral $\int_0^1 dx \int_0^1 dy \, (x+y)^{-2}$. Evidently the divergences must be extracted analytically before the result can be numerically integrated. This process is described in Ref [42].

To decide whether a graph contains divergences, one can examine the amplitude in momentum space or in parametric space. In parametric space, the analysis is straightforward: we set $d = 4$ everywhere then check if the resulting integral is finite. As we will discuss in more detail later, divergences only occur when subsets of Feynman parameters become small. For a subset containing s Feynman parameters x_i, the integral of $f(x_i)$ in a region where $x_i \sim \epsilon$ can be approximated as $f(\epsilon)\epsilon^s$. For convergent integrals, this quantity must vanish in the limit $\epsilon \to 0$, otherwise the integral
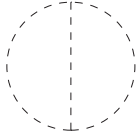
Figure 5.1: Scalar vacuum bubble diagram

diverges.

As a concrete example, consider the bubble diagram in Fig 5.1 which arises in a scalar field theory with a ϕ^3 coupling. The amplitude is given, in our formalism, by:

$$\mathcal{M} = i\frac{g^2 M^2}{(4\pi)^d}\left(\frac{M^2}{\mu^2}\right)^{d-4}\int\!\!\!\int\!\!\!\int_0^1 dx_1 dx_2 dx_3 \delta(1-x_1-x_2-x_3)(x_1x_2+x_1x_3+x_2x_3)^{-d/2}\Gamma(3-d)\,. \quad (5.2)$$

Ignoring the overall divergence from the gamma function, we find additional logarithmic subdivergences associated with the sets (x_1x_2), (x_1x_3) and (x_2x_3) approaching zero. For instance, with $d=4$ and $x_1, x_2 \to \epsilon$, we get an ϵ^2 from the measure which cancels with an ϵ^{-2} from the integrand. This implies that the integral will be logarithmically divergent as x_1 and x_2 approach zero. Setting $d=4$ was a mistake and additional processing is necessary before this integral can be evaluated numerically.

We apply this analysis to the diagrams which contribute to $a_\mu^{\pi^+\pi^-}$ and find that they are all finite. As mentioned previously, this depends crucially on using the Ward identity to rewrite the LBL amplitude (Eq (4.16)). Without it, individual diagrams are divergent, making the calculation far more difficult. In our case, however, analysis of the numerators generated by each diagram suggest that we can safely take the $d \to 4$ limit before integrating. The various contributions can then all be placed into one integral:

$$a_\mu = \frac{1}{32}\left(\frac{\alpha}{\pi}\right)^3\int\!\!\!\int\!\!\!\int_0^1 dx_1 dx_2 \ldots \delta(1-\Sigma x_i)\frac{1}{U^5}\sum \text{num}_i\text{F}_i(V)\,, \quad (5.3)$$

where $\text{F}_i(V)$ depends on the graph and particular choice of VMD prescription. From Eqs. (4.39) and (4.46), we see that $\text{F}_i(V)$ will either be a sum of $\log(V)$, V^{-1}, or V^{-2} terms. We have also absorbed factors of U into the num_i terms.

5.2 Monte Carlo integration

The integral in Eq.(5.3) contains eight Feynman parameters and therefore, upon eliminating the delta function, is a seven dimensional integral. Multi-dimensional integrals such as this one can often be simply and quickly evaluated numerically using Monte Carlo (MC) integration. The basic

idea is that to calculate the integral $I = \int_a^b dx \, f(x)$, one can randomly generate a set of N points x_i using a uniform distribution between a and b. The integral is then estimated as:

$$I \sim (b-a)\frac{\sum f(x_i)}{N} = (b-a)\langle f \rangle \,. \tag{5.4}$$

As $N \to \infty$ the relationship becomes exact; for finite N, the variance of the integrand evaluations $f(x_i)$ provides a good estimate of the error:

$$\sigma_I = \sqrt{\frac{(b-a)^2}{N^2}\sum_i \sigma_f^2} = \frac{b-a}{\sqrt{N}}\sigma_f \,, \tag{5.5}$$

where $\sigma_f^2 = \langle f^2 \rangle - \langle f \rangle^2$ for large values of N. The generalization to multidimensional integrals is simple - in the formulas above, $b-a$ is replaced by V, the volume of the region.

This basic method can be improved upon by algorithms which essentially assign more points in regions with larger variances. For our calculation, we have chosen to implement the MISER algorithm. This is a recursive technique which calculates the integral and error estimates for a given region. If the error is larger than the goal error, the region is bisected and the process is repeated for the two subregions. This continues until the goal error is met in all regions.

In more detail, N random integrand evaluations are allotted for a given region. A fraction of these (in our case 10%) are calculated, and the integrand variance is estimated using these points. Eq. (5.5) predicts the total integral error which will be obtained using the full N points. If this is acceptable, the remaining evaluations are taken and the integral value and error estimate are returned. If not, the region is bisected along one of the dimensions. The preliminary data set will contain roughly the same number of points in each subregion; these are used to calculate the variances σ_1 and σ_2 for the two subregions. With N total points to distribute throughout both regions, the overall error is minimized by allotting $N_1 = N\sigma_1/(\sigma_1 + \sigma_2)$ and $N_2 = N\sigma_2/(\sigma_1 + \sigma_2)$. As expected, regions with higher variance receive more points. With this partitioning, the total error can again be estimated by combining errors from each subregion. Each dimension is bisected in this way, and the bisection which produces the smallest total error is chosen. Again, if this error is less than the goal error, the remaining evaluations are taken (but now partitioned accordingly) and the results are returned. Otherwise, the entire process is repeated for the two subregions, but now with an error goal reduced by $\sqrt{2}$ to account for the splitting. Since the integral error is proportional to the volume which is reduced by a factor of two for every bisection, it is clear that the goal error will eventually be obtained for all regions.

5.3 Difficult features of parametric integrals

The MISER algorithm described in the previous section can be found in standard numeric integration packages such as CUBA [43]. However, parametric integrals like Eq (5.1) share a number of features which make general purpose integrators slow and inefficient. Most importantly, the integrand divergences which appear in regions where U or V go to zero can result in unreliable error estimates and values for the integral, which, though convergent, require vast numbers of points with convergence slower than $N^{-1/2}$. We discuss this problem in more detail in Section 5.5.

Parametric integrals also have to eliminate the delta function before numerically integrating. This leaves integration limits which are functions of the remaining Feynman parameters. MC integration requires fixed limits, therefore a variable redefinition is required. The simplest one involves rescaling each Feynman parameter as in the example below:

$$\iiint\limits_{0}^{1} dx_1 dx_2 dx_3 dx_4 \delta(1 - x_1 - x_2 - x_3 - x_4) f(x_1, x_2, x_3, x_4) =$$

$$\int_0^1 dx_1 \int_0^{1-x_1} dx_2 \int_0^{1-x_1-x_2} dx_3 \, f(x_1, x_2, x_3, 1 - x_1 - x_2 - x_3) =$$

$$\iiint\limits_{0}^{1} dy_1 dy_2 dy_3 \, (1 - y_1)^2 (1 - y_2) f(y_1, (1 - y_1)y_2, (1 - y_1)(1 - y_2)y_3, (1 - y_1)(1 - y_2)(1 - y_3)) .$$

$$(5.6)$$

Because this integral will be randomly sampled in y-space, we see that the distribution won't be uniform in the original Feynman parameters. Obviously this is accounted for by the Jacobian, but if, for example, the integral is dominated by the region where x_4 is close to one, then many points will need to be sampled in y-space before adequately covering this region. This problem only becomes worse as the number of Feynman parameters is increased. To address thise issues, we decided to create our own integrator to evaluate the parametric integral in Eq. (5.3). Our solutions to the problems presented here are given in the next few sections. They allow us to achieve a typical accuracy of $\mathcal{O}(10^{-3})$ in less than 1 minute run time using a standard laptop.

5.4 Generating random numbers with a fixed sum

Rather than redefining variables as in Eq. (5.6), we seek a distribution which is uniform in the space of the original Feynman parameters. This is equivalent to generating points which are uniformly spread over the surface $\sum_{i=1}^{n} x_i = 1$. We use geometrical arguments to find the correct distribution for the first few cases, then generalize to any n.

For $n = 2$, we seek a distribution of points which is uniformly distributed along the line $x_1 + x_2 =$
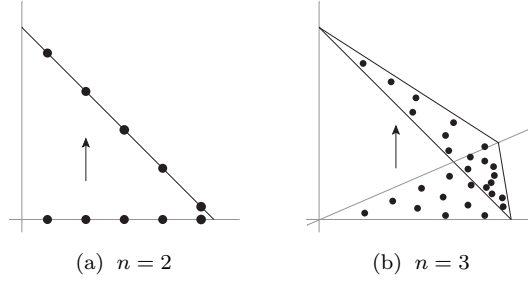
(a) $n = 2$ (b) $n = 3$

Figure 5.2: A uniform distribution of points on the surfaces shown can be generated by first picking points uniformly on the surfaces below, then projecting onto the surface

1. It is clear from Fig 5.2(a) that this can be obtained by first choosing x_1 from a uniform distribution then lifting the result up to find x_2.

Similarly, for $n = 3$, points distributed uniformly throughout the triangular region in the $x_1 - x_2$ plane will give a uniform distribution on the surface $x_1 + x_2 + x_3 = 1$. x_1 and x_2 can be generated by considering their sum $x_1 + x_2 = r$, where $0 \leq r \leq 1$. For fixed r, x_1 and x_2 can be chosen as before, by picking x_1 randomly between 0 and r. The probability distribution for r is not flat, however, from the geometry of Fig 5.2(b) it should be clear that $P(r) \sim r$. Requiring r to be between 0 and 1 gives $P(r) = 2r$. This can be generated from the uniformly distributed variable y as $r = \sqrt{y}$. To summarize, the $n = 3$ case is handled by generating two random numbers y_1 and y_2 between 0 and 1 using a uniform distribution and then assigning:

$$
\begin{aligned}
x_1 &= r_2 r_1 \\
x_2 &= r_2 (1 - r_1) \\
x_3 &= 1 - r_2
\end{aligned}
\qquad , \qquad
\begin{aligned}
r_2 &= \sqrt{y_2} \\
r_1 &= y_1
\end{aligned}
\qquad . \tag{5.7}
$$

Generalizing is not too difficult, as each case builds on the previous ones. For $n = 4$, we first consider the sum $x_1 + x_2 + x_3 = r_3$ with $P(r_3) = 3r_3^2$. r_3 can be generated using $y^{1/3}$, and with r_3 fixed, this devolves to a rescaled $n = 3$ case, where now $x_1 + x_2 = r_3 r_2$. The correct prescripton for $n = 4$ is given by:

$$
\begin{aligned}
x_1 &= r_3 r_2 r_1 \\
x_2 &= r_3 r_2 (1 - r_1) \\
x_3 &= r_3 (1 - r_2) \\
x_4 &= (1 - r_3)
\end{aligned}
\qquad , \qquad
r_i = (y_i)^{1/i}
\qquad . \tag{5.8}
$$

The generalization to n Feynman parameters should now be clear, and can be succinctly represented

by the formulas:

$$\sum_{i=1}^{m} x_i = \prod_{i=0}^{n-m} r_{n-i} \,,$$

$$r_i = (y_i)^{1/i} \,,$$

$$y_n = 1 \,, \tag{5.9}$$

where $y_1 - y_{n-1}$ are chosen randomly using a uniform distribution from 0 to 1. The probability distribution for each x_i is identical, depending only on n:

$$P(x) = (n-1)(1-x)^{n-2} \,. \tag{5.10}$$

For general $f(x_i)$, MC integration using this democratic distribution should converge faster than the equivalent hypercube-transformed version in Eq (5.6). To numerically integrate, we must know the volume of the region enclosed. In the Feynman parameter space, this is easily found by setting $f(x_i) = 1$:

$$V_n = \int\!\!\!\int\!\!\!\int_0^1 dx_1 dx_2 \ldots \delta(1 - \mathbf{\Sigma} x_i) = \frac{1}{(n-1)!} \,. \tag{5.11}$$

It is instructive to write this volume integral in terms of the other variables which we have created:

$$V_n = \int\!\!\!\int\!\!\!\int_0^1 dx_1 dx_2 \ldots \delta(1 - \mathbf{\Sigma} x_i) \,,$$

$$= \int\!\!\!\int\!\!\!\int_0^1 dr_{n-1} dr_{n-2} \ldots dr_1 (r_{n-1})^{n-2} (r_{n-2})^{n-3} \ldots r_2 \,,$$

$$= \int\!\!\!\int\!\!\!\int_0^1 dy_{n-1} dy_{n-2} \ldots dy_1 \frac{1}{(n-1)!} \,. \tag{5.12}$$

The last equation involves integration over a hypercube, but now with overall volume factor $1/(n-1)!$ instead of the more complicated Jacobian of Eq. (5.6). By using the variable transformations in Eq. (5.9), points can be uniformly distributed in both y and x space. In this form, the bisections used by the MISER algorithm can be easily created by halving the range of one of the randomly generated y's.

5.5   MC errors for singular integrands

The standard MC error estimation uses the variance:

$$\sigma_I^2 = \frac{V^2}{N}\left(\langle f^2\rangle - \langle f\rangle^2\right) . \tag{5.13}$$

This method only works for functions with well defined $\langle f\rangle$ and $\langle f^2\rangle$. Consider a MC integration of $f(x) = 1/\sqrt{x}$ from 0 to 1. The exact averages can be calculated explicitly: $\langle f\rangle = 2$, but $\langle f^2\rangle = \int_0^1 x^{-1}\,dx$ which diverges. As it involves a finite sum of random integrand evaluations, the calculated σ_I will obviously be finite, but its value will be unstable and does not converge as more points are included. More generally, for any function f where $\int f^2$ diverges, the variance σ_I is an unreliable estimate of the numeric integration error. The mean integral value still converges, but a different measure of error must be used such as $\delta_I \sim \langle |f - \langle f\rangle|\rangle$. However, these integrals tend to converge more slowly than their better behaved counterparts. Our initial attempts to integrate the singular integrand of Eq. (5.3) in this way showed no signs of convergence over timescales as long as 10 minutes.

Alternatively, one can often change variables in the singular region and tame the divergence. As a simple example, consider:

$$I = \int_0^1 dx \int_0^1 dy \frac{1}{(x+y)^{3/2}} . \tag{5.14}$$

Using the analysis from Section 5.1, near $x, y \to \epsilon$, the contribution to the integral scales as $\epsilon^{1/2}$, and I is therefore convergent. The squared integral $\int_0^1 dx \int_0^1 dy\, (x+y)^{-3}$, on the other hand, scales as ϵ^{-1} and therefore diverges. To numerically integrate, we split into two regions, one of which contains $x = y = 0$. The other is well-behaved and can be integrated in the usual manner. To integrate the singular region, we change variables: $x = r^2 t$, $y = (1-t)r^2$:

$$I = \iint \frac{2r^3 dr dt}{r^3} . \tag{5.15}$$

The Jacobian associated with the transformation cancels the singularity, and now the integral is easy to evaluate.

For all but the simplest of singularities, this method requires partitioning the integral into several regions, and making the appropriate variable changes, but the end result is usually worth the extra effort, converging much faster with reliable error estimate σ_I. In the next section, we discuss the singularity structure of our parametric integral and propose a series of variable changes to improve the behavior in the singular region.
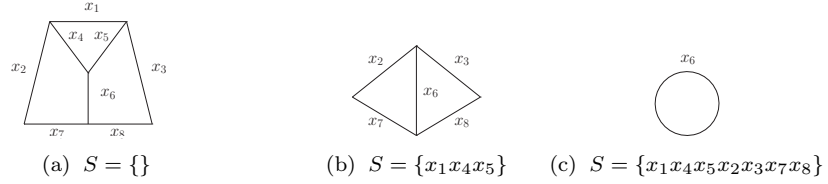
(a) $S = \{\}$ (b) $S = \{x_1 x_4 x_5\}$ (c) $S = \{x_1 x_4 x_5 x_2 x_3 x_7 x_8\}$

Figure 5.3: Diagrams for calculating $U_{G/S}$ in UV limit when parameters belonging to S approach zero

5.6   Singularities of parametric integrals

In general, both functions U and V can appear with a negative coefficient. The zeroes of these functions result in singular regions, which, for large enough coefficients can represent actual divergences. Although this does not happen in our case, it is clear that the zeroes must be in a direct correspondence with potential UV and IR divergences. Subdiagram UV divergences are contained in the function U, which vanishes whenever the subdiagram Feynamn parameters go to zero. This is evident for the loop subdiagrams parameterized in the matrix U - since each row contains only Feynman parameters from a given loop, the determinant will vanish as one of these sets approaches zero. The authors of Ref [42] show that this holds for any subdiagram, and that in fact, as the Feynman parameters of subdiagram S of graph G approach zero, U factorizes into the product:

$$U \to U_S U_{G/S}\,. \tag{5.16}$$

U_S is the determinant of the subdiagram only, and $U_{G/S}$ comes from the graph formed by shrinking subdiagram S to zero size in graph G. In this way, the singularity structure of U can be obtained graphically. We present a few examples using our graph and parameterization.

In the region where only x_1, x_4 and x_5 are small, U is approximately linear in these variables:

$$U \sim (x_1 + x_4 + x_5)U_b\,, \tag{5.17}$$

where U_b involves the other Feynman parameters and can be derived from the graph in Fig 5.3(b). If x_2, x_3, x_7 and x_8 are also allowed to be small, U is quadratic in the small variables:

$$U \sim \left[(x_1 + x_4 + x_5)(x_2 + x_3 + x_7 + x_8 + x_1) - x_1^2\right] U_c\,, \tag{5.18}$$

where U_c, derived from the graph in Fig 5.3(c), is equal to x_6. The prefactor is now more complicated, but its zeroes simply correspond to loops of subdiagram S: (145), (12378), and (237845). We can use this graphical method to determine the leading behavior of U in any region where a set of Feynamn parameters are small.

IR divergences are encoded in the function V. In our case, the analysis of the zeroes is simple. Because they contribute a $m_\pi^2 x_i$ to V, the Feynman parameters which correspond to massive pion propagators must vanish. The mass in the muon propagators cancels for p on shell, but reappears in V due to the loop-external momenta couplings. These are proportional to x_7 and x_8, therefore V vanishes as x_1, x_4, x_5, x_7^2, and x_8^2 go to zero. The zeroes in U are more numerous, but the nonlinear behavior of V is ultimately more challenging, as we will discuss in the next few sections. There we present a series of partitions and variable changes which give square integrable parametric integrals, allowing for a speedy and reliable MC calculation of $g_\mu - 2$.

5.7   Variable changes for U singularities

We begin by considering a stripped down version of our parametric integral:

$$I = \int\!\!\!\int\!\!\!\int_0^1 dx_1 dx_2 \ldots \delta(1 - \mathbf{\Sigma} x_i) U^{-2}\,. \tag{5.19}$$

From Fig 5.3(a), the smallest loop contains 3 Feynman parameters, therefore this integral is finite. However, it is not square integrable - as x_1, x_4, $x_5 \to \epsilon$, for example, the square integral scales as ϵ^{-1}. In this region, where only those three parameters are allowed to be small, we can change variables:

$$\int\!\!\!\int\!\!\!\int_0^1 dx_1 dx_4 dx_5 \delta(1 - \mathbf{\Sigma} x_i) =$$

$$\int_0^1 dr \int\!\!\!\int\!\!\!\int_0^1 dx_1 dx_4 dx_5 \delta(1 - r - x_2 - x_3 - x_6 - x_7 - x_8)\delta(r - x_1 - x_4 - x_5) =$$

$$\int_0^1 r^2 dr \int\!\!\!\int\!\!\!\int_0^1 d\overline{x}_1 d\overline{x}_4 d\overline{x}_5 \delta(1 - r - x_2 - x_3 - x_6 - x_7 - x_8)\delta(1 - \overline{x}_1 - \overline{x}_4 - \overline{x}_5)\,. \tag{5.20}$$

The behavior of U near the singular point is given by Eq. (5.17). The r^2 from the Jacobian now exactly cancels the r^{-2} which appears in U^{-2}. In these variables, both the integral and squared integral are convergent. Generating random sets of Feynman parameters is now slightly more complicated. Because of the two delta functions, we must apply our method of generating fixed sum random numbers twice, once with $n = 6$ and once with $n = 3$. This changes the volume from $1/7!$ to $1/5!\,2!$. If this was the only zero in U, we could use this form for the entire integral, but other zeroes exist. Indeed, the singularity structure becomes more complicated as more Feynman parameters approach zero.

We turn next to the region where x_1, x_4, x_5, x_2, x_6, x_7 are all allowed to be small. The overall

divergence is isolated by rescaling these parameters by r:

$$\delta(1 - \mathbf{\Sigma} x_i) \to r^5 \delta(1 - r - x_3 - x_8)\delta(1 - \overline{x}_1 - \overline{x}_4 - \overline{x}_5 - \overline{x}_2 - \overline{x}_6 - \overline{x}_7)\,. \tag{5.21}$$

Because it involves two loops, near $r = 0$, U^{-2} scales as r^{-4}. Again the singularity is removed by the Jacobian. In this form, though, the integrand still diverges when one of the sets $(\overline{x}_1\overline{x}_4\overline{x}_5)$, $(\overline{x}_2\overline{x}_4\overline{x}_6\overline{x}_7)$, and $(\overline{x}_1\overline{x}_2\overline{x}_5\overline{x}_6\overline{x}_7)$ go to zero. These correspond graphically to loops in the subdiagram. For our simple U^{-2} integral, the last set is not actually a problem since the square integral $\sim \epsilon^5/\epsilon^4$ and is finite. This will not be the case for our real integral, therefore we will treat it here as if it were divergent.

The solution, of course, is to make another transformation. Note that the $\overline{x}$ delta function does not allow for simultaneous divergences. We can therefore transform each set individually as it approaches zero. The diffferent regions must be carefully segregated; we accomplish this by appending step functions to the integrand. For this particular example, we are considering a region where x_3 and x_8 cannot simultaneously be zero (otherwise more singularities would be present than the ones discussed above). Therefore, the integral we wish to calculate is given by:

$$I_{1-3} = \iiint\limits_{0}^{1} dx_1 dx_2 \dots \delta(1 - \mathbf{\Sigma} x_i)U^{-2}\Theta(x_3 + x_8 > \delta)\,. \tag{5.22}$$

As suggested by the subscript, in order to make it square integrable, we split it into 3 pieces:

$$I_1 = \int_0^1 r_1^5 dr_1 \int_0^1 r_2^2 dr_2 \int_0^1 d\overline{\overline{x}}_1 \dots \int_0^1 d\overline{x}_2 \dots \int_0^1 dx_3 \dots$$
$$\delta(1 - r_1 - x_3 - x_8)\delta(1 - r_2 - \overline{x}_2 - \overline{x}_6 - \overline{x}_7)\delta(1 - \overline{\overline{x}}_1 - \overline{\overline{x}}_4 - \overline{\overline{x}}_5)U^{-2}$$
$$\Theta(x_3 + x_8 > \delta)\Theta(\overline{x}_1 + \overline{x}_5 + \overline{x}_2 + \overline{x}_6 + \overline{x}_7 > \delta)\Theta(\overline{x}_2 + \overline{x}_4 + \overline{x}_6 + \overline{x}_7 > \delta)\,, \tag{5.23}$$

$$I_2 = \int_0^1 r_1^5 dr_1 \int_0^\delta r_2^3 dr_2 \int_0^1 d\overline{\overline{x}}_2 \dots \int_0^1 d\overline{x}_1 \dots \int_0^1 dx_3 \dots$$
$$\delta(1 - r_1 - x_3 - x_8)\delta(1 - r_2 - \overline{x}_1 - \overline{x}_5)\delta(1 - \overline{\overline{x}}_2 - \overline{\overline{x}}_4 - \overline{\overline{x}}_6 - \overline{\overline{x}}_7)U^{-2}$$
$$\Theta(x_3 + x_8 > \delta)\Theta(\overline{x}_1 + \overline{x}_5 + \overline{x}_2 + \overline{x}_6 + \overline{x}_7 > \delta)\,, \tag{5.24}$$

$$I_3 = \int_0^1 r_1^5 dr_1 \int_0^\delta r_2^4 dr_2 \int_0^1 d\overline{\overline{x}}_1 \dots \int_0^1 d\overline{x}_4 \int_0^1 dx_3 \dots$$
$$\delta(1 - r_1 - x_3 - x_8)\delta(1 - r_2 - \overline{x}_4)\delta(1 - \overline{\overline{x}}_1 - \overline{\overline{x}}_5 - \overline{\overline{x}}_2 - \overline{\overline{x}}_6 - \overline{\overline{x}}_7)U^{-2}$$
$$\Theta(x_3 + x_8 > \delta)\,, \tag{5.25}$$

where $x_1 = r_1\bar{x}_1 = r_1 r_2 \bar{\bar{x}}_1$ etc. The delta functions are of the usual form, except for the ones involving r_2 in the last two integrals, which is only integrated from 0 to δ. This is put into the usual form by rescaling by $1 - r_2$:

$$\int_0^\delta dr_2 \delta(1 - r_2 - \bar{x}_1 - \bar{x}_5) = \int_0^\delta dr_2 (1 - r_2) \delta(1 - \hat{\bar{x}}_1 - \hat{\bar{x}}_5). \tag{5.26}$$

We represent this partitioning symbolically as:

$$I_{1-3} = (145267) \left. \frac{\overline{(145)}}{\frac{\overline{(2467)}}{\overline{(15267)}}} \right|_{x_3 + x_8 > \delta}. \tag{5.27}$$

To calculate the full integral, we must also include the region where $x_3 + x_8 < \delta$. The singularities are too numerous in this region, and we are forced to proceed in a piecewise manner. If we introduce the additional constraint $x_2 + x_7 < \delta$, this smaller region can be partitioned just like the last one:

$$I_{4-6} = (145368) \left. \frac{\overline{(145)}}{\frac{\overline{(3568)}}{\overline{(14368)}}} \right|_{\substack{x_3 + x_8 < \delta \\ x_2 + x_7 > \delta}}. \tag{5.28}$$

We continue this process, isolating two loop subdiagrams one-by-one:

$$I_{7-9} = (2345678) \left. \frac{\overline{(2467)}}{\frac{\overline{(3568)}}{\overline{(234578)}}} \right|_{\substack{x_3 + x_8 < \delta \\ x_2 + x_7 < \delta \\ x_1 > \delta/3}},$$

$$I_{10-12} = (1235678) \left. \frac{\overline{(3568)}}{\frac{\overline{(15267)}}{\overline{(12378)}}} \right|_{\substack{x_3 + x_8 < \delta \\ x_2 + x_7 < \delta \\ x_1 < \delta/3 \\ x_4 > \delta/3}},$$

$$I_{13-15} = (1234678) \left. \frac{\overline{(2467)}}{\frac{\overline{(14368)}}{\overline{(12378)}}} \right|_{\substack{x_3 + x_8 < \delta \\ x_2 + x_7 < \delta \\ x_1, x_4 < \delta/3 \\ x_5 > \delta/3}}. \tag{5.29}$$

With an appropriately chosen δ, our last set of integrals can finally be done with no further restrictions. For $\delta < 1/3$, x_6 is now forced to be non-zero by the delta function, rather than an imposed constraint:

$$I_{16-18} = (1234578) \left. \frac{\overline{(145)}}{\frac{\overline{(12378)}}{\overline{(452378)}}} \right|_{\substack{x_3 + x_8 < \delta \\ x_2 + x_7 < \delta \\ x_1, x_4, x_5 < \delta/3}} \tag{5.30}$$

By partitioning the integral into regions associated with the graph subdiagrams, we have managed to control the singularities, producing square integrable contributions from each region. For the 3-loop graphs which contribute to $g_\mu - 2$, this results in 18 distinct integrals, but now standard MC techniques can be applied to each one.

5.8 Variable changes for V singularities

Finally we consider the full integral in Eq. (5.3). U^{-5} is more singular than our simple example, but the numerator also contains factors of Feynman parameters - enough to render the integral convergent. One might expect that by partitioning it as before, the squared integrals could also be made convergent. However, additional complications arise due to the presence of V. In regions where both U and V contain zeroes, the overall singularity is enhanced and our previous prescription fails.

We illustrate these issues with the following integral:

$$I = \int\limits_0^1\!\!\!\int\!\!\!\int dx_1 dx_2 \ldots \delta(1 - \mathbf{\Sigma} x_i) \frac{x_1 x_2 x_3^2 x_4}{U^4} \frac{1}{(x_1 + x_4 + x_5 + x_7^2 + x_8^2)} \, . \tag{5.31}$$

Here V has been replaced with a simpler function which shares the same singularity structure. Consider the first partitioning which groups the variables (145267) into common scale r. As r approaches zero, the integrand roughly scales as:

$$\sim \frac{r^3 r^5}{r^8} \frac{1}{(r + x_8^2)} \, . \tag{5.32}$$

For $r \to \epsilon$, $x_8 \to \sqrt{\epsilon}$, the squared integral scales as $\epsilon^{-1/2}$ and is therefore divergent. The extra singularity which appears in V has ruined the convergence of the squared integral. This problem also occurs when the variables (145) are grouped together. The integrand is proportional to:

$$\frac{r^4}{r^4} \frac{1}{(r + x_7^2 + x_8^2)} \, , \tag{5.33}$$

which, for $r \to \epsilon$, x_7, $x_8 \to \sqrt{\epsilon}$, results in a non-convergent square integral $\sim \epsilon^0$.

Unlike the UV singularities which appear in U, these additional V singularities are not generic, depending both on the numerator and the form of V. Many diagrams in this calculation produce numerators which contain enough Feynman parameters to cancel the V singularity. However, not all do. We suspect that a completely general formalism for producing square integrable regions may not exist, and instead, due to V, must be considered on a case by case basis.

For our $g_\mu - 2$ integral, the two examples given happen to represent the most singular behavior. Fortunately, these extra divergences can be tamed through a slight modification of our previous prescription. For the first case, instead of defining $r = x_1 + x_4 + x_2 + x_6 + x_7$, we choose $r^3 = x_1 + x_4 + x_5 + x_2 + x_6 + x_7$. After changing variables, the integrand now behaves as:

$$\sim \frac{r^9 r^{17}}{r^{24}} \frac{1}{(r^3 + x_8^2)} \, , \tag{5.34}$$

which results in a convergent square integral scaling as $\epsilon^{1/6}$. Similarly, by grouping x_1, x_4, x_5 as $r^2 = x_1 + x_4 + x_5$, this too, can be made square integrable.

5.9 Final prescription for $g - 2$ integrals

In the end, the LBL $g - 2$ contributions of Eq. (5.3) can be made square integrable by the following partitioning:

$$I_{1-3} = (145267)_3 \frac{\overline{(145)}_2}{\overline{(2467)}}\bigg|_{x_3+x_8>\delta},$$

$$I_{4-6} = (145368)_3 \frac{\overline{(145)}_2}{\overline{(3568)}}\bigg|_{\substack{x_3+x_8<\delta \\ x_2+x_7>\delta}},$$

$$I_{7-9} = (2345678) \frac{\overline{(2467)}}{\overline{(3568)}}\bigg|_{\substack{x_3+x_8<\delta \\ x_2+x_7<\delta \\ x_1>\delta/3}},$$

$$I_{10-12} = (1235678)\frac{\overline{(3568)}}{\overline{(12378)}}\bigg|_{\substack{x_3+x_8<\delta \\ x_2+x_7<\delta \\ x_1<\delta/3 \\ x_4>\delta/3}},$$

$$I_{13-15} = (1234678)\frac{\overline{(2467)}}{\overline{(12378)}}\bigg|_{\substack{x_3+x_8<\delta \\ x_2+x_7<\delta \\ x_1,x_4<\delta/3 \\ x_5>\delta/3}},$$

$$I_{16-18} = (1234578) \frac{\overline{(145)}_2}{\overline{(452378)}}\bigg|_{\substack{x_3+x_8<\delta \\ x_2+x_7<\delta \\ x_1,x_4,x_5<\delta/3}}. \tag{5.35}$$

Here $(123)_m$ represents the grouping $r^m = x_1 + x_2 + x_3$, with default value $m = 1$. All delta functions which appear are manipulated into the usual form of 1 minus a sum of integration variables with range 0 to 1. In particular, for $m \neq 1$, this means rescaling by $(1 - r^m)$. The final result can be integrated using the MC techniques previously described. We now have a mix of integration variables - some appear inside delta functions and are generated according to our general formula, others have been factored out of the delta function and are generated using a uniform distribution.

Despite the extra complications introduced by V, we have ultimately managed to partition our result into square integrable regions. We have done this along lines suggested by the UV singularities contained in U. This partitioning is general and can be used for any diagram (although the number of partitions does increase rapidly with the number of loops). Depending on the numerator, V, and its coefficient, this may not be enough to create a square integrable result, but often, as in our case, the variable changes can be tweaked to account for the additional singularities. The end result is a set of parametric integrals which can be numerically evaluated quickly and stably with reliable estimates for their value and error.

Chapter 6

Results

We begin by reproducing the results of previous calculations. For the various mass scales, we use the PDG values:

$$m_\pi = m_{\pi^\pm} = 139.57018 \text{ MeV}, \tag{6.1}$$

$$m_\mu = 105.6583715 \text{ MeV}, \tag{6.2}$$

$$M_V = m_\rho = 775.49 \text{ MeV}, \tag{6.3}$$

and later, for the a_1 models, we set the axial vector mass $M_A = \sqrt{2}M_V$.

The LO and ρ-corrected results for the diagrams of Fig 4.3 are shown in Table 6.1. Here HLS refers to the partial VMD prescription of Eq (3.13) and (3.14), while VMD corresponds to the form factors of Eq (3.13) and (3.31) (leaving out the a_1 contribution). The quoted errors refer only to the uncertainty due to the numeric integration. The values we obtain agree with the previous calculations discussed in Section 1.2.

Table 6.1: Charged pion contribution to a_μ for two different models of ρ exchange

	LO	HLS	VMD
$a_\mu^{\pi^+\pi^-} \times 10^{10}$	$-4.385(3)$	$-.434(2)$	$-1.644(2)$

The HLS and VMD results incorporate both LO and ρ exchange diagrams. To these, we must add the a_1 contribution from Model I or Model II. As previously noted, the a_1 exchange diagrams in Figs 4.6 and 4.7 contain $\gamma\pi\pi$ and $\gamma\gamma\pi\pi$ vertices which will be modified by ρ exchange. Therefore, for each a_1 model, we present three different results, one with LO photon-pion vertices, one with HLS corrections, and one with VMD corrections. Of course, only one of these will be appropriate for each model; we include the other values in an attempt to compare the two and gauge the model dependence of the a_1 contribution. These results are shown below:

Unlike Model I, our second model does not enhance the convergence of the pion loop integral, and as a result, some of the graphs in Fig 4.7 must be paired to produce a finite result. This pairing

Table 6.2: a_1 exchange contribution to $a_\mu^{\pi^+\pi^-}$ ($\times 10^{10}$)

	LO	HLS	VMD
Model I	$-7.069(3)$	$-1.345(3)$	$-5.473(3)$
Model II	$-6.349(3)$	$-$	$-3.248(2)$

is maintained by the LO and VMD prescriptions, but is broken by HLS, leading to a divergent result. We discard this and consider only the finite predictions from each model.

For both models we find a relatively large LO a_1 contribution. This gets supressed by the inclusion of the VMD form factors, in accord with the similar effects demonstrated in Table 6.1. However, we see that for both models, the a_1 contribution opposes the ρ contribution, pushing the overall magnetic moment toward larger values. Furthermore, Table 6.2 shows a general agreement between the two different models, suggesting, perhaps, a relative model independence in the a_1 contribution, at least compared to the larger differences between HLS and VMD. Finally, we combine the appropriate a_1 value with its counterpart from Table 6.1 to find the full charged pion loop contribution, $a_\mu^{\pi^+\pi^-}$:

$$a_\mu^{\mathrm{I,\,HLS}} = -1.779(4) \times 10^{-10} \,, \tag{6.4}$$

$$a_\mu^{\mathrm{II,\,VMD}} = -4.892(3) \times 10^{-10} \,. \tag{6.5}$$

Chapter 7

Conclusion

The theoretical estimation of the hadronic light-by-light contribution to a_μ is, at least at present, unavoidably model dependent. In situations like this, it is only in the concurrence between the results of various valid models that some degree of certainty can be found. Through much effort, this has been achieved for the pseudoscalar exchange contribution. The same can not be said for the less studied charged pion loop contribution, for which only a few results exist. In this thesis, we have re-examined those results, focusing on the models used in the calculation of $a_\mu^{\pi^+\pi^-}$.

We began with a consistency check at low energies, calculating the charged pion contribution to light-by-light scattering to two loops in χPT. Matching our results onto a four photon effective Lagrangian, we found that the NLO corrections were dominated by the pion charge radius and the pion polarizability. The two occurred with roughly the same magnitude, but because of a numerical supression at LO, these provided $\mathcal{O}(10\%)$ corrections to the LBL amplitude, rather than the expected 1%. More significantly, we found that in this low energy regime, the existing models capture only the charge radius corrections, missing out on potentially significant polarizability corrections.

Next, we considered alternative models which give the correct pion form factors at low energies, reproducing both the charge radius and polarizability corrections through exchange of the ρ and a_1 mesons. The a_1 form factors are poorly behaved at high energies, however, leading to divergences when inserted into the LBL and a_μ calculations. Abandoning these models, we decided on the simpler approach of modifying the necessary χPT counterterms to give appropriate form factors. We then developed two a_1 models with improved UV behavior, which, when paired with the correct model of ρ exchange, satisfy all the known constraints from χPT and QCD.

Finally, we come to the main result of this thesis - the magnetic moment. In the previous calculations of $a_\mu^{\pi^+\pi^-}$, inclusion of the ρ VMD form factors strongly modified the LO result, and therefore it seemed reasonable to suspect that including a_1 contributions in the form factors could also have a large impact. After a lengthy calculation, we have found that this is indeed the case. In

the absence of a_1 contributions, we reproduce the old results

$$a_\mu^{\mathrm{HLS}} = -.434(2) \times 10^{-10}\,, \tag{7.1}$$

$$a_\mu^{\mathrm{VMD}} = -1.644(2) \times 10^{-10}\,, \tag{7.2}$$

for two different models of ρ exchange. However, when contributions from our two a_1 models are included, these values shift dramatically:

$$a_\mu^{\mathrm{I,\,HLS}} = -1.779(4) \times 10^{-10}\,, \tag{7.3}$$

$$a_\mu^{\mathrm{II,\,VMD}} = -4.892(3) \times 10^{-10}\,. \tag{7.4}$$

Ours is the first full calculation of the charged pion loop contribution to a_μ which includes corrections from both ρ and a_1 exchanges. Spurred by [44], a recent attempt was made by Bijnens and Abyaneh to estimate the effect of including the a_1 exchanges[45]. By adding the pion polarizability interaction from Eq (3.15), along with an energy cutoff of 500 MeV, they found an enhancement to $a_\mu^{\pi^+\pi^-}$ of 10%. However, this result has a strong dependence on the energy cutoff as the full contribution is divergent. We avoid this issue with our form factor approach by selecting models with improved UV behavior. In addition, unlike those used in previous calculations, our models are the first which give the proper $1/q^2$ behavior for the $\gamma\gamma\pi\pi$ vertex. Admittedly, it is unclear how important this behavior is in the magnetic moment calculation. Presumably heavier resonances could be added which have marginal impact on $g-2$, but alter the higher energy behavior of the form factors. If the QCD constraint is dismissed, then our Model I could also be paired with the full VMD ρ prescription, giving:

$$a_\mu^{\mathrm{I,\,VMD}} = -7.117(4) \times 10^{-10}\,. \tag{7.5}$$

From this work it is clear that inclusion of the a_1 in the pion loop calculation can have a large effect on $a_\mu^{\pi^+\pi^-}$. For the two models presented here, we have found that the contributions from the a_1 tend to oppose those from the ρ, resulting in a larger $a_\mu^{\pi^+\pi^-}$; a_μ^{LO} may be lesss supressed than previously believed. Along with the increase in size comes an increase in modeling uncertainty. Although our two models of a_1 exchange were quite different, we found decent agreement in Table 6.2. However, the differences between the HLS and VMD prescriptions, already present without the a_1, become magnified with it. Although they satisfy all known constraints, our HLS model and our VMD model produce a_μ contributions which differ by more than 3×10^{-10}. If the result from Eq (7.5) is included, the discrepancy is even larger.

These results lead us to believe that the charged pion loop contribution to a_μ is far from settled, and that the current uncertainty may be underestimated. In addition, we have found that including

the a_1 tends to push a_μ to more negative values, thereby increasing the discrepancy between theory and experiment. Further work will be necessary to resolve these issues.

Chapter 8

Appendix

8.1   LBL Feynman integrals

The four Feynman integrals needed for the LBL amplitude are presented below. For convenience, we use a modified Gamma function defined as: $\Gamma(n) \equiv \frac{1}{(4\pi)^{d/2}} \mu^{4-d} \Gamma(n - d/2)$.

$$
\begin{aligned}
H^{\mu\nu\sigma\rho}(k_1, k_2, k_3, k_4) &\equiv \int_0^1 dx \int_0^{1-x} dy \int_0^{1-x-y} dz \bigg\{ 4 \left(g^{\mu\nu} g^{\sigma\rho} + g^{\mu\sigma} g^{\nu\rho} + g^{\mu\rho} g^{\nu\sigma} \right) \Gamma(2) \left(\tfrac{1}{D_1} \right)^{2-d/2} \\
&- 2 \left(g^{\mu\nu} C^\sigma D^\rho + g^{\mu\sigma} B^\nu D^\rho + g^{\mu\rho} B^\nu C^\sigma + g^{\nu\sigma} A^\mu D^\rho + g^{\nu\rho} A^\mu C^\sigma + g^{\sigma\rho} A^\mu B^\nu \right) \Gamma(3) \left(\tfrac{1}{D_1} \right)^{3-d/2} \\
&+ A^\mu B^\nu C^\sigma D^\rho \Gamma(4) \left(\tfrac{1}{D_1} \right)^{4-d/2} \bigg\},
\end{aligned}
$$

where

$$
\begin{aligned}
D_1 &= (x^2 - x)k_1^2 + (y^2 - y)k_2^2 + (z^2 - z)(k_2 + k_3)^2 - 2xy k_1 k_2 - 2xz k_1(k_2 + k_3) + 2yz k_2(k_2 + k_3) + m_\pi^2 \,, \\
A^\mu &= (2x - 1)k_1^\mu - 2(y + z)k_2^\mu - 2z k_3^\mu \,, \\
B^\nu &= 2x k_1^\nu + (1 - 2y - 2z)k_2^\nu - 2z k_3^\nu \,, \\
C^\sigma &= 2x k_1^\sigma + 2(1 - y - z)k_2^\sigma + (1 - 2z)k_3^\sigma \,, \\
D^\rho &= (2x - 1)k_1^\rho + (1 - 2y - 2z)k_2^\rho + (1 - 2z)k_3^\rho \,.
\end{aligned}
$$

$$
I^{\mu\nu}(k_1, k_2) \equiv \int_0^1 dx \int_0^{1-x} dy \bigg\{ - 2g^{\mu\nu} \Gamma(2) \left(\tfrac{1}{D_1} \right)^{2-d/2} + A^\mu B^\nu \Gamma(3) \left(\tfrac{1}{D_1} \right)^{3-d/2} \bigg\},
$$

where

$$D_1 = (x^2 - x)k_1^2 + (y^2 - y)k_2^2 - 2xyk_1k_2 + m_\pi^2 \,,$$

$$A^\mu = (2x - 1)k_1^\mu - 2yk_2^\mu \,,$$

$$B^\nu = 2xk_1^\nu + (1 - 2y)k_2^\nu \,.$$

$$J^{\mu\nu}(k_1) \equiv \int_0^1 dx \left\{ -2g^{\mu\nu}\Gamma(1)\left(\frac{1}{D_1}\right)^{1-d/2} + 2x(2x-1)k_1^\mu k_1^\nu \Gamma(2)\left(\frac{1}{D_1}\right)^{2-d/2} \right\} \,,$$

where

$$D_1 = (x^2 - x)k_1^2 + m_\pi^2 \,.$$

$$K(k_1, k_2) \equiv \int_0^1 dx \, \Gamma(2)\left(\frac{1}{D_1}\right)^{2-d/2} \,,$$

where

$$D_1 = (x^2 - x)(k_1 + k_2)^2 + m_\pi^2 \,.$$

8.2 Ward identity

Two amplitudes are needed to demonstrate the Ward identity in Eq (2.17). For the $\gamma\gamma\pi\pi$ vertex with incoming photon momenta k_1 and k_2, incoming pion momentum p_1, and outgoing pion momentum p_2, we have:

$$
\begin{aligned}
&\mathcal{M}^{\mu\nu}(k_1, k_2, p_1, p_2) = \\
&\frac{-ie^2}{(p_1^2 - m_\pi^2)(p_2^2 - m_\pi^2)}\left[2g^{\mu\nu}\left(1 - 2c_1 + \frac{c_2 m_\pi^2}{p_1^2 - m_\pi^2} + \frac{c_2 m_\pi^2}{p_2^2 - m_\pi^2}\right) + V_1^{\mu\nu}(k_1, k_2) + (p_1^2 + p_2^2 - 2m_\pi^2)V_2^{\mu\nu}\right] \\
&+ \frac{ie^2(2p_1^\alpha + k_1^\alpha)(2p_2^\beta - k_2^\beta)}{(p_1^2 - m_\pi^2)((p_1 + k_1)^2 - m_\pi^2)(p_2^2 - m_\pi^2)}\left[\delta_\alpha^\mu \delta_\beta^\nu \left(1 - 3c_1 + \frac{c_2 m_\pi^2}{p_1^2 - m_\pi^2} + \frac{c_2 m_\pi^2}{(p_1 + k_1)^2 - m_\pi^2} + \frac{c_2 m_\pi^2}{p_2^2 - m_\pi^2}\right)\right. \\
&\left. + V_\alpha{}^\mu(k_1)\delta_\beta^\nu + \delta_\alpha^\mu V_\beta{}^\nu(k_2)\right] \\
&+ \frac{ie^2(2p_2^\alpha - k_1^\alpha)(2p_1^\beta + k_2^\beta)}{(p_1^2 - m_\pi^2)((p_2 - k_1)^2 - m_\pi^2)(p_2^2 - m_\pi^2)}\left[\delta_\alpha^\mu \delta_\beta^\nu \left(1 - 3c_1 + \frac{c_2 m_\pi^2}{p_1^2 - m_\pi^2} + \frac{c_2 m_\pi^2}{(p_2 - k_1)^2 - m_\pi^2} + \frac{c_2 m_\pi^2}{p_2^2 - m_\pi^2}\right)\right. \\
&\left. + V_\alpha{}^\mu(k_1)\delta_\beta^\nu + \delta_\alpha^\mu V_\beta{}^\nu(k_2)\right] \,.
\end{aligned}
$$

For the $\gamma\pi\pi$ vertex, with incoming photon momentum k, incoming pion momentum p_1, and outgoing pion momentum p_2, we have:

$$\mathcal{M}^\mu(k, p_1, p_2) = \frac{-ie(p_1^\alpha + p_2^\alpha)}{(p_1^2 - m_\pi^2)(p_2^2 - m_\pi^2)}\left[\delta_\alpha^\mu\left(1 - 2c_1 + \frac{c_2 m_\pi^2}{p_1^2 - m_\pi^2} + \frac{c_2 m_\pi^2}{p_2^2 - m_\pi^2}\right) + V_\alpha{}^\mu(k)\right] \,.$$

The only non-trivial part in the proof of the Ward identity comes from the Feynman integrals found in the form factors. We have managed to show, using integration by parts, that $k_1^\mu I_{\mu\nu}(k_1, k_2) =$

$-k_1^\nu K(k_1, k_2)$ and $k_1^\mu J_\mu{}^\nu(k_1) = -2k_1^\nu \Gamma(1) \left(\frac{1}{m_\pi^2}\right)^{1-d/2}$. Using these two relationships, it is simple, although tedious, to show that the Ward identity does indeed hold.

8.3 LBL effective Lagrangian

In this section we construct a complete basis of gauge invariant four photon operators up to mass dimension 10. At low energies, these operators give the dominant contributions to the LBL scattering amplitude. Throughout, we ignore operators which may be constructed with Levi-Civita tensors, as these do not appear in our result.

Due to gauge invariance, the first four photon operators appear at mass dimension 8, coupling four field strength operators. There are two ways to contract indices:

$$G_1 = F_{\mu\nu} F^{\mu\nu} F_{\alpha\beta} F^{\alpha\beta} \,,$$
$$G_2 = F_{\alpha\beta} F^{\beta\gamma} F_{\gamma\delta} F^{\delta\alpha} \,.$$

The next set of operators have mass dimension 10 and are constructed from four field strengths and two additional derivatives. Extracting a set of independent operators is challenging as many operators are related through integration by parts, as well as derivative swapping using the anti-symmetry of the field strengths. To ensure a complete set, we explicitly write down all possible operators, then list the relationships which allow us to eliminate redundant operators.

We begin with the operators where the additional derivatives are contracted into each other. These modify the G_1 and G_2 operators above:

$$F_1 = \partial^2 F_{\mu\nu} F^{\mu\nu} F_{\alpha\beta} F^{\alpha\beta} \,,$$
$$F_2 = \partial_\rho F_{\mu\nu} \partial^\rho F^{\mu\nu} F_{\alpha\beta} F^{\alpha\beta} \,,$$
$$F_3 = \partial_\rho F_{\mu\nu} F^{\mu\nu} \partial_\rho F_{\alpha\beta} F^{\alpha\beta} \,,$$
$$F_4 = \partial^2 F_{\alpha\beta} F^{\beta\gamma} F_{\gamma\delta} F^{\delta\alpha} \,,$$
$$F_5 = \partial_\rho F_{\alpha\beta} \partial^\rho F^{\beta\gamma} F_{\gamma\delta} F^{\delta\alpha} \,,$$
$$F_6 = \partial_\rho F_{\alpha\beta} F^{\beta\gamma} \partial^\rho F_{\gamma\delta} F^{\delta\alpha} \,.$$

Two of these operators can be eliminated using integration by parts:

$$\partial_\rho \left(\partial^\rho F_{\mu\nu} F^{\mu\nu} F_{\alpha\beta} F^{\alpha\beta} \right) = 0 \,,$$

$$F_1 + F_2 + 2F_3 = 0 \,,$$

$$\partial_\rho \left(\partial^\rho F_{\alpha\beta} F^{\beta\gamma} F_{\gamma\delta} F^{\delta\alpha} \right) = 0 \,,$$

$$F_4 + 2F_5 + F_6 = 0 \,.$$

We arbitrarily choose to eliminate F_1 and F_4, leaving four independent operators: F_2, F_3, F_5, F_6.

Next, we turn to the set of operators where the extra derivatives are contracted into different field strengths. Using derivative indices μ, ν, two field strength structures are possible: $F^{\mu\gamma} F^\nu{}_\gamma F_{\alpha\beta} F^{\alpha\beta}$, and $F^{\mu\alpha} F^{\nu\beta} F_{\alpha\gamma} F^\gamma{}_\beta$. Applying the derivatives to the first structure, we find:

$$F_7 = \partial_\mu \partial_\nu F^{\mu\gamma} F^\nu{}_\gamma F_{\alpha\beta} F^{\alpha\beta} \,,$$

$$F_8 = \partial_\mu F^{\mu\gamma} \partial_\nu F^\nu{}_\gamma F_{\alpha\beta} F^{\alpha\beta} \,,$$

$$F_9 = \partial_\nu F^{\mu\gamma} \partial_\mu F^\nu{}_\gamma F_{\alpha\beta} F^{\alpha\beta} \,,$$

$$F_{10} = F^{\mu\gamma} F^\nu{}_\gamma \partial_\mu \partial_\nu F_{\alpha\beta} F^{\alpha\beta} \,,$$

$$F_{11} = F^{\mu\gamma} F^\nu{}_\gamma \partial_\mu F_{\alpha\beta} \partial_\nu F^{\alpha\beta} \,,$$

$$F_{12} = \partial_\mu F^{\mu\gamma} F^\nu{}_\gamma \partial_\nu F_{\alpha\beta} F^{\alpha\beta} \,,$$

$$F_{13} = F^{\mu\gamma} \partial_\mu F^\nu{}_\gamma \partial_\nu F_{\alpha\beta} F^{\alpha\beta} \,.$$

As mentioned previously, we can use the antisymmetry of the field strength tensor to eliminate some of these operators:

$$F_7 = \partial_\mu \partial_\nu (\partial^\mu A^\gamma - \partial^\gamma A^\mu) F^\nu{}_\gamma F_{\alpha\beta} F^{\alpha\beta} \,,$$

$$= \partial^2 \partial_\nu A^\gamma F^\nu{}_\gamma F_{\alpha\beta} F^{\alpha\beta} \,,$$

$$= \tfrac{1}{2} F_1 \,.$$

Relationships like this exist whenever a derivative and one of the indices from the field strength on which it acts are contracted into another field strength. From the list above, we find the additional relationships:

$$F_9 = \tfrac{1}{2} F_2 \,,$$

$$F_{13} = \tfrac{1}{2} F_3 \,.$$

Accordingly, we choose to eliminate F_7, F_9 and F_{13} from the list of independent operators. Integra-

tion by parts allows for a further reduction:

$$\partial_\mu \left(\partial_\nu F^{\mu\gamma} F^\nu{}_\gamma F_{\alpha\beta} F^{\alpha\beta} \right) = 0 \,,$$

$$F_7 + F_9 + 2F_{13} = 0 \,,$$

$$\partial_\mu \left(F^{\mu\gamma} \partial_\nu F^\nu{}_\gamma F_{\alpha\beta} F^{\alpha\beta} \right) = 0 \,,$$

$$F_8 + F_7 + 2F_{12} = 0 \,,$$

$$\partial_\mu \left(F^{\mu\gamma} F^\nu{}_\gamma \partial_\nu F_{\alpha\beta} F^{\alpha\beta} \right) = 0 \,,$$

$$F_{12} + F_{13} + F_{10} + F_{11} = 0 \,.$$

The first equation is of no use, but the next two allow us to eliminate F_8 and F_{10}, leaving only two independent operators: F_{11} and F_{12}.

We continue with the second tensor structure:

$$F_{14} = \partial_\mu \partial_\nu F^{\mu\alpha} F^{\nu\beta} F_{\alpha\gamma} F^\gamma{}_\beta \,,$$

$$F_{15} = \partial_\mu F^{\mu\alpha} \partial_\nu F^{\nu\beta} F_{\alpha\gamma} F^\gamma{}_\beta \,,$$

$$F_{16} = \partial_\nu F^{\mu\alpha} \partial_\mu F^{\nu\beta} F_{\alpha\gamma} F^\gamma{}_\beta \,,$$

$$F_{17} = F^{\mu\alpha} F^{\nu\beta} \partial_\mu \partial_\nu F_{\alpha\gamma} F^\gamma{}_\beta \,,$$

$$F_{18} = F^{\mu\alpha} F^{\nu\beta} \partial_\mu F_{\alpha\gamma} \partial_\nu F^\gamma{}_\beta \,,$$

$$F_{19} = F^{\mu\alpha} F^{\nu\beta} \partial_\nu F_{\alpha\gamma} \partial_\mu F^\gamma{}_\beta \,,$$

$$F_{20} = \partial_\mu F^{\mu\alpha} F^{\nu\beta} \partial_\nu F_{\alpha\gamma} F^\gamma{}_\beta \,,$$

$$F_{21} = \partial_\mu F^{\mu\alpha} F^{\nu\beta} F_{\alpha\gamma} \partial_\nu F^\gamma{}_\beta \,,$$

$$F_{22} = F^{\mu\alpha} \partial_\mu F^{\nu\beta} \partial_\nu F_{\alpha\gamma} F^\gamma{}_\beta \,,$$

$$F_{23} = F^{\mu\alpha} \partial_\mu F^{\nu\beta} F_{\alpha\gamma} \partial_\nu F^\gamma{}_\beta \,.$$

Again, we use antisymmetry and integration by parts to reduce the list:

$$F_{17} = F^{\mu\alpha} F^{\nu\beta} \partial_\mu \partial_\nu \left(\partial_\alpha A_\gamma - \partial_\gamma A_\alpha \right) F^\gamma{}_\beta \,,$$

$$= -F^{\mu\alpha} F^{\nu\beta} \partial_\nu \partial_\gamma \left(\partial_\mu A_\alpha \right) F^\gamma{}_\beta \,,$$

$$= -\tfrac{1}{2} F_{10} \,,$$

$$F_{18} = -\tfrac{1}{2} F_{13} \,,$$

$$F_{21} = -\tfrac{1}{2} F_{12} \,,$$

$$F_{23} = -\tfrac{1}{2} F_{11} \,.$$

$$\partial_\mu \left(\partial_\nu F^{\mu\alpha} F^{\nu\beta} F_{\alpha\gamma} F^\gamma{}_\beta \right) = 0 \, ,$$

$$F_{14} + F_{16} + F_{22} + F_{23} = 0 \, ,$$

$$\partial_\mu \left(F^{\mu\alpha} \partial_\nu F^{\nu\beta} F_{\alpha\gamma} F^\gamma{}_\beta \right) = 0 \, ,$$

$$F_{15} + F_{14} + F_{20} + F_{21} = 0 \, ,$$

$$\partial_\mu \left(F^{\mu\alpha} F^{\nu\beta} \partial_\nu F_{\alpha\gamma} F^\gamma{}_\beta \right) = 0 \, ,$$

$$F_{20} + F_{22} + F_{17} + F_{19} = 0 \, ,$$

$$\partial_\mu \left(F^{\mu\alpha} F^{\nu\beta} F_{\alpha\gamma} \partial_\nu F^\gamma{}_\beta \right) = 0 \, ,$$

$$F_{21} + F_{23} + F_{18} + F_{17} = 0 \, .$$

We eliminate the redundant operators F_{17}, F_{18}, F_{21}, F_{23}, F_{14}, F_{15} and F_{20}, leaving three independent operators: F_{16}, F_{19} and F_{22}.

Finally we turn to the operators where both derivatives are contracted into the same field strength. These are highly constrained by the antisymmetry of the field strength, and only one operator is non-vanishing:

$$F_{24} = F^{\mu\nu} \partial_\mu F_{\alpha\beta} \partial_\nu F^{\beta\gamma} F_\gamma{}^\alpha \, .$$

This completes our exhaustive list of mass dimension 10 operators. We have found 24 distinct operators, from which 10 nominally independent ones have been chosen. However, closer study of these remaining operators uncovers three more subtle relationships:

$$F_{16} = \partial_\nu F^{\mu\alpha} \partial_\mu F^{\nu\beta} F_{\alpha\gamma} F^\gamma{}_\beta \, ,$$

$$= \partial_\nu F^{\mu\alpha} \left(\partial_\mu \partial^\nu A^\beta - \partial_\mu \partial^\beta A^\nu \right) F_{\alpha\gamma} F^\gamma{}_\beta \, ,$$

$$= \partial_\nu F^{\mu\alpha} \left(\partial_\nu F_\mu{}^\beta - \partial^\beta F_\mu{}^\nu \right) F_{\alpha\gamma} F^\gamma{}_\beta \, ,$$

$$= -\partial_\rho F_{\alpha\beta} \partial^\rho F^{\beta\gamma} F_{\gamma\delta} F^{\delta\alpha} - F^{\mu\alpha} \partial_\mu F^{\nu\beta} F_{\alpha\gamma} \partial_\nu F^\gamma{}_\beta \, ,$$

$$F_{16} = -F_5 - F_{23} \, .$$

$$F_{19} = F^{\mu\alpha} F^{\nu\beta} \partial_\nu F_{\alpha\gamma} \partial_\mu F^\gamma{}_\beta \, ,$$

$$= F^{\mu\alpha} F^{\nu\beta} \left(\partial_\nu \partial_\alpha A_\gamma - \partial_\nu \partial_\gamma A_\alpha \right) \partial_\mu F^\gamma{}_\beta \, ,$$

$$= F^{\mu\alpha} F^{\nu\beta} \left(\partial_\alpha F_{\nu\gamma} - \partial_\gamma F_{\nu\alpha} \right) \partial_\mu F^\gamma{}_\beta \, ,$$

$$= F^{\mu\nu} \partial_\mu F_{\alpha\beta} \partial_\nu F^{\beta\gamma} F_\gamma{}^\alpha + F^{\mu\alpha} \partial_\mu F^{\nu\beta} \partial_\nu F_{\alpha\gamma} F^\gamma{}_\beta \, ,$$

$$F_{19} = F_{24} + F_{22} \, .$$

$$F_{22} = F^{\mu\alpha}\partial_\mu F^{\nu\beta}\partial_\nu F_{\alpha\gamma}F^\gamma{}_\beta \,,$$

$$= F^{\mu\alpha}\left(\partial_\mu\partial^\nu A^\beta - \partial_\mu\partial^\beta A^\nu\right)\partial_\nu F_{\alpha\gamma}F^\gamma{}_\beta \,,$$

$$= F^{\mu\alpha}\left(\partial^\nu F_\mu{}^\beta - \partial^\beta F_\mu{}^\nu\right)\partial_\nu F_{\alpha\gamma}F^\gamma{}_\beta \,,$$

$$= -\partial_\rho F_{\alpha\beta}F^{\beta\gamma}\partial^\rho F_{\gamma\delta}F^{\delta\alpha} - F^{\mu\alpha}\partial_\mu F^{\nu\beta}\partial_\nu F_{\alpha\gamma}F^\gamma{}_\beta \,,$$

$$= -F_6 - F_{22} \,,$$

$$F_{22} = -\tfrac{1}{2}F_6 \,.$$

Eliminating these three operators leaves seven independent operators which form a complete basis for the mass dimension 10 operators:

$$F_2 = \partial_\rho F_{\mu\nu}\partial^\rho F^{\mu\nu}F_{\alpha\beta}F^{\alpha\beta} \,,$$

$$F_3 = \partial_\rho F_{\mu\nu}F^{\mu\nu}\partial_\rho F_{\alpha\beta}F^{\alpha\beta} \,,$$

$$F_5 = \partial_\rho F_{\alpha\beta}\partial^\rho F^{\beta\gamma}F_{\gamma\delta}F^{\delta\alpha} \,,$$

$$F_6 = \partial_\rho F_{\alpha\beta}F^{\beta\gamma}\partial^\rho F_{\gamma\delta}F^{\delta\alpha} \,,$$

$$F_{11} = F^{\mu\gamma}F^\nu{}_\gamma\partial_\mu F_{\alpha\beta}\partial_\nu F^{\alpha\beta} \,,$$

$$F_{12} = \partial_\mu F^{\mu\gamma}F^\nu{}_\gamma\partial_\nu F_{\alpha\beta}F^{\alpha\beta} \,,$$

$$F_{24} = F^{\mu\nu}\partial_\mu F_{\alpha\beta}\partial_\nu F^{\beta\gamma}F_\gamma{}^\alpha \,.$$

Clearly our particular choice of basis is not unique and different combinations of operators can be used. The equations listed in this section can be used to convert between the various other possible parameterizatons.

8.4 Removal of $\partial_\mu A^\mu$ terms

In this section, we show that gauge invariance permits us to remove $\partial_\mu A^\mu$ terms from a Lagrangian to leading order in α. We begin by considering the following Lagrangian:

$$\mathcal{L} = -\tfrac{1}{4}F_{\mu\nu}F^{\mu\nu} + e\partial_\mu A^\mu J + \ldots \tag{8.1}$$

Obviously to preserve gauge invariance, other interactions are necessary. These are signified by the ellipsis and are irrelevant to our purpose. We can remove the unwanted interaction by modifying the usual gauge fixing term:

$$-\tfrac{1}{2\xi}(\partial_\mu A^\mu)^2 \quad \rightarrow \quad -\tfrac{1}{2\xi}(\partial_\mu A^\mu + \xi eJ)^2. \tag{8.2}$$

This results in the gauge fixed Lagrangian:

$$\mathcal{L} = -\tfrac{1}{4}F_{\mu\nu}F^{\mu\nu} - \tfrac{1}{2\xi}(\partial_\mu A^\mu)^2 - \tfrac{\xi e^2}{2}J^2 + \ldots \tag{8.3}$$

The original $\partial_\mu A^\mu J$ term has been eliminated at the cost of a J^2 term. However, this interaction is suppressed by a factor of α and can be ignored in a leading order calculation such as a_μ^{HLBL}. The only caveat to this approach is that additional ghost interactions are introduced when using the gauge fixing term in Eq. (8.2). For most J, the same reasoning applies, and the new interactions are suppressed by a factor of α. Because A_μ transforms as $A_\mu \to A_\mu - \tfrac{1}{e}\partial_\mu\Lambda$, though, for a J such as $\partial^\mu(\pi^+\pi^- A_\mu)$, this can result in a ghost interaction term that is not suppressed by α. In our case, though, these complications do not arise, and we make use of this freedom for the pion form factors, dropping all terms proportional to k^μ and k_1^μ, k_2^ν respectively.

8.5 Feynman rules for the form factor a_1 model

We derive the relevant Feynman rules for the form factor interaction of Eq (3.19), reproduced below for convenience.

$$\begin{aligned}
\mathcal{L}_{a_1} &= -\frac{e^2}{4}F_{\mu\nu}\pi^+\left(\frac{1}{D^2 + M_A^2}\right)\left(F^{\mu\nu}\pi^-\right) \quad + \text{h.c.} \\
&= -\frac{e^2}{4M_A^2}F_{\mu\nu}\pi^+\sum_{n=0}^{\infty}\left(-\frac{D^2}{M_A^2}\right)^n\left(F^{\mu\nu}\pi^-\right) \quad + \text{h.c.}
\end{aligned} \tag{8.4}$$

In addition to the desired $\gamma\gamma\pi\pi$ coupling, we find that gauge invariance, through the covariant derivative, enforces an infinite series of photon-pion couplings. For the purposes of this LBL calculation, we need only consider interactions with four or fewer photons. The $\gamma\gamma\pi\pi$ vertex is trivial:

$$\mathcal{L}_{\gamma\gamma\pi\pi} = -\tfrac{e^2}{4}F_{\mu\nu}\pi^+\left(\tfrac{1}{\partial^2 + M_A^2}\right)\left(F^{\mu\nu}\pi^-\right) + \text{h.c.} \tag{8.5}$$

This results in the Feynman rule:

$$V^{\mu\nu} = \frac{-ie^2(k_1 k_2 g^{\mu\nu} - k_2^\mu k_1^\nu)}{(p_1 + k_1)^2 - M_A^2} + \text{photon perms}, \tag{8.6}$$

where p_1 is the incoming pion momentum, and the two photon momenta are chosen to be incoming as well.

For the $\gamma\gamma\gamma\pi\pi$ vertex, we use the series representation of Eq (8.4) and extract the terms linear

in A:

$$D^{2n} = D^2 D^{2(n-1)},$$

$$D^{2n}_{(1)} = \partial^2 D^{2(n-1)}_{(1)} - ie(\partial_\alpha A^\alpha + A^\alpha \partial_\alpha)\partial^{2(n-1)},$$

$$D^2_{(1)} = -ie(\partial_\alpha A^\alpha + A^\alpha \partial_\alpha),$$

$$D^{2n}_{(1)} = -ie \sum_{a=0}^{n-1} \partial^{2a}(\partial_\alpha A^\alpha + A^\alpha \partial_\alpha)\partial^{2(n-1-a)},\tag{8.7}$$

where the derivatives are understood to act on everything to the right. The three photon coupling can now be written as:

$$\mathcal{L}_{\gamma\gamma\gamma\pi\pi} = -\frac{e^2}{4M_A^2} F_{\mu\nu}\pi^+ \sum_{n=0}^{\infty}(-)^n \frac{D^{2n}_{(1)}}{M_A^{2n}}\left(F^{\mu\nu}\pi^-\right) \quad + \text{h.c.}$$

$$= \frac{ie^3}{4M_A^4} F_{\mu\nu}\pi^+ \sum_{n=0}^{\infty}\sum_{a=0}^{n-1}(-)^n \left(\frac{\partial^2}{M_A^2}\right)^a (\partial_\alpha A^\alpha + A^\alpha \partial_\alpha)\left(\frac{\partial^2}{M_A^2}\right)^{n-1-a}(F^{\mu\nu}\pi^-) + \text{h.c.}$$

$$= -\frac{ie^3}{4} F_{\mu\nu}\pi^+ \frac{1}{\partial^2+M_A^2}(\partial_\alpha A^\alpha + A^\alpha \partial_\alpha)\frac{1}{\partial^2+M_A^2}(F^{\mu\nu}\pi^-) + \text{h.c.}\tag{8.8}$$

The series resums nicely and the corresponding Feynman rule is given by:

$$V^{\mu\nu\sigma} = \frac{ie^3(k_1 k_2 g^{\mu\nu} - k_2^\mu k_1^\nu)(2p_1^\sigma + 2k_1^\sigma + k_3^\sigma)}{\left((p_1 + k_1)^2 - M_A^2\right)\left((p_1 + k_1 + k_3)^2 - M_A^2\right)} + \text{photon perms}.\tag{8.9}$$

Finally for the $\gamma\gamma\gamma\gamma\pi\pi$ vertex, we extract terms quadratic in A:

$$D^{2n} = D^2 D^{2(n-1)},$$

$$D^{2n}_{(2)} = \partial^2 D^{2(n-1)}_{(2)} - ie(\partial_\alpha A^\alpha + A^\alpha \partial_\alpha)D^{2(n-1)}_{(1)} - e^2 A^\alpha A_\alpha \partial^{2(n-1)},$$

$$D^2_{(2)} = -e^2 A^\alpha A_\alpha,$$

$$D^{2n}_{(2)} = -e^2 \sum_{a=0}^{n-1} \partial^{2a}(A^\alpha A_\alpha)\partial^{2(n-1-a)}$$

$$- e^2 \sum_{b=0}^{n-2} \partial^{2(n-2-b)}(\partial_\alpha A^\alpha + A^\alpha \partial_\alpha)\sum_{a=0}^{b} \partial^{2a}(\partial_\beta A^\beta + A^\beta \partial_\beta)\partial^{2(b-a)}.\tag{8.10}$$

We plug this result back into Eq (8.4):

$$\mathcal{L}_{\gamma\gamma\gamma\gamma\pi\pi} = -\frac{e^2}{4M_A^2} F_{\mu\nu}\pi^+ \sum_{n=0}^{\infty}(-)^n \frac{D^{2n}_{(2)}}{M_A^{2n}}\left(F^{\mu\nu}\pi^-\right) \quad + \text{h.c.}$$

$$= -\frac{e^4}{4} F_{\mu\nu}\pi^+ \frac{1}{\partial^2+M_A^2} A^\alpha A_\alpha \frac{1}{\partial^2+M_A^2}(F^{\mu\nu}\pi^-)$$

$$+ \frac{e^4}{4} F_{\mu\nu}\pi^+ \frac{1}{\partial^2+M_A^2}(\partial_\alpha A^\alpha + A^\alpha \partial_\alpha)\frac{1}{\partial^2+M_A^2}(\partial_\beta A^\beta + A^\beta \partial_\beta)\frac{1}{\partial^2+M_A^2}(F^{\mu\nu}\pi^-) + \text{h.c.}\tag{8.11}$$

Again, the series resums to give the Feynman rule:

$$
\begin{aligned}
V^{\mu\nu\sigma\rho} = {} & \frac{ie^4(k_1 k_2 g^{\mu\nu} - k_2^\mu k_1^\nu)g^{\sigma\rho}}{((p_1 + k_1)^2 - M_A^2)\,((p_1 + k_1 + k_3 + k_4)^2 - M_A^2)} \\
& - \frac{ie^4(k_1 k_2 g^{\mu\nu} - k_2^\mu k_1^\nu)(2p_1^\sigma + 2k_1^\sigma + k_3^\sigma)(2p_1^\rho + 2k_1^\rho + 2k_3^\rho + k_4^\rho)}{((p_1 + k_1)^2 - M_A^2)\,((p_1 + k_1 + k_3)^2 - M_A^2)\,((p_1 + k_1 + k_3 + k_4)^2 - M_A^2)} \\
& + \text{ photon perms}\,.
\end{aligned} \tag{8.12}
$$

Although there is no dynamical a_1 in this form factor approach, the denominator structure in our results above suggests the exchange of multiple a_1 mesons. We have found that a small set of Feynman rules for a ficticious a_1 can indeed reproduce the interactions above. These are given in Fig 3.3.

8.6 Example of magnetic moment calculation using the parametric formalism

The functions defined in Eq (4.31) are given here in terms of the Feynman parameters:

$$U = x_1x_2x_3 + x_1x_3x_4 + x_2x_3x_4 + x_1x_2x_5 + x_2x_3x_5 + x_1x_4x_5 + x_2x_4x_5 + x_3x_4x_5 + x_1x_2x_6+$$
$$x_1x_3x_6 + x_1x_4x_6 + x_2x_4x_6 + x_3x_4x_6 + x_1x_5x_6 + x_2x_5x_6 + x_3x_5x_6 + x_1x_3x_7 + x_3x_4x_7+$$
$$x_1x_5x_7 + x_3x_5x_7 + x_4x_5x_7 + x_1x_6x_7 + x_4x_6x_7 + x_5x_6x_7 + x_1x_2x_8 + x_1x_4x_8 + x_2x_4x_8+$$
$$x_2x_5x_8 + x_4x_5x_8 + x_1x_6x_8 + x_4x_6x_8 + x_5x_6x_8 + x_1x_7x_8 + x_4x_7x_8 + x_5x_7x_8 \,,$$

$$c_1 = x_2x_3 + x_3x_4 + x_2x_5 + x_4x_5 + x_2x_6 + x_3x_6 + x_4x_6 + x_5x_6 + x_3x_7 + x_5x_7 + x_6x_7 + x_2x_8+$$
$$x_4x_8 + x_6x_8 + x_7x_8 \,,$$

$$c_2 = x_1x_3 + x_3x_4 + x_1x_5 + x_3x_5 + x_4x_5 + x_1x_6 + x_4x_6 + x_5x_6 + x_1x_8 + x_4x_8 + x_5x_8 \,,$$

$$c_3 = x_1x_2 + x_1x_4 + x_2x_4 + x_2x_5 + x_4x_5 + x_1x_6 + x_4x_6 + x_5x_6 + x_1x_7 + x_4x_7 + x_5x_7 \,,$$

$$c_4 = x_3x_4 + x_4x_5 + x_4x_6 + x_5x_6 + x_4x_8 \,,$$

$$c_5 = -(x_2x_5 + x_4x_5 + x_4x_6 + x_5x_6 + x_5x_7) \,,$$

$$c_6 = -(x_4x_5 + x_1x_6 + x_4x_6 + x_5x_6) \,,$$

$$c_7 = -(x_3x_4x_7 + x_4x_5x_7 + x_4x_6x_7 + x_5x_6x_7 + x_2x_5x_8 + x_4x_5x_8 + x_4x_6x_8 + x_5x_6x_8 + x_4x_7x_8+$$
$$x_5x_7x_8)/U \,,$$

$$c_8 = -(x_1x_3x_7 + x_3x_4x_7 + x_1x_5x_7 + x_3x_5x_7 + x_4x_5x_7 + x_1x_6x_7 + x_4x_6x_7 + x_5x_6x_7 + x_4x_5x_8+$$
$$x_1x_6x_8 + x_4x_6x_8 + x_5x_6x_8 + x_1x_7x_8 + x_4x_7x_8 + x_5x_7x_8)/U \,,$$

$$c_9 = (x_4x_5x_7 + x_1x_6x_7 + x_4x_6x_7 + x_5x_6x_7 + x_1x_2x_8 + x_1x_4x_8 + x_2x_4x_8 + x_2x_5x_8 + x_4x_5x_8+$$
$$x_1x_6x_8 + x_4x_6x_8 + x_5x_6x_8 + x_1x_7x_8 + x_4x_7x_8 + x_5x_7x_8)/U \,,$$

$$c_{10} = (x_1x_3x_7^2 + x_3x_4x_7^2 + x_1x_5x_7^2 + x_3x_5x_7^2 + x_4x_5x_7^2 + x_1x_6x_7^2 + x_4x_6x_7^2 + x_5x_6x_7^2 + 2x_4x_5x_7x_8+$$
$$2x_1x_6x_7x_8 + 2x_4x_6x_7x_8 + 2x_5x_6x_7x_8 + x_1x_7^2x_8 + x_4x_7^2x_8 + x_5x_7^2x_8 + x_1x_2x_8^2 + x_1x_4x_8^2+$$
$$x_2x_4x_8^2 + x_2x_5x_8^2 + x_4x_5x_8^2 + x_1x_6x_8^2 + x_4x_6x_8^2 + x_5x_6x_8^2 + x_1x_7x_8^2 + x_4x_7x_8^2 + x_5x_7x_8^2)/U \,.$$

For diagram 4.3(a), its contribution to the magnetic moment is given in Eq (4.39) with the two numerator functions defined below:

$$\text{num}_7 = 2x_1\big(-2c_2c_5U - 2c_8c_2c_5U + 4c_4c_5U - 16c_7c_4c_5U + 6c_8c_4c_5U + 6c_8c_5^2U + 2c_4c_6U +$$

$$6c_7c_4c_6U - 6c_7c_5c_6U - 3c_7c_3c_4dU + 3c_7c_2c_5dU - c_8c_2c_5dU - 8c_7c_4c_5dU +$$

$$2c_7c_2c_3c_4x_5 + 2c_7c_3^2c_4x_5 + 2c_3c_4^2x_5 + 2c_2c_5^2x_5 + 2c_8c_2c_5^2x_5 + 2c_8c_3c_5^2x_5 -$$

$$2c_7c_2c_5c_6x_5 - 2c_7c_3c_5c_6x_5 - 4c_4c_5c_6x_5 + c_7c_2c_3c_4dx_5 + c_7c_3^2c_4dx_5 + c_8c_2c_5^2dx_5 +$$

$$c_8c_3c_5^2dx_5 - c_7c_2c_5c_6dx_5 - c_7c_3c_5c_6dx_5 + 4c_1^2(c_8c_3 - c_9c_6)(2+d)x_5 -$$

$$c_9c_4(6c_4U - c_2(2+d)(U - c_5x_5) + c_5(6U + c_3(2+d)x_5)) + c_1(-4c_6U - 2c_2c_3x_5 -$$

$$8c_7c_3c_4x_5 + 8c_7c_5c_6x_5 + 2c_6^2x_5 - 4c_7c_3c_4dx_5 + 4c_7c_5c_6dx_5 + c_9(-3c_2dU +$$

$$2c_4(2+d)(U + 2c_5x_5) + c_6(6U + (c_2+c_3)(2+d)x_5)) - c_8(6c_6U - 6c_5(2+d)U +$$

$$4c_5^2(2+d)x_5 + c_3(2(c_2+c_3)x_5 + d(-3U + (c_2+c_3)x_5))))\big),$$

$$\text{num}_8 = 4x_1\big(4c_7^3(c_3c_4 - c_5c_6)x_5 + (c_9c_4 - c_8c_5)((-2+c_9)c_9c_5x_5 - 2c_8(U - c_5x_5) + c_8^2(-U + c_5x_5)) +$$

$$2c_7^2(c_4((-2+3c_9)U + 4c_3x_5 - 2c_9c_5x_5) + c_5((2+c_8)U + 2(c_8c_5 - 2c_6)x_5)) +$$

$$c_1(c_8^3c_3x_5 - (-2+c_9)c_9^2c_6x_5 + c_8c_9((4-3c_9)U + ((-2+c_9)c_3 - 2c_6)x_5) +$$

$$c_8^2(3c_9U + 2c_3x_5 - c_9c_6x_5) + c_7^2(-4c_8c_3x_5 + 4c_9c_6x_5) - 4c_7(c_8((-1+2c_9)U + 2c_3x_5) +$$

$$c_9(U - 2c_6x_5))) + c_7(c_9^2(3c_4U - c_3c_4x_5 + c_5c_6x_5) + 2c_9(-c_5c_6x_5 +$$

$$c_4(U + c_3x_5 - 4c_5x_5)) + c_8(-(2+c_8)c_3c_4x_5 + 8c_5^2x_5 - (2+c_8)c_5(3U - c_6x_5))))\big).$$

Bibliography

[1] M. Passera, W. J. Marciano and A. Sirlin, Chin. Phys. C **34**, 735 (2010) [arXiv:1001.4528 [hep-ph]].

[2] F. Jegerlehner and A. Nyffeler, Phys. Rept. **477**, 1 (2009) [arXiv:0902.3360 [hep-ph]].

[3] B. L. Roberts, Chin. Phys. C **34**, 741 (2010) [arXiv:1001.2898 [hep-ex]].

[4] G. W. Bennett *et al.* [Muon G-2 Collaboration], Phys. Rev. D **73**, 072003 (2006) [hep-ex/0602035].

[5] G. W. Bennett *et al.* [Muon g-2 Collaboration], Phys. Rev. Lett. **92**, 161802 (2004) [hep-ex/0401008].

[6] G. W. Bennett *et al.* [Muon g-2 Collaboration], Phys. Rev. Lett. **89**, 101804 (2002) [Erratum-ibid. **89**, 129903 (2002)] [hep-ex/0208001].

[7] D. Stockinger, J. Phys. G G **34**, R45 (2007) [hep-ph/0609168].

[8] D. W. Hertzog, J. P. Miller, E. de Rafael, B. Lee Roberts and D. Stockinger, arXiv:0705.4617 [hep-ph].

[9] A. Czarnecki and W. J. Marciano, Phys. Rev. D **64**, 013014 (2001) [hep-ph/0102122].

[10] R. M. Carey, K. R. Lynch, J. P. Miller, B. L. Roberts, W. M. Morse, Y. K. Semertzides, V. P. Druzhinin and B. I. Khazin *et al.*, FERMILAB-PROPOSAL-0989.

[11] M. Fujikawa *et al.* [Belle Collaboration], Phys. Rev. D **78**, 072006 (2008) [arXiv:0805.3773 [hep-ex]].

[12] M. Benayoun, P. David, L. DelBuono, O. Leitner and H. B. O'Connell, Eur. Phys. J. C **55**, 199 (2008) [arXiv:0711.4482 [hep-ph]].

[13] F. Jegerlehner and R. Szafron, Eur. Phys. J. C **71**, 1632 (2011) [arXiv:1101.2872 [hep-ph]].

[14] J. Prades, E. de Rafael and A. Vainshtein, arXiv:0901.0306 [hep-ph].

[15] J. Bijnens, E. Pallante and J. Prades, Phys. Rev. Lett. **75**, 1447 (1995) [Erratum-ibid. **75**, 3781 (1995)]; Nucl. Phys. B **474**, 379 (1996); Nucl. Phys. B **626**, 410 (2002).

[16] M. Hayakawa, T. Kinoshita and A. I. Sanda, Phys. Rev. Lett. **75**, 790 (1995); Phys. Rev. D **54**, 3137 (1996).

[17] M. Hayakawa and T. Kinoshita, Phys. Rev. D **57**, 465 (1998) [Erratum-ibid. D **66**, 019902 (2002)] [arXiv:hep-ph/9708227].

[18] M. Knecht, A. Nyffeler, M. Perrottet and E. de Rafael, Phys. Rev. Lett. **88**, 071802 (2002) [arXiv:hep-ph/0111059].

[19] M. Knecht and A. Nyffeler, Phys. Rev. D **65**, 073034 (2002) [arXiv:hep-ph/0111058].

[20] K. Melnikov and A. Vainshtein, Phys. Rev. D **70**, 113006 (2004) [arXiv:hep-ph/0312226].

[21] J. Bijnens and J. Prades, Mod. Phys. Lett. A **22**, 767 (2007) [arXiv:hep-ph/0702170].

[22] A. Nyffeler, Phys. Rev. D **79**, 073012 (2009) [arXiv:0901.1172 [hep-ph]].

[23] M. J. Ramsey-Musolf and M. B. Wise, Phys. Rev. Lett. **89**, 041601 (2002) [arXiv:hep-ph/0201297].

[24] A. Nyffeler, Chin. Phys. C **34**, 705 (2010) [arXiv:1001.3970 [hep-ph]].

[25] T. Kinoshita, B. Nizic and Y. Okamoto, Phys. Rev. D **31**, 2108 (1985).

[26] J. F. Donoghue, E. Golowich and B. R. Holstein, *Dynamics of the Standard Model*, Cambridge Univ. Press, Cambridge (1992).

[27] J. Gasser and H. Leutwyler, Annals Phys. **158**, 142 (1984); Nucl. Phys. B **250**, 465 (1985).

[28] M. Bando, T. Kugo, S. Uehara, K. Yamawaki and T. Yanagida, Phys. Rev. Lett. **54**, 1215 (1985).

[29] J. Bijnens and P. Talavera, JHEP **0203**, 046 (2002) [arXiv:hep-ph/0203049].

[30] R. Unterdorfer and H. Pichl, Eur. Phys. J. C **55**, 273 (2008) [arXiv:0801.2482 [hep-ph]].

[31] M. Gonzalez-Alonso, A. Pich and J. Prades, Phys. Rev. D **78**, 116012 (2008) [arXiv:0810.0760 [hep-ph]].

[32] J. Ahrens *et al.*, Eur. Phys. J. A **23**, 113 (2005) [arXiv:nucl-ex/0407011].

[33] M. E. Peskin and D. V. Schroeder, *An Introduction to Quantum Field Theory*, Westview Press (1995).

[34] G. Ecker, J. Gasser, A. Pich and E. de Rafael, Nucl. Phys. B **321**, 311 (1989).

[35] M. Bando, T. Fujiwara and K. Yamawaki, Prog. Theor. Phys. **79**, 1140 (1988).

[36] G. Ecker, J. Gasser, H. Leutwyler, A. Pich and E. de Rafael, Phys. Lett. B **223**, 425 (1989).

[37] J. F. Donoghue and A. F. Perez, Phys. Rev. D **55**, 7075 (1997) [hep-ph/9611331].

[38] S. Weinberg, Phys. Rev. Lett. **18**, 507 (1967).

[39] G. P. Lepage and S. J. Brodsky, Phys. Lett. B **87**, 359 (1979).

[40] M. Z. Abyaneh, arXiv:1208.2554 [hep-ph].

[41] P. Cvitanovic and T. Kinoshita, Phys. Rev. D **10**, 3978 (1974).

[42] P. Cvitanovic and T. Kinoshita, Phys. Rev. D **10**, 3991 (1974).

[43] T. Hahn, Comput. Phys. Commun. **168**, 78 (2005) [arXiv:hep-ph/0404043].

[44] K. T. Engel, H. H. Patel and M. J. Ramsey-Musolf, Phys. Rev. D **86**, 037502 (2012) [arXiv:1201.0809 [hep-ph]].

[45] J. Bijnens and M. Z. Abyaneh, EPJ Web Conf. **37**, 01007 (2012) [arXiv:1208.3548 [hep-ph]].